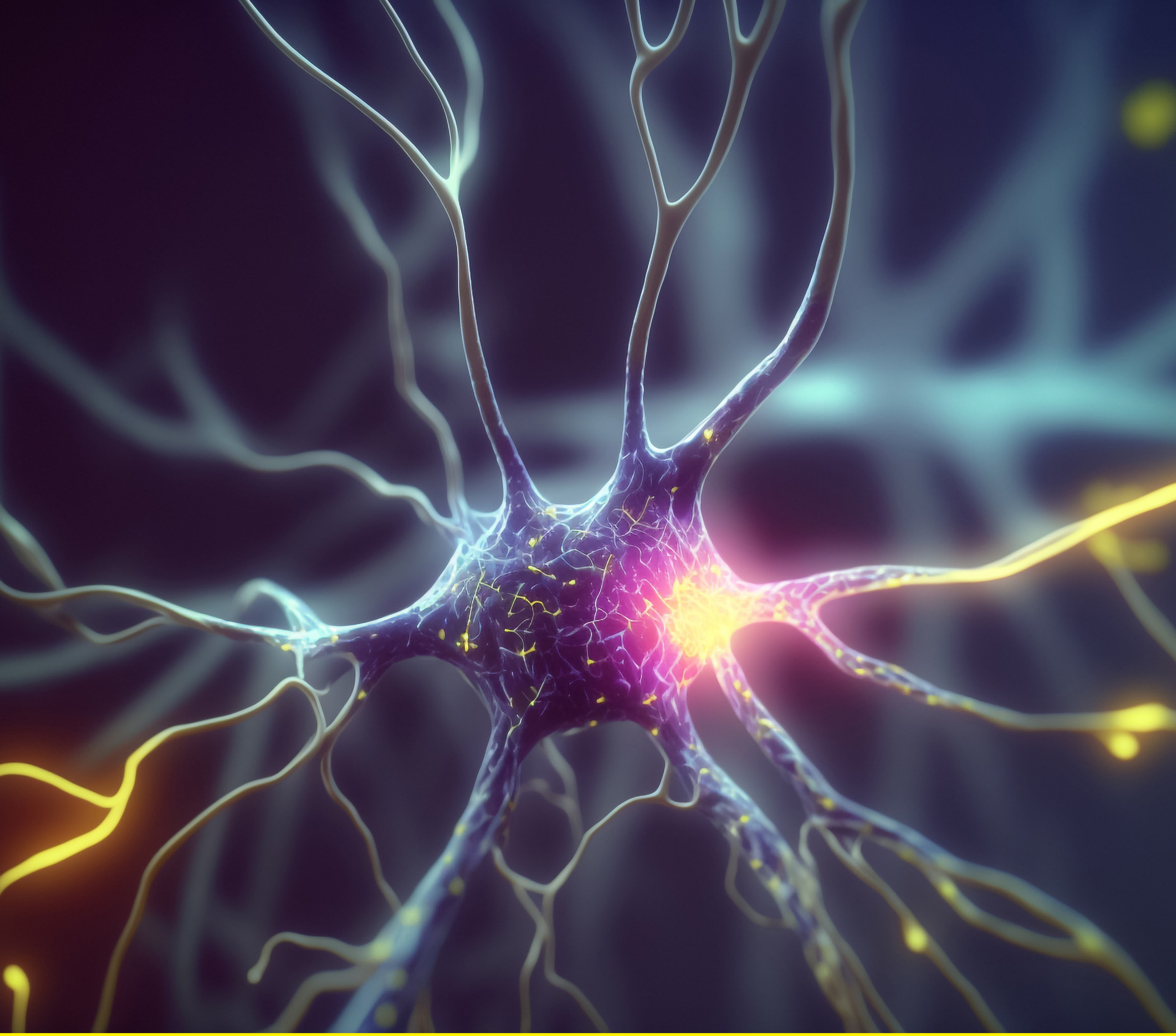

Live-Cell Imaging and Analysis for Neuroscience

ARTICLE COLLECTION

Sponsored by:

WILEY

SARTORIUS


SARTORIUS
INCUCYTE

Contents

COVER IMAGE © SARTORIUS

Introduction

The brain is a complex organ, comprising numerous cell types that interact with each other in a myriad of ways. The most fundamental unit of interaction is at the level of the synapse, which has expanded beyond just the pre- and post-synaptic compartments of two connecting neurons to include modulation by associated astrocytes and surveillance, as well as potential pruning by microglia. The ability to study these interactions in a reductionist manner is key to understanding their role in both physiology and pathology. The use of live-cell imaging to examine neurite outgrowth and morphology enables elucidation of the cellular mechanisms underlying these processes. Additionally, characterizing morphological and functional aspects of glia cell types, such as cell motility, can lead to insights into their contributing biological roles.

In this article collection, we highlight recent case studies exemplifying the power of live-cell imaging for neuroscience and the development of therapeutics. First, Wang et al (2021) examines the use of Astragaloside IV (AS-IV), an herbal extract, as a pro-integrin compound to promote neurite outgrowth. They found that AS-IV increased the expression and activity of integrin-β, which through increasing intracellular structural force, promoted greater neurite extension. Next, Wadhani et al (2019) utilized CRISPR-Cas9 edited induced pluripotent stem cells differentiated into neurons to examine the expression of apolipoprotein E isoform E4, a genetic risk factor for Alzheimer's disease. Imaging of cultured neurons and analysis of morphological parameters, such as neurite length and branching, found expression of E4 increased susceptibility to cytotoxicity, which was associated with increased tau phosphorylation and spreading, consistent with the pathological hallmarks observed in Alzheimer's disease.

Concluding the first half of this article collection is a Sartorius application note regarding the use of the Incucyte® Live-Cell Analysis System to kinetically quantify neurite outgrowth in mono- and co-culture systems, and how combining novel, non-perturbing reagents that deploy longer wavelength fluorophores designed for neuronal-specific measurements along with lab-tested protocols ensures reproducible and unprecedented access to phenotypic information.

The second half of this collection focuses on non-neuronal cells including microglia and astrocytes. Levi et al. (2022) used *in vitro* glia models of ataxia-telangiectasia, a disease caused by mutations in the *ATM* gene, to investigate the role of microglia in mechanisms underlying disease-associated cerebellar degeneration. They found that *ATM* deficiency led to altered microglia morphology, increased cell migration, as well as a significant reduction of cellular activity, such as phagocytosis, neurotrophic factor release, and mitochondrial activity. Lastly, we present a white paper by Alcantara et al. (2021) describing a number of live-cell techniques that allow for real-time monitoring of astroglia models through the quantification of growth, morphology, and functionality. This paper describes how a combination of live-cell analysis techniques provides the flexibility required to enable the characterization of highly dynamic astrocytic models by quantifying their growth, morphology, motility and functional analysis.

We hope the readers of this collection will gain a deeper understanding of how live-cell imaging can elucidate cellular mechanisms in neuronal and non-neuronal cell types, leading to the advancement of translatable models facilitating the development of potential therapeutic interventions.

References

Wang, Y., Zhou, J., Tang, C., et al. (2021) Positive effect of Astragaloside IV on neurite outgrowth via talin-dependent integrin signaling and microfilament force. *J Cell Physiol*. 236: 2156– 2168coo. https://doi.org/10.1002/jcp.30002

Wadhwani, A.R., Affaneh, A., Van Gulden, S. and Kessler, J.A. (2019), Neuronal apolipoprotein E4 increases cell death and phosphorylated tau release in Alzheimer's disease. *Ann Neurol*, 85: 726-739. https://doi.org/10.1002/ana.25455

Trigg, J., et al. (2023) Quantification of neurite dynamics in mono-cultures and co-cultures using the Incucyte® Live-Cell Analysis System. *Sartorius*

Levi, H., Bar, E., Cohen-Adiv, S., Sweitat, S., Kanner, S., Galron, R., Mitiagin, Y., & Barzilai, A. (2022). Dysfunction of cerebellar microglia in Ataxia-telangiectasia. *Glia*, 70(3), 536– 557. https://doi.org/10.1002/glia.24122

Alcantara, S. L., et al. (2021) Characterizing astroglia models with live-cell analysis. *Sartorius*

Received: 8 January 2020 | Accepted: 28 July 2020

DOI: 10.1002/jcp.30002

ORIGINAL RESEARCH ARTICLE

Journal of Cellular Physiology WILEY

Positive effect of Astragaloside IV on neurite outgrowth via talin-dependent integrin signaling and microfilament force

Yifan Wang[1] | **Jingwen Zhou**[1] | **Chuanfeng Tang**[2] | **Jia Yu**[1] | **Wen Zhu**[1] | **Jun Guo**[3] | **Yue Wang**[1]

[1]Affiliated Hospital of Nanjing University of Chinese Medicine, Jiangsu Province Hospital of Chinese Medicine, Nanjing, China

[2]State Key Laboratory of Pharmaceutical Biotechnology, School of Life Sciences, Nanjing University, Nanjing, China

[3]School of Medicine and Holistic Integrative Medicine, Nanjing University of Chinese Medicine, Nanjing, China

Correspondence

Yue Wang, Affiliated Hospital of Nanjing University of Chinese Medicine, Jiangsu Province Hospital of Chinese Medicine, Nanjing 210029, China.
Email: wangyuephd@163.com

Jun Guo, School of Medicine and Holistic Integrative Medicine, Nanjing University of Chinese Medicine, Nanjing 210023, China.
Email: guoj@njucm.edu.cn

Funding information

A Project Funded by the Priority Academic Program Development of Jiangsu Higher Education Institutions; National Natural Science Foundation of China, Grant/Award Numbers: 81774274, 81973769; Open Projects of the Discipline of Chinese Medicine of Nanjing University of Chinese Medicine Supported by the Subject of Academic priority discipline of Jiangsu Higher Education Institutions, Grant/Award Number: NO.ZYX03KF...; Chinese Medicine Science and Technology Program of Jiangsu Province, Grant/Award Number: YB2017090

Abstract

Integrin plays a prominent role in neurite outgrowth by transmitting both mechanical and chemical signals. Integrin expression is closely associated with Astragaloside IV (AS-IV), the main component extracted from *Astragali radix*, which has a positive effect on neural-protection. However, the relationship between AS-IV and neurite outgrowth has not been studied exhaustively to date. The present study investigated the underlying mechanism of AS-IV on neurite outgrowth. Longer neurites have been observed in SH-SY5Y cells or cortical neurons after AS-IV treatment. Furthermore, AS-IV not only increased the expression of integrin β but also activated it. The AS-IV-induced increased integrin activity was attributed to the integrin-activating protein talin. Application of the actin force probe showed that AS-IV led to an increase in intracellular microfilament force during neurite growth. Furthermore, in response to AS-IV, the microfilament force was regulated by talin and integrin activity during neurite growth. These results suggest that AS-IV has the ability to increase intracellular structural force and facilitate neurite elongation by integrin signaling, which highlights its therapeutic potential for neurite outgrowth.

KEYWORDS

Astragaloside IV, integrin, neurite, talin

1 | INTRODUCTION

Impairment of central nervous system (CNS) function is a dominant feature of neurodegenerative disorders and has consequently received considerable attention. Reconstruction of neural networks plays a central role in the functional recovery of the CNS after injury (J. Li & Lepski, 2013; Schubert, Dorkenwald, Januszewski, Jain, & Kornfeld, 2019). This reconstruction depends on the effective extension of neurites (W. Li et al., 2018), which is closely related to integrin (Cheah & Andrews, 2018; Eva & Fawcett, 2014; Lilja & Ivaska, 2018).

The transmembrane protein integrin is a functionally conserved cell-adhesion receptor for the transmission of mechanical and chemical signals between the extracellular matrix (ECM) and the

---

Yifan Wang and Jingwen Zhou contributed equally to this study.

cytoskeleton (Humphries, Chastney, Askari, & Humphries, 2019; Sun, Guo, & Fassler, 2016). Integrin is composed of noncovalently bound α and β subunits, both of which possess an extracellular ligand-binding region and a universally cytoplasmic tail that combines with a multitude of cytoskeletal and adaptor molecules (Iwamoto & Calderwood, 2015). Integrin adopts low-, intermediate-, and high-affinity states in cells (Sun, Costell, & Fassler, 2019). The transformation from a low-affinity to a high-affinity state has been termed "integrin activation" (Iwamoto & Calderwood, 2015; Sun et al., 2019). Clustering and activation of integrin recruits and activates intracellular signaling molecules, such as focal adhesion kinase (FAK), Src, and integrin-linked kinase (ILK), all of which are involved in neuronal polarization and growth, and are conducive to axonal guidance and regeneration (Borghi, Lowndes, Maruthamuthu, Gardel, & Nelson, 2010; S. Chen et al., 2017; Eva & Fawcett, 2014; Kerstein, Patel, & Gomez, 2017; Lee, Lee, & Kim, 2012; Mills et al., 2003; Palazzo, Eng, Schlaepfer, Marcantonio, & Gundersen, 2004; Pastuhov et al., 2016; Stanslowsky et al., 2016; Suzuki et al., 2014).

Talin is the pivotal integrin-activating protein and is widely present in the cytoplasm (Goult, Yan, & Schwartz, 2018; Haining, Lieberthal, & Del Rio Hernandez, 2016). It consists of an N-terminal head domain (~50 kDa) and a large C-terminal flexible rod domain (~220 kDa). The head domain activates integrin by combining with its β subunit cytoplasmic tails, while the rod domain binds directly to the actin cytoskeleton (Goult et al., 2018; Klapholz & Brown, 2017). The formation of the integrin–talin–actin complex was considered a significant step in the transmission of mechanical and chemical signals and has been shown to be beneficial for the crosstalk between them (Kanchanawong et al., 2010; Kumar et al., 2019; Nakao, Maki, Mofrad, & Adachi, 2019). In previous research, mechanical stimuli could be transformed into a biochemical signal via the integrin–talin–actin complex (Kukkurainen et al., 2014; Neumann & Gottschalk, 2016; Sun et al., 2019). Furthermore, a positive correlation was identified between talin and nerve growth factor (NGF)-induced intracellular microfilament force during neuronal polarization and growth (Dingyu et al., 2016). Talin-dependent integrin signaling could mediate the transmission of intracellular microfilament force (Nordenfelt, Elliott, & Springer, 2016; Sun, Guo, & Fässler, 2016).

Astragaloside IV (AS-IV) is a natural saponin and PPARγ agonist, extracted from *Astragali radix* (X. Wang et al., 2017). It has previously been reported that AS-IV had a protective effect against cerebral ischemic-reperfusion injury and glutamate-induced neurotoxicity (Costa et al., 2019; J. Yang et al., 2012; Yue et al., 2015) and decreased the production of amyloid β-protein (Aβ) in Alzheimer's disease (Chang et al., 2016; X. Wang et al., 2017). Moreover, AS-IV could upregulate the expression of integrin in high glucose-induced podocyte and ameliorate diabetic nephropathy by restoring the expression of integrin in diabetic rats (J. Chen et al., 2008; J. Chen et al., 2014). However, there is a paucity of evidence regarding AS-IV participating in neurite outgrowth, and whether this process is correlated with integrin signaling remains to be explored.

This study investigated the mechanisms when AS-IV mediated talin-dependent integrin signaling and its relationship with neurite elongation. Moreover, the application of the actin force probe, based on the Förster resonance energy transfer (FRET), clarified the effect of AS-IV in regulating the mechanical properties of the cytoskeletal force during neurite elongation. This further enabled the detection of crosstalk between intracellular mechanical activity and chemical signaling during neurite outgrowth. This study highlights the potential of AS-IV for the treatment of neurodegenerative diseases.

2 | MATERIALS AND METHODS

2.1 | Chemicals and reagents

AS-IV was purchased from Sigma-Aldrich (St. Louis, MO). Manganese chloride was purchased from Sinopharm (Beijing, China) and Firategrast was purchased from MedChemExpress (Monmouth Junction, NJ). Recombinant murine β-nerve growth factor (β-NGF) was purchased from Peprotech (Rocky Hill, NJ).

2.2 | Cells and neuronal culture

Human SH-SY5Y cells were cultured in DMEM/F12 (Wisent, Montreal, Canada) at 37°C in a 5% CO_2 atmosphere. The medium was supplemented with 10% heat-inactivated fetal bovine serum (Gibco, Invitrogen, Grand Island, NY) and 1% mixture of penicillin and streptomycin (Gibco, Invitrogen, Grand Island, NY). Female C57BL/6 mice were obtained from the Model Animal Research Center (Nanjing University, Nanjing, China). All animal care and handling procedures closely followed the NIH Guide for the Care and Use of Laboratory Animals and were approved by the Animal Care and Use Committee of the Nanjing University of Chinese Medicine (Nanjing, China). Cortical neurons were obtained from C57BL/6 mice cortices at embryonic day 18.5. Dissociated neurons were treated in 12-well plates, precoated with poly-L-lysine (Beyotime Biotechnology Jiangsu, China) and maintained in Neurobasal medium containing 2% B27 and 0.6% (w/v) D-glucose (Thermo Fisher Scientific, Waltham, MA) under humidified air containing 5% CO_2 at 37°C.

2.3 | Immunofluorescence analysis

Cells were fixed in 4% paraformaldehyde solution for 30 min at room temperature. Then, they were cultured with 0.1% Triton X-100 for 15 min at 4°C. After that, cells were incubated with 5% bovine serum albumin/phosphate-buffered saline (PBS) for 30 min at room temperature. For fluorescence labeling, cells were incubated with primary antibody anti-active β1 integrin (12G10; ab30394, 1:200; Abcam, Cambridge, MA) overnight at 4°C. After washing with PBS three times, cells were incubated with secondary antibody fluorescein-conjugated goat anti-mouse IgG (H + L) (ZF-0312, IF 1:100; Zsgb-Bio, Beijing, China) for 2 hr in the dark. Hoechst 33342 (Thermo Fisher Scientific) was applied to label nuclei. The change in the fluorescence value was tested by laser confocal microscopy (Leica Microsystems, Wetzlar, Germany).

2.4 | Neurite extension assay

SH-SY5Y cells were labeled with antigrowth-associated protein 43 (GAP-43; bs-0154R, 1:200; Beijing Biosynthesis Biotechnology, Beijing, China), which is a nervous-system-specific growth-associated protein. Cortical neurons were labeled with the anti-microtubule-associated protein tau (10274-1-AP, 1:100; Proteintech Group, Rosemont, IL). Then, cells were detected by an inverted fluorescence microscope, as previously described (Y. Wang et al., 2019). Neurite length was measured by ImageJ (National Institutes of Health, Bethesda, MD). At least 20 cells were assessed in each experiment.

2.5 | Time-lapse imaging of neurite outgrowth

Neurons were cultured in a 12-well culture plate, and cellular morphology was recorded and measured every 1 hr for 2 days by an IncuCyte live-cell imaging system (Essen Instruments, Ann Arbor, MI) installed in the incubator. Cells were imaged under phase. Data were analyzed by Incucyte's NeuroTrack software.

2.6 | Western blot analysis

Cells were dissolved in cell RIPA lysis buffer (Beyotime Bio, Jiangsu, China) supplemented with PMSF (Roche, Basel, Switzerland) and a protease inhibitor cocktail (Sigma-Aldrich). The extracted total proteins were separated via SDS-PAGE and were transferred to nitrocellulose membranes (Bio-Rad, Hercules, CA). After blocking in 5% nonfat milk for 1 hr, the membranes were incubated with primary antibodies overnight at 4°C. After washing three times, the membranes were incubated with secondary antibodies for 2 hr at room temperature. Enhanced chemiluminescence (ECL) chromogenic substrate was applied to enhance immunoreactive protein bands. The intensities were quantified by densitometry (Quantity One; Bio-Rad, Hercules, CA). The following primary antibodies were used: anti-FAK (BA0839-2, WB 1:500; Boster Bio, Pleasanton, CA), anti-integrin β1 (34971, 1:1,000; Cell Signaling Technology, Danvers, MA), anti-β-actin (4970S, 1:1,000; Cell Signaling Technology), anti-pFAK (Y397) (3283, 1:1,000; Cell Signaling Technology), anti-talin (bs-3619R, 1:500; Biosynthesis Biotechnology, Beijing, China), and anti-talin2 (ARG41981, 1:500; Arigobio, Hsinchu City, Taiwan, ROC).

2.7 | Small interfering RNA (siRNA) transfection

Integrin β1, talin, and negative control siRNAs were constructed by Sangon Biotech Co., Ltd (Shanghai, China). The sequence of the negative control (NC) siRNA was 5′-UUCUCCGAACGUGUCACGU-3′. The sequence of integrin β1-siRNA was 5′-CAGUGAAUGG CAACAAUGA-3′. The sequence of talin-siRNA was 5′GCACUCA CUGGAACCAUUATT-3′. Transfection was performed using Lipofectamine 3000 (Invitrogen, Carlsbad, CA), according to the manufacturers' instructions. The siRNAs transfection efficiency was detected by western blot analysis.

2.8 | Förster resonance energy transfer (FRET) analysis

The Actin-cpstFRET-Actin (AcpA) probe was purchased from Addgene (80643). SH-SY5Y cells, transfected with the AcpA probe, were incubated in 1,000 μg/ml Geneticin to remove untransfected cells, and selected cells were diluted into single cells, and cultured in 96-well plates. The effectiveness of FRET in cells was determined as previously described (J. Zhang et al., 2019; X. Zhang et al., 2019). The CFP:FRET ratios were calculated by Equation 1: E = CFP donor/YFP acceptor, which is negatively associated with FRET efficiency, but positively correlated with mechanical force.

2.9 | Cell viability assay

The viability of SH-SY5Y was evaluated by MTT dye 3-(4,5-dimethyl-2-thiazolyl)-2,5-diphenyl-2-H-tetrazolium bromide (Sigma-Aldrich). The cells were seeded in a 96-well plate and treated according to the requirements of the different groups. The cells were treated with 50 μl of MTT (5 mg/ml) for 4 hr in a 37°C incubator. Subsequently, dimethyl sulfoxide (DMSO, 200 ml/well) was added to stop reaction. The absorbance at 570 nm was detected using a microplate reader.

2.10 | Flow cytometric analysis of integrin β1

Flow cytometric analysis of integrin β1 was conducted according to previously described methods (Jin et al., 2015). In brief, expression of activated or total integrin β1 was measured by geometric mean fluorescence intensity and analyzed by FlowJo software (Tree Star, Ashland, OR). The following antibodies were used: anti-active integrin β1 (9EG7; 550531; BD Biosciences, San Jose, CA) and anti-total integrin β1 (MAR4; 555443; BD Biosciences).

2.11 | Statistical analysis

Data analysis was performed using the statistical program SPSS v.16.0 (IBM, Armonk, NY). Results are shown as the means ± standard error of mean (*SEM*). Statistical analyses used two-tailed Student's *t* test and one-way analysis of variance (ANOVA) was used for single-factor sample comparisons. A least significant difference test was used for comparisons between any two means. Each experiment was repeated at least three times.

3 | RESULTS

3.1 | AS-IV is beneficial to neurite elongation in SH-SY5Y cells and cortical neurons

This study explored the association between AS-IV and neurite elongation. First, SH-SY5Y cells were treated with different AS-IV concentrations and NGF for 2 days. Neurites were stained with an anti-GAP-43 antibody to measure their length. As shown in Figure 1, the neurites of SH-SY5Y cells under 80 and 120 μg/ml AS-IV treatment were significantly longer than neurites of the control group. For further investigation, cortical neurons were then stimulated with different concentrations of AS-IV and NGF for 2 days. The neurites in cortical neurons were strained with anti-tau antibody. Immunofluorescence analysis of cortical neurons was consistent with that in SH-SY5Y cells (Figure 1c,d). Similar results were also obtained by time-lapse imaging of neurites, where neurons under the stimulation of AS-IV grew quicker than those of the control group (Movies S1 and S2). In summary, these results suggested that AS-IV promotes neurite outgrowth in both SH-SY5Y cells and cortical neurons.

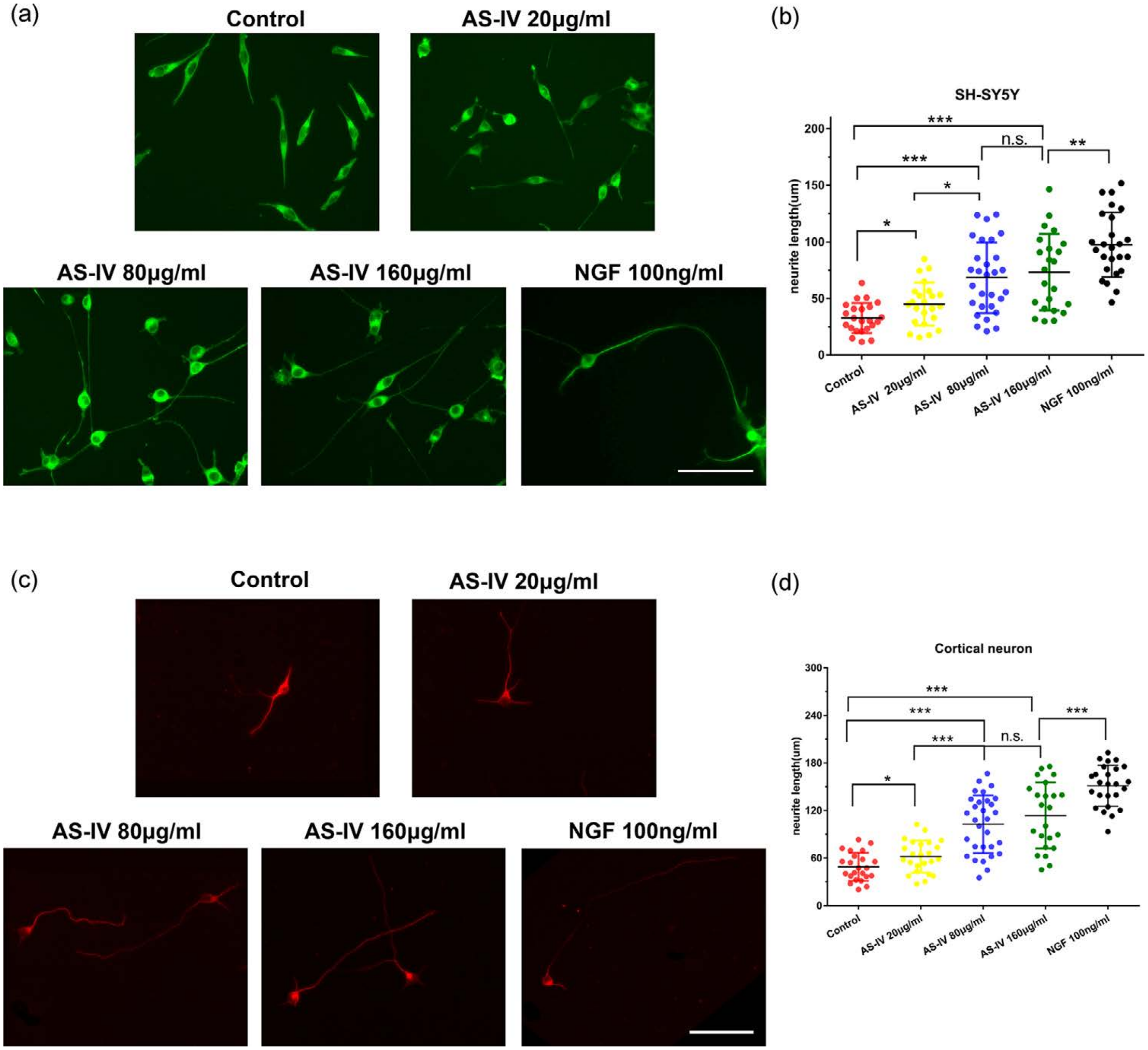

FIGURE 1 AS-IV promotes neurite elongation in SH-SY5Y cells and cortical neurons. (a) SH-SY5Y cells were treated with different AS-IV concentrations and NGF for 2 days. Representative images are shown. Scale bar, 50 μm. (b) Neurite length quantified from (a) (control, $n = 23$ cells; AS-IV 20 μg/ml, $n = 23$ cells; AS-IV 80 μg/ml, $n = 29$ cells; AS-IV 160 μg/ml, $n = 23$ cells; NGF, $n = 25$ cells). (c) Cortical neurons were cultured with different AS-IV concentrations and NGF for 2 days. Representative images are shown. Scale bar, 50 μm. (d) The lengths of neurites were quantified (control, $n = 23$ cells; AS-IV 20 μg/ml, $n = 24$ cells; AS-IV 80 μg/ml, $n = 30$ cells; AS-IV 160 μg/ml, $n = 23$ cells; NGF, $n = 25$ cells). Data were obtained from three independent experiments. Data are presented as means ± *SEM*. One-way ANOVA was used for single-factor sample comparisons. $^*p < .05$ and $^{***}p < .001$ compared with the control. ANOVA, analysis of variance; AS-IV, Astragaloside IV; NGF, nerve growth factor; *SEM*, standard error of mean

3.2 | AS-IV-induced neurite elongation is depended on the expression and activity of integrin β1

To determine whether AS-IV participated in neurite elongation in an integrin-dependent manner, the integrin/FAK signaling pathway was investigated in SH-SY5Y under AS-IV stimulation. Western blot analysis showed that the protein levels of pY397 FAK and integrin β1 in AS-IV-treated SH-SY5Y cells were higher than those of the control group (Figure 2a). Then, the activity of integrin β1 was further examined by immunofluorescence staining using a conformation-specific

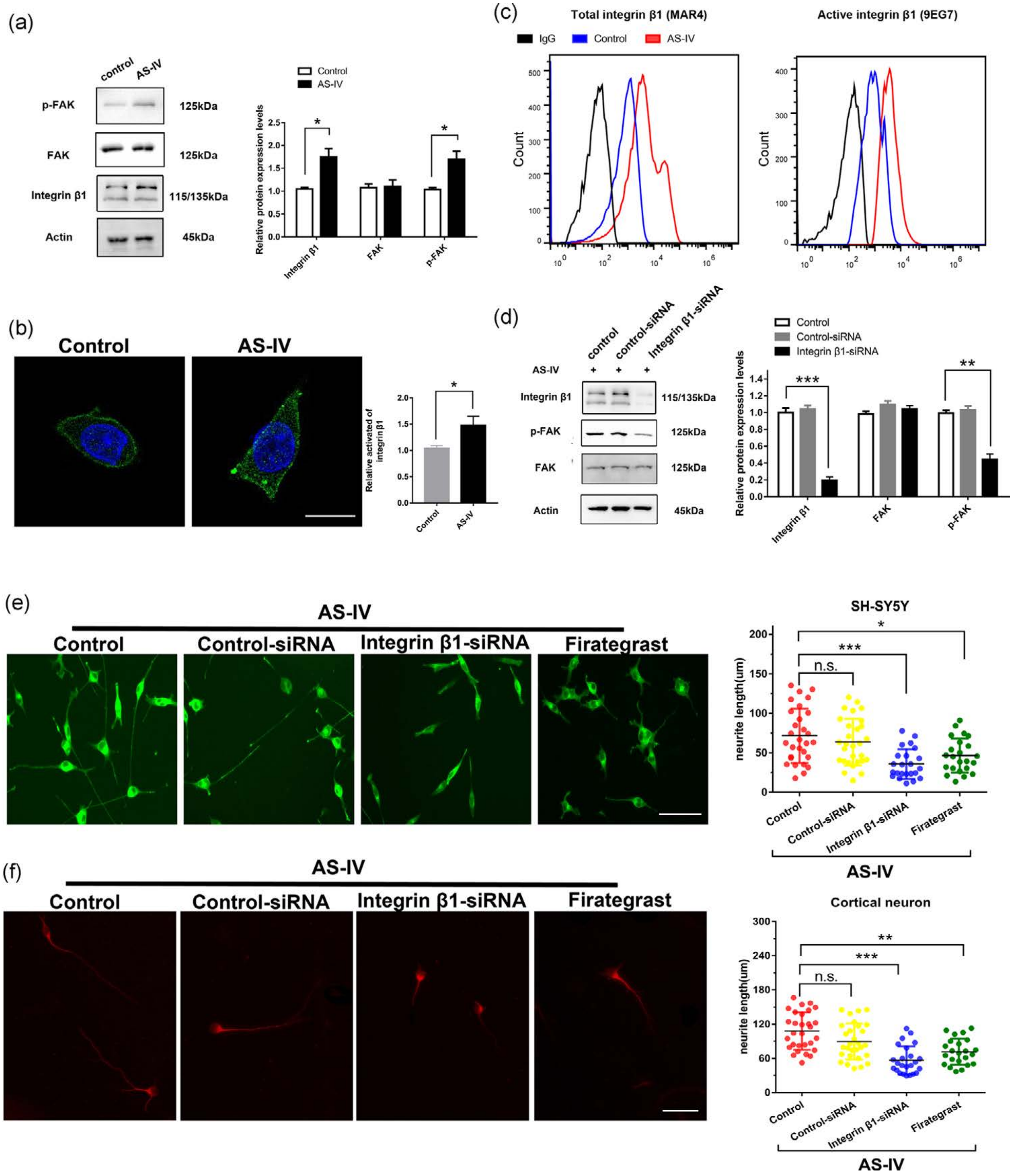

antibody (mAb 12G10). The results indicated that the fluorescence intensity of activated integrin β1 increased in response to AS-IV treatment (Figure 2b). Similar results were obtained in the flow cytometric analysis, where fluorescence intensities of total integrin β1 and activated integrin β1 in the AS-IV group were stronger than that of the control group (Figure 2c). Next, it was examined whether the effect of the expression and activity of integrin β1 was responsible for the AS-IV-induced extension of neurites. SH-SY5Y cells or cortical neurons were transfected with integrin β1-siRNA or treated with firategrast, the antagonist of integrin β1, before AS-IV stimulation. The efficiency of integrin β1-siRNA was detected by western blot analysis (Figure 2d). The results of immunofluorescence analysis suggested that the neurite length was significantly shortened, when the expression or activity of integrin β1 was downregulated in SH-SY5Y cells and cortical neurons (Figure 2e,f). Overall, these results showed that the neurite elongation induced by AS-IV treatment is modulated by the expression and activity of integrin β1.

3.3 | AS-IV promotes neurite elongation by upregulating the expression of talin

To explore whether talin is involved in integrin activation and neurite outgrowth induced by AS-IV, the expression of talin was detected in SH-SY5Y cells by western blot analysis under AS-IV stimulation. The results showed that AS-IV upregulated the protein level of talin (Figure 3a). To further determine the effect of talin on integrin activation induced by AS-IV, siRNA was applied to decrease the expression of talin before AS-IV treatment in SH-SY5Y cells (Figure 3b). The results of immunofluorescence and flow cytometric analyses showed that talin-siRNA decreased the activity of integrin β1, without affecting the expression of total integrin β1 in AS-IV-treated SH-SY5Y cells (Figure 3c,d). Moreover, immunofluorescence analysis showed that the length of neurites decreased significantly by the downregulation of talin expression in SH-SY5Y cells or cortical neurons (Figure 3e,f). In summary, these results suggested that integrin activation and neurite elongation in response to AS-IV is dependent on the expression of talin.

3.4 | AS-IV increases intracellular microfilament force during neurite growth

The above experiments showed that AS-IV upregulated the expression of talin during neurite growth. Furthermore, talin is also involved in neurite growth and regeneration by intercellular mechanical activities (Dingyu et al., 2016). Here, the AcpA probe was applied to explore the relationship between AS-IV and intracellular microfilament force. The CFP/FRET ratio was used to calculate the force in actin, based on previous reports (J. Guo, Wang, Sachs, & Meng, 2014; X. Zhang et al., 2019). SH-SY5Y cells were transfected with the AcpA probe and then treated with AS-IV for 24 hr. As shown in Figure 4, AS-IV-treated SH-SY5Y cells showed stronger actin force compared with the control group. Next, probe-transfected SH-SY5Y were treated with AS-IV for 2 days and actin forces were observed in different areas of the cell. The results showed that the actin force in neurites was higher than that in the cell body under the stimulation of AS-IV (Figure 4c,d), suggesting the involvement of actin force induced by AS-IV in neurite growth. To further identify the association between AS-IV-induced actin force and talin during neurite growth, probe-transfected SH-SY5Y were transfected with talin-siRNA or control-siRNA, and then cultured either with or without AS-IV for 2 days. The results of FRET ratio analysis showed that the actin force induced by AS-IV was attenuated after the inhibition of talin expression (Figure 4e,f). In summary, these results suggest that AS-IV increases intracellular microfilament force during neurite growth.

3.5 | AS-IV is involved in the upregulation of actin force by integrin activation during neurite growth

To better understand the mechanical properties and integrin activity induced by AS-IV during neurite outgrowth, time-lapse imaging was performed for 15 min after treating transfected SH-SY5Y cells with NGF alone, the integrin agonist manganese alone, or both manganese and the integrin antagonist firategrast. FRET analysis showed that the actin force increased under the stimulation of NGF or manganese treatment, while the increasing trend induced by manganese was reversed by firategrast (Figure 5a,b). This suggested that the actin force

FIGURE 2 Neurite elongation in response to AS-IV is dependent on the expression and activation of integrin β1. (a) SH-SY5Y cells were cultured with 80 μg/ml of AS-IV for 2 days. The protein levels of integrin β1, FAK, and pY397 FAK were measured by western blot analysis, with β-actin as loading control. (b) Integrin β1 activity was assessed through staining with conformation-specific antibody (mAb 12G10). Nuclei were counterstained by Hoechst 33342. Scale bar, 10 μm. (c) Flow cytometric analysis of total and activated integrin β1 in cells. (d) SH-SY5Y cells were transfected with siRNA against integrin β1. Two days after transfection, the protein levels of integrin β1, FAK, and pY397 FAK were measured by western blot analysis, with β-actin as loading control. (e) SH-SY5Y cells transfected with control-siRNA or integrin β1-siRNA were treated with AS-IV for 2 days. Immunofluorescence images show the neurite length in SH-SY5Y cells. The length of the longest neurite in cells was measured (control, $n = 29$ cells; control-siRNA, $n = 29$ cells; integrin β1-siRNA, $n = 23$ cells; firategrast, $n = 23$ cells). Scale bar, 50 μm. (f) Immunofluorescence images show neurite lengths in cortical neurons. The length of the longest neurites in cells was measured (control, $n = 29$ cells; control-siRNA, $n = 29$ cells; integrin β1-siRNA, $n = 24$ cells; firategrast, $n = 23$ cells). Scale bar, 50 μm. Symbols indicate the results of Student's t test; Data were obtained from three independent experiments. Data are presented as means ± *SEM*. $^{*}p < .05$, $^{**}p < .01$, and $^{***}p < .001$; one-way ANOVA was used for single-factor sample comparisons. ANOVA, analysis of variance; AS-IV, Astragaloside IV; FAK, focal adhesion kinase; *SEM*, standard error of mean; siRNA, small interfering RNA was regulated by integrin activity during neurite growth. After treating the transfected cells with AS-IV alone or with the combination of AS-IV and firategrast, the cells were observed for 15 min using fluorescence microscopy. The results showed that the actin force increased in a time-dependent manner under the stimulation of AS-IV, whereas it attenuated in the group with firategrast treatment (Figure 5a,c). In summary, these results suggest that integrin activation induced by AS-IV modulates the microfilament force during neurite growth.

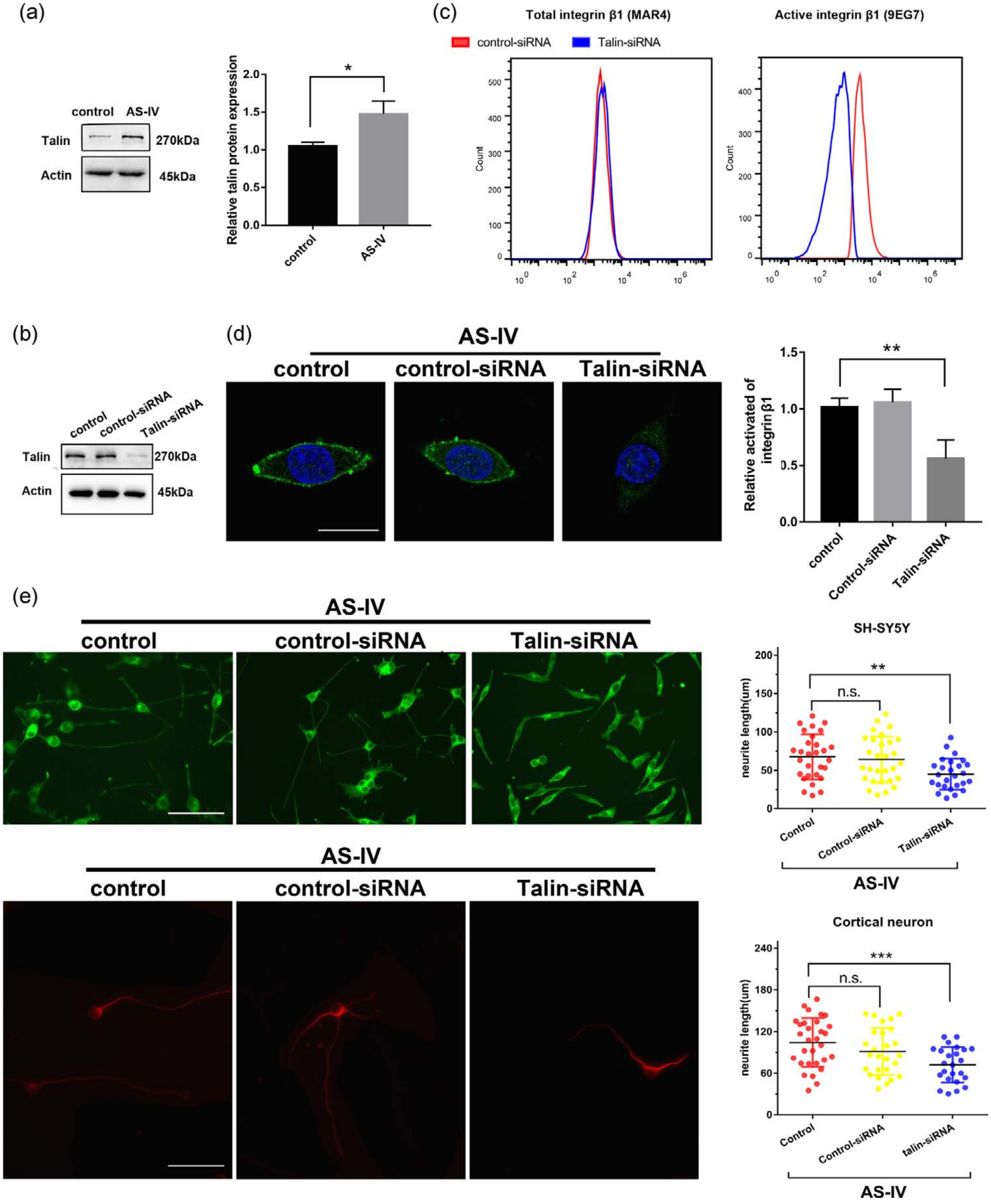

4 | DISCUSSION

Neurite outgrowth is paramount for the establishment of neural networks in developing neurons, which is intimately associated with chemical signaling and mechanical activities (Kim et al., 2018; Toriyama, Kozawa, Sakumura, & Inagaki, 2013). The present study showed that AS-IV had beneficial effects on talin-dependent integrin signaling and intracellular microfilament force during neurite outgrowth.

AS-IV, a triterpenoid saponin, has a moderate penetration in the blood–brain barrier and presents valid protective effects in neurological disorders. Functional or sensory loss occurs because of a multitude of advantageous features, such as antioxidant, antiviral, anti-inflammatory, and immunoregulation functions (Costa et al., 2019; Qu et al., 2009; C. Yang et al., 2019; C. H. Zhang et al., 2019; W. D. Zhang et al., 2006). However, the majority of previous studies on AS-IV have focused on neuroprotection during neurological diseases, while ignoring its possible effect on neurite outgrowth. Recent studies have shown that AS-IV plays a synergistic role in neurite outgrowth (Liang, Zou, Niu, & Niu, 2019). The present study further indicates that AS-IV promoted neurite elongation alone during nerve growth (Figure 1). These lines of evidence suggest that AS-IV not only prevents neurites from various harmful stimuli, but also promotes neurite outgrowth.

Transmembrane cell-adhesion integrins are involved in the appropriate functioning of the nervous system. They cluster in the front of neuronal synapses to promote neurite outgrowth and regeneration by strengthening the connection between the cell and ECM (Nieuwenhuis, Haenzi, Andrews, Verhaagen, & Fawcett, 2018). Previous reports demonstrated that AS-IV modulated the expression of integrin in high glucose-induced podocyte and experimental diabetic nephropathy rats (J. Chen et al., 2008; J. Chen et al., 2014). The data obtained in the present study showed similar results, that is, AS-IV increased the expression of integrin β1 in neurite outgrowth (Figure 2a,c). This suggests that AS-IV may be involved in neurite growth by regulating integrins. However, upregulation of integrin expression only is not sufficient to facilitate neurite extension. The conformational activation of integrin is also crucial for neurite elongation (Cheah & Andrews, 2018). The conformational change of the integrin receptor transformed by focal adhesion proteins and modulated by trafficking and activation molecules facilitates both the maturation of adhesion and ameliorates cell-to-extracellular matrix interaction during neurite growth (Eva & Fawcett, 2014). Interestingly, further analysis demonstrated that the AS-IV increased the activity of integrin β1 during neurite outgrowth (Figure 2b,c). In summary, the experimental evidence allowed to hypothesize that AS-IV promotes neurite outgrowth by the increment of integrin β1 expression and its activity.

Talin is one of the most important mediators of integrin activation, which correlates with neurite growth and regeneration (Tan et al., 2015). It is necessary to investigate the relationship between integrin activation induced by either AS-IV or talin during neurite outgrowth. This study showed that AS-IV upregulated the activities of integrin by increasing the expression of talin (Figure 3a), suggesting that integrin activation in response to AS-IV might have relied on talin during neurite outgrowth. Except for the chemical signal, neurite growth is also accompanied by an array of mechanical activities, such as osmotic pressure and intercellular structure tension, which play a regulative role during neurite extension (Y. C. Guo, Wang, Ge, Yu, & Guo, 2018; Suter & Miller, 2011). Talin was also identified as an intracellular mechanosensor and was found to participate in intracellular mechanical signal transmission (Yao et al., 2016). When mechanical stimuli are applied to talin, it facilitates the exposure of multiple vinculin-binding domains in the talin rod domain. This is beneficial for the formation of the mechanosensitive talin–vinculin complex, reinforces the linkage to actin filaments, and promotes mechanical transmission (del Rio et al., 2009; Gingras et al., 2005; Hytonen & Vogel, 2008). A previous study in NGF-stimulated PC12 cells demonstrated that talin could upregulate neurite growth and regeneration by microfilament force (Dingyu et al., 2016). The application of the FRET-based actin force probe in this study showed that AS-IV manifested a high relevance for talin-dependent intercellular microfilament force (Figure 4). Based on this evidence, it can be speculated that AS-IV may be involved in neurite outgrowth by talin-dependent intracellular cytoskeletal force.

Both intracellular mechanical activities and integrin signaling are part of neural polarization and nerve growth. The formation of the integrin–talin–actin complex is a vitally important procedure in the crosstalk between them (Ciobanasu et al., 2018; Haining et al., 2016; Yao et al., 2016). Mechanical stimulation could effectively regulate

FIGURE 3 AS-IV promotes neurite elongation by increasing talin expression. (a) SH-SY5Y cells were cultured with AS-IV for 2 days. The protein levels of talin and β-actin were detected by western blot analysis. (b) Cells were transfected with siRNA against talin. Two days after transfection, cells were harvested for immunoblotting, with β-actin as loading control. (c) Flow cytometric analysis of total and activated integrin β1 in cells. (d) Integrin β1 activities of representative groups were tested by staining with the conformation-specific antibody (mAb 12G10). Nuclei were counterstained by Hoechst 33342. Scale bar, 10 μm. (e) SH-SY5Y cells transfected with control-siRNA or integrin β1-siRNA were treated with AS-IV for 2 days. Immunofluorescence images show the neurite length in SH-SY5Y cells. The length of the longest neurites in cells was measured with a scale bar of 50 μm (control, $n = 29$ cells; control-siRNA, $n = 29$ cells; talin-siRNA, $n = 26$ cells). (f) Immunofluorescence images show the neurite length in cortical neurons. The length of the longest neurites in cells was measured (control, $n = 30$ cells; control-siRNA, $n = 26$ cells; talin-siRNA, $n = 24$ cells). Scale bar, 50 μm. Data are presented as means ± *SEM* of three separate experiments. $^{*}p < .05$, $^{**}p < .01$, and $^{***}p < .001$. One-way ANOVA was used for single-factor sample comparisons. ANOVA, analysis of variance; AS-IV, Astragaloside IV; *SEM*, standard error of mean; siRNA, small interfering RNA

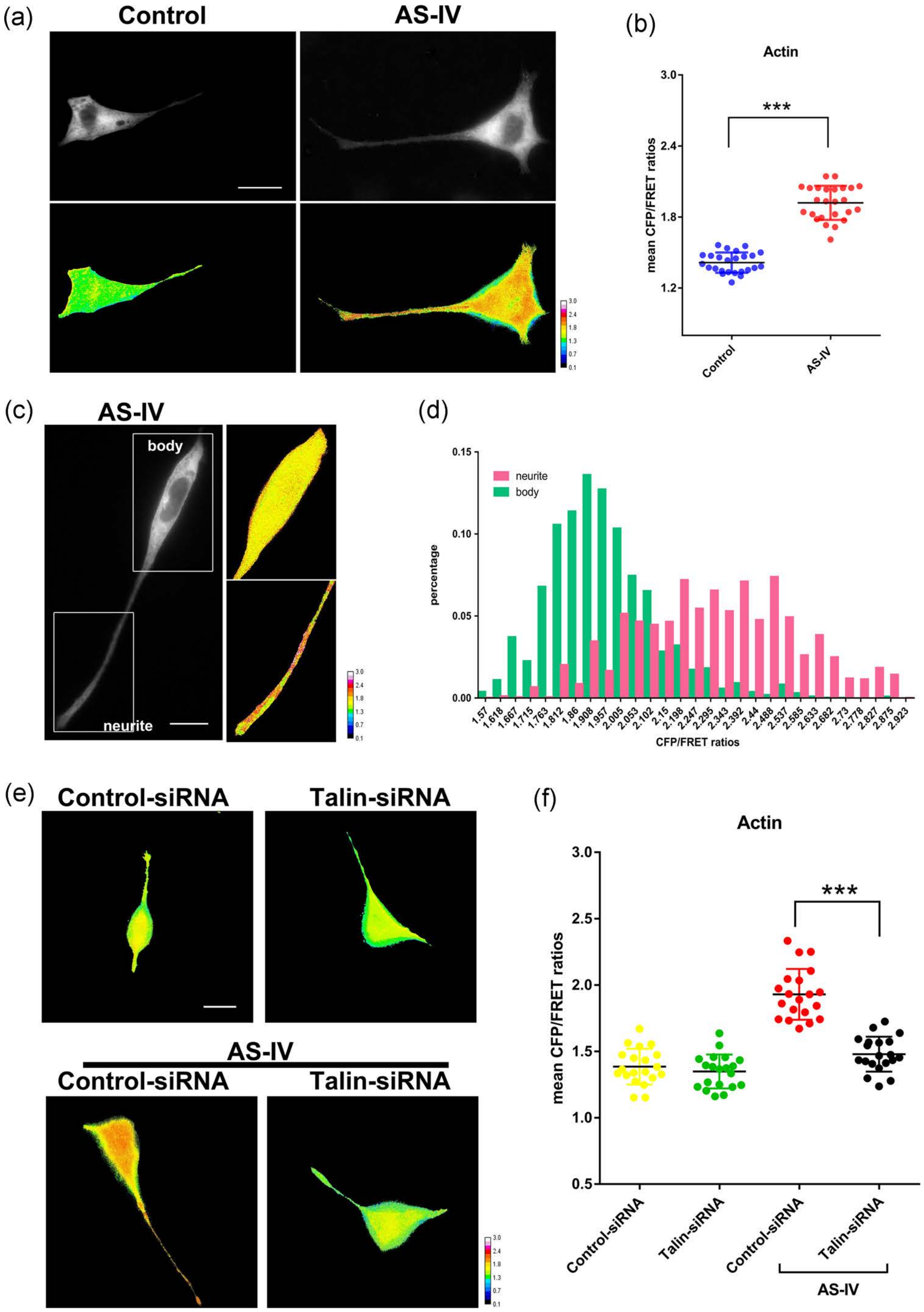

FIGURE 4 AS-IV upregulates intracellular microfilament force during neurite growth. (a,b) Probe-transfected cells were treated with or without AS-IV for 24 hr. A scatter diagram shows the mean CFP/FRET ratios of the above groups ($n = 25$). Scale bar, 10 μm. (c,d) Probe-transfected SH-SY5Y cells were treated with AS-IV for 2 days. The distribution of CFP/FRET ratios is shown. Scale bar, 10 μm. (e,f) Probe-transfected cells were transfected with control-siRNA or talin-siRNA and treated with or without AS-IV for 24 hr. A scatter diagram shows the mean CFP/FRET ratios of the above groups ($n = 20$). Scale bar, 10 μm. The calibration bar was set from 0.1 to 3. All error bars represent the *SEM*. Each experiment was repeated more than three times. ***$p < .001$ compared with the control. AS-IV, Astragaloside IV; CFP, cyan fluorescent protein; FRET, Förster resonance energy transfer; *SEM*, standard error of mean; siRNA, small interfering RNA

integrin conformation and activity via this complex (Kukkurainen et al., 2014; Sun et al., 2019). At the same time, the results of this study suggest that the intracellular microfilament force could be modulated by integrin activation in response to AS-IV (Figure 5). This may be because ectodomains, the single transmembrane, and cytoplasmic domains keep the integrin in its bent conformation when integrin is in low-affinity states. Nevertheless, AS-IV transformed integrin into a stable extended activated high-affinity state, which is beneficial for mechanical transmission (Moser, Legate, Zent, & Fassler, 2009; Yao et al., 2016). Hence, it can conceivably be

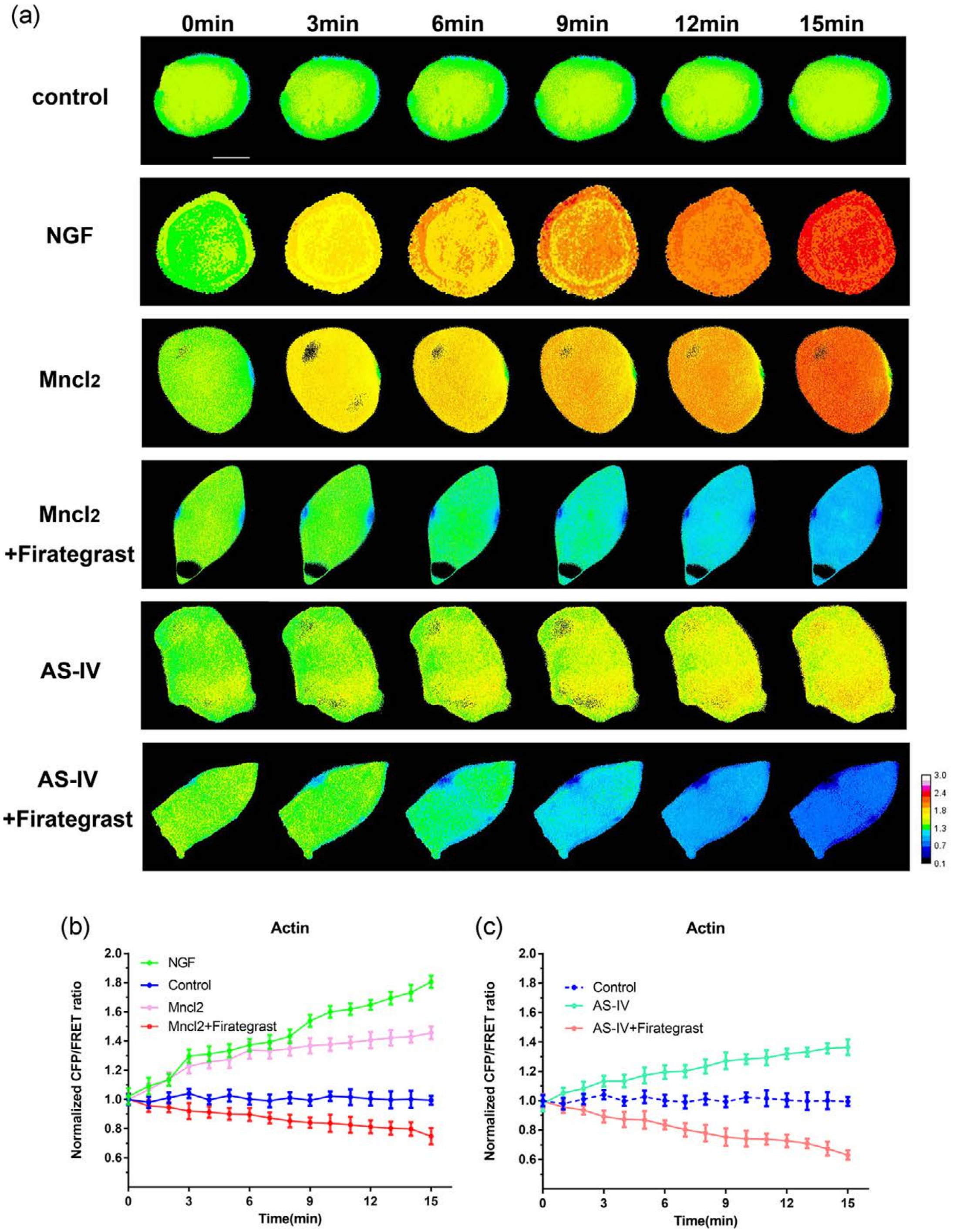

FIGURE 5 Microfilament force in response to AS-IV is modulated by integrin activation during neurite growth. (a) Probe-transfected SH-SY5Y cells were treated with NGF, an activator of integrin manganese, or both manganese and the antagonist of integrin β1 firategrast or AS-IV, or combination of AS-IV and firategrast for 15 min. (b, c) The mean CFP/FRET ratios over the whole cell were obtained by measuring the relative increase compared with the reference value. Normalized CFP and FRET signals corresponded to actin tension versus time. The calibration bar was set from 0.1 to 3. Data show the means ± *SEM* of three separate experiments. Scale bars, 10 μm. AS-IV, Astragaloside IV; CFP, cyan fluorescent protein; FRET, Förster resonance energy transfer; NGF, nerve growth factor; *SEM*, standard error of mean

hypothesized that mechanical activity and integrin signals are inalienable during neurite outgrowth, and transform into each other.

The experimental findings of this study enable a new understanding of AS-IV during neurite outgrowth. AS-IV exerts a positive effect on neurite elongation by integrin conformational changes and leads to an increase in intracellular microfilament force. Furthermore, both of them can transform and interact with each other during neurite outgrowth (Figure 6). The application of mechanical probes allows to evaluate AS-IV in neural therapy from a mechanical perspective, which provides corroborative evidence for the

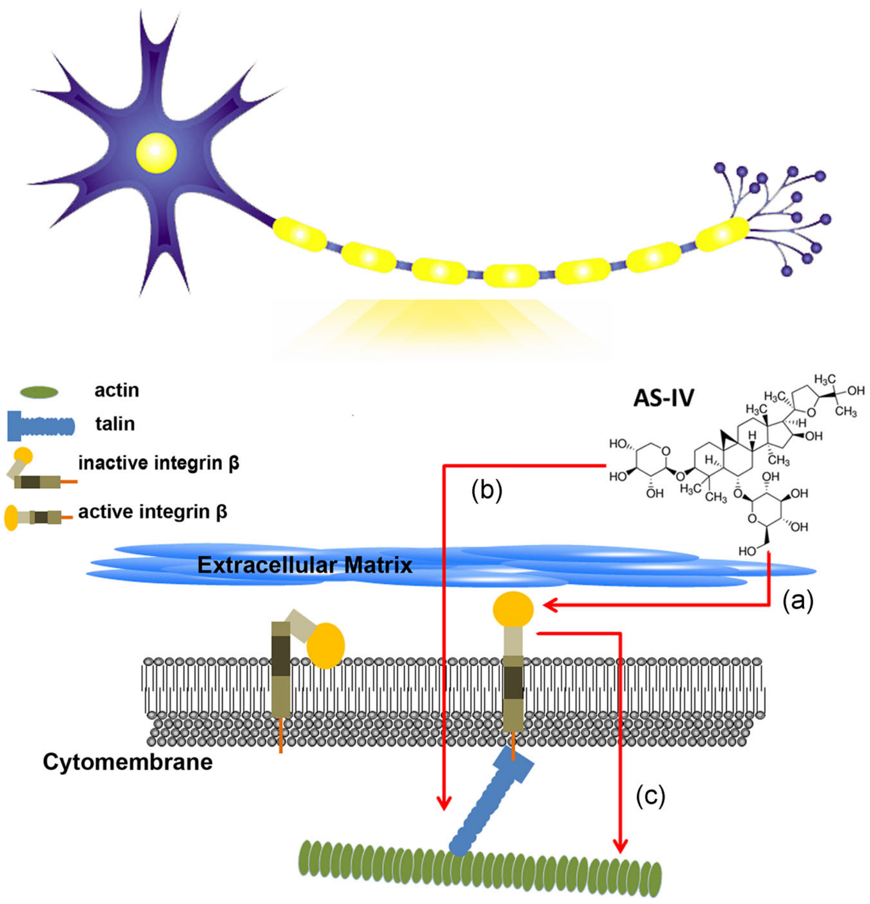

FIGURE 6 The molecular underlying mechanism of AS-IV in neurite outgrowth. (a) AS-IV increased the expression of integrin β1 during neurite growth. (b) AS-IV upregulated the integrin activity and intercellular microfilament force by increasing the expression of talin during neurite outgrowth. (c) Integrin activation improved the microfilament force during neurite outgrowth. AS-IV, Astragaloside IV

effectiveness of AS-IV. In further studies, AS-IV will be used as precursor compound for in vivo experiments to verify its function in the promotion of neurite outgrowth.

ACKNOWLEDGMENTS

This study was supported by grants from the National Natural Science Foundation of China (81774274 and 81973769), a Project Funded by the Priority Academic Program Development of Jiangsu Higher Education Institutions (PAPD, Open Projects of the Discipline of Chinese Medicine of Nanjing University of Chinese Medicine Supported by the Subject of Academic priority discipline of Jiangsu Higher Education Institutions (NO.ZYX03KF...), and the Chinese Medicine Science and Technology Program of Jiangsu Province (YB2017090).

CONFLICT OF INTERESTS

The authors declare that there are no conflict of interests.

AUTHOR CONTRIBUTIONS

Y. W. and Y. W. designed the study. Y. W., J. Z., and C. T. conducted the experiments. W. Z. and J. Y. analyzed the data. Y. W., Y. W., and J. G. wrote the manuscript. All authors read the final version of the manuscript. All authors approve and agree to be responsible for all aspects of this study.

DATA AVAILABILITY STATEMENT

The data sets used and/or analyzed during the current study are available from the corresponding author on reasonable request.

ORCID

Yifan Wang http://orcid.org/0000-0002-2655-4154

REFERENCES

Borghi, N., Lowndes, M., Maruthamuthu, V., Gardel, M. L., & Nelson, W. J. (2010). Regulation of cell motile behavior by crosstalk between cadherin- and integrin-mediated adhesions. *Proceedings of the National Academy of Sciences of the United States of America*, *107*(30), 13324–13329. https://doi.org/10.1073/pnas.1002662107

Chang, C. P., Liu, Y. F., Lin, H. J., Hsu, C. C., Cheng, B. C., Liu, W. P., … Lin, K. C. (2016). Beneficial effect of astragaloside on Alzheimer's disease condition using cultured primary cortical cells under beta-amyloid exposure. *Molecular Neurobiology*, *53*(10), 7329–7340. https://doi.org/10.1007/s12035-015-9623-2

Cheah, M., & Andrews, M. R. (2018). Integrin activation: Implications for axon regeneration. *Cells*, *7*(3), 20. https://doi.org/10.3390/cells7030020

Chen, J., Chen, Y., Luo, Y., Gui, D., Huang, J., & He, D. (2014). Astragaloside IV ameliorates diabetic nephropathy involving protection of podocytes in streptozotocin induced diabetic rats. *European Journal of Pharmacology*, *736*, 86–94. https://doi.org/10.1016/j.ejphar.2014.04.037

Chen, J., Gui, D., Chen, Y., Mou, L., Liu, Y., & Huang, J. (2008). Astragaloside IV improves high glucose-induced podocyte adhesion dysfunction via alpha3beta1 integrin upregulation and integrin-linked kinase inhibition. *Biochemical Pharmacology*, *76*(6), 796–804. https://doi.org/10.1016/j.bcp.2008.06.020

Chen, S., Tisch, N., Kegel, M., Yerbes, R., Hermann, R., Hudalla, H., … Martin-Villalba, A. (2017). CNS macrophages control neurovascular development via CD95L. *Cell Reports*, *19*(7), 1378–1393. https://doi.org/10.1016/j.celrep.2017.04.056

Ciobanasu, C., Wang, H., Henriot, V., Mathieu, C., Fente, A., Csillag, S., … Le Clainche, C. (2018). Integrin-bound talin head inhibits actin filament barbed-end elongation. *Journal of Biological Chemistry*, *293*(7), 2586–2596. https://doi.org/10.1074/jbc.M117.808204

Costa, I. M., Lima, F. O. V., Fernandes, L. C. B., Norrara, B., Neta, F. I., Alves, R. D., … Guzen, F. P. (2019). Astragaloside IV supplementation promotes a neuroprotective effect in experimental models of neurological disorders: A systematic review. *Current Neuropharmacology*, *17*(7), 648–665. https://doi.org/10.2174/1570159X16666180911123341

del Rio, A., Perez-Jimenez, R., Liu, R., Roca-Cusachs, P., Fernandez, J. M., & Sheetz, M. P. (2009). Stretching single talin rod molecules activates vinculin binding. *Science*, *323*(5914), 638–641. https://doi.org/10.1126/science.1162912

Dingyu, W., Fanjie, M., Zhengzheng, D., Baosheng, H., Chao, Y., Yi, P., … Gang, H. (2016). Regulation of intracellular structural tension by talin in the axon growth and regeneration. *Molecular Neurobiology*, *53*(7), 4582–4595. https://doi.org/10.1007/s12035-015-9394-9

Eva, R., & Fawcett, J. (2014). Integrin signalling and traffic during axon growth and regeneration. *Current Opinion in Neurobiology*, *27*, 179–185. https://doi.org/10.1016/j.conb.2014.03.018

Gingras, A. R., Ziegler, W. H., Frank, R., Barsukov, I. L., Roberts, G. C., Critchley, D. R., & Emsley, J. (2005). Mapping and consensus sequence identification for multiple vinculin binding sites within the talin rod. *Journal of Biological Chemistry*, *280*(44), 37217–37224. https://doi.org/10.1074/jbc.M508060200

Goult, B. T., Yan, J., & Schwartz, M. A. (2018). Talin as a mechanosensitive signaling hub. *Journal of Cell Biology*, *217*(11), 3776–3784. https://doi.org/10.1083/jcb.201808061

Guo, J., Wang, Y., Sachs, F., & Meng, F. (2014). Actin stress in cell reprogramming. *Proceedings of the National Academy of Sciences of the United States of America*, *111*(49), E5252–E5261. https://doi.org/10.1073/pnas.1411683111

Guo, Y. C., Wang, Y. X., Ge, Y. P., Yu, L. J., & Guo, J. (2018). Analysis of subcellular structural tension in axonal growth of neurons. *Reviews in the Neurosciences*, *29*(2), 125–137. https://doi.org/10.1515/revneuro-2017-0047

Haining, A. W., Lieberthal, T. J., & Del Rio Hernandez, A. (2016). Talin: A mechanosensitive molecule in health and disease. *FASEB Journal*, *30*(6), 2073–2085. https://doi.org/10.1096/fj.201500080R

Humphries, J. D., Chastney, M. R., Askari, J. A., & Humphries, M. J. (2019). Signal transduction via integrin adhesion complexes. *Current Opinion in Cell Biology*, *56*, 14–21. https://doi.org/10.1016/j.ceb.2018.08.004

Hytonen, V. P., & Vogel, V. (2008). How force might activate talin's vinculin binding sites: SMD reveals a structural mechanism. *PLOS Computational Biology*, *4*(2), e24. https://doi.org/10.1371/journal.pcbi.0040024

Iwamoto, D. V., & Calderwood, D. A. (2015). Regulation of integrin-mediated adhesions. *Current Opinion in Cell Biology*, *36*, 41–47. https://doi.org/10.1016/j.ceb.2015.06.009

Jin, J. K., Tien, P. C., Cheng, C. J., Song, J. H., Huang, C., Lin, S. H., & Gallick, G. E. (2015). Talin1 phosphorylation activates beta1 integrins: A novel mechanism to promote prostate cancer bone metastasis. *Oncogene*, *34*(14), 1811–1821. https://doi.org/10.1038/onc.2014.116

Kanchanawong, P., Shtengel, G., Pasapera, A. M., Ramko, E. B., Davidson, M. W., Hess, H. F., & Waterman, C. M. (2010). Nanoscale architecture of integrin-based cell adhesions. *Nature*, *468*(7323), 580–584. https://doi.org/10.1038/nature09621

Kerstein, P. C., Patel, K. M., & Gomez, T. M. (2017). Calpain-mediated proteolysis of talin and FAK regulates adhesion dynamics necessary for axon guidance. *Journal of Neuroscience*, *37*(6), 1568–1580. https://doi.org/10.1523/JNEUROSCI.2769-16.2016

Kim, G. B., Chen, Y., Kang, W., Guo, J., Payne, R., Li, H., … Yang, J. (2018). The critical chemical and mechanical regulation of folic acid on neural engineering. *Biomaterials*, *178*, 504–516. https://doi.org/10.1016/j.biomaterials.2018.03.059

Klapholz, B., & Brown, N. H. (2017). Talin—The master of integrin adhesions. *Journal of Cell Science*, *130*(15), 2435–2446. https://doi.org/10.1242/jcs.190991

Kukkurainen, S., Maatta, J. A., Saeger, J., Valjakka, J., Vogel, V., & Hytonen, V. P. (2014). The talin–integrin interface under mechanical stress. *Molecular BioSystems*, *10*(12), 3217–3228. https://doi.org/10.1039/c4mb00341a

Kumar, A., Shutova, M. S., Tanaka, K., Iwamoto, D. V., Calderwood, D. A., Svitkina, T. M., & Schwartz, M. A. (2019). Filamin A mediates isotropic distribution of applied force across the actin network. *Journal of Cell Biology*, *218*(8), 2481–2491. https://doi.org/10.1083/jcb.201901086

Lee, J. H., Lee, H. Y., & Kim, H. W. (2012). Adhesive proteins linked with focal adhesion kinase regulate neurite outgrowth of PC12 cells. *Acta Biomaterialia*, *8*(1), 165–172. https://doi.org/10.1016/j.actbio.2011.08.024

Li, J., & Lepski, G. (2013). Cell transplantation for spinal cord injury: A systematic review. *BioMed Research International*, *2013*, 786475. https://doi.org/10.1155/2013/786475

Li, W., Tam, K. M. V., Chan, W. W. R., Koon, A. C., Ngo, J. C. K., Chan, H. Y. E., & Lau, K. F. (2018). Neuronal adaptor FE65 stimulates Rac1-mediated neurite outgrowth by recruiting and activating ELMO1. *Journal of Biological Chemistry*, *293*(20), 7674–7688. https://doi.org/10.1074/jbc.RA117.000505

Liang, Y., Zou, Y., Niu, C., & Niu, Y. (2019). Astragaloside IV and ferulic acid synergistically promote neurite outgrowth through Nrf2 activation. *Mechanisms of Ageing and Development*, *180*, 70–81. https://doi.org/10.1016/j.mad.2019.04.002

Lilja, J., & Ivaska, J. (2018). Integrin activity in neuronal connectivity. *Journal of Cell Science*, *131*(12), jcs.212803. https://doi.org/10.1242/jcs.212803

Mills, J., Digicaylioglu, M., Legg, A. T., Young, C. E., Young, S. S., Barr, A. M., … Dedhar, S. (2003). Role of integrin-linked kinase in nerve growth factor-stimulated neurite outgrowth. *Journal of Neuroscience*, *23*(5), 1638–1648.

Moser, M., Legate, K. R., Zent, R., & Fassler, R. (2009). The tail of integrins, talin, and kindlins. *Science*, *324*(5929), 895–899. https://doi.org/10.1126/science.1163865

Nakao, N., Maki, K., Mofrad, M. R. K., & Adachi, T. (2019). Talin is required to increase stiffness of focal molecular complex in its early formation process. *Biochemical and Biophysical Research Communications*, *518*(3), 579–583. https://doi.org/10.1016/j.bbrc.2019.08.091

Neumann, J., & Gottschalk, K. E. (2016). The integrin–talin complex under force. *Protein Engineering, Design & Selection: PEDS*, *29*, 503–512. https://doi.org/10.1093/protein/gzw031

Nieuwenhuis, B., Haenzi, B., Andrews, M. R., Verhaagen, J., & Fawcett, J. W. (2018). Integrins promote axonal regeneration after injury of the nervous system. *Biological Reviews of the Cambridge Philosophical Society*, *93*(3), 1339–1362. https://doi.org/10.1111/brv.12398

Nordenfelt, P., Elliott, H. L., & Springer, T. A. (2016). Coordinated integrin activation by actin-dependent force during T-cell migration. *Nature Communications*, *7*, 13119. https://doi.org/10.1038/ncomms13119

Palazzo, A. F., Eng, C. H., Schlaepfer, D. D., Marcantonio, E. E., & Gundersen, G. G. (2004). Localized stabilization of microtubules by integrin- and FAK-facilitated Rho signaling. *Science*, *303*(5659), 836–839. https://doi.org/10.1126/science.1091325

Pastuhov, S. I., Fujiki, K., Tsuge, A., Asai, K., Ishikawa, S., Hirose, K., … Hisamoto, N. (2016). The core molecular machinery used for engulfment of apoptotic cells regulates the JNK pathway mediating axon regeneration in *Caenorhabditis elegans*. *Journal of Neuroscience*, *36*(37), 9710–9721. https://doi.org/10.1523/JNEUROSCI.0453-16.2016

Qu, Y. Z., Li, M., Zhao, Y. L., Zhao, Z. W., Wei, X. Y., Liu, J. P., … Gao, G. D. (2009). Astragaloside IV attenuates cerebral ischemia-reperfusion-induced increase in permeability of the blood–brain barrier in rats. *European Journal of Pharmacology*, *606*(1–3), 137–141. https://doi.org/10.1016/j.ejphar.2009.01.022

Schubert, P. J., Dorkenwald, S., Januszewski, M., Jain, V., & Kornfeld, J. (2019). Learning cellular morphology with neural networks. *Nature Communications*, *10*(1), 2736. https://doi.org/10.1038/s41467-019-10836-3

Stanslowsky, N., Reinhardt, P., Glass, H., Kalmbach, N., Naujock, M., Hensel, N., … Wegner, F. (2016). Neuronal dysfunction in iPSC-derived medium spiny neurons from chorea-acanthocytosis patients is reversed by Src kinase inhibition and F-actin stabilization. *Journal of Neuroscience*, *36*(47), 12027–12043. https://doi.org/10.1523/JNEUROSCI.0456-16.2016

Sun, Z., Costell, M., & Fassler, R. (2019). Integrin activation by talin, kindlin and mechanical forces. *Nature Cell Biology*, *21*(1), 25–31. https://doi.org/10.1038/s41556-018-0234-9

Sun, Z., Guo, S. S., & Fassler, R. (2016). Integrin-mediated mechanotransduction. *Journal of Cell Biology*, *215*(4), 445–456. https://doi.org/10.1083/jcb.201609037

Suter, D. M., & Miller, K. E. (2011). The emerging role of forces in axonal elongation. *Progress in Neurobiology*, *94*(2), 91–101. https://doi.org/10.1016/j.pneurobio.2011.04.002

Suzuki, N., Numakawa, T., Chou, J., de Vega, S., Mizuniwa, C., Sekimoto, K., … Akazawa, C. (2014). Teneurin-4 promotes cellular protrusion formation and neurite outgrowth through focal adhesion kinase signaling. *FASEB Journal*, *28*(3), 1386–1397. https://doi.org/10.1096/fj.13-241034

Tan, C. L., Kwok, J. C., Heller, J. P., Zhao, R., Eva, R., & Fawcett, J. W. (2015). Full length talin stimulates integrin activation and axon regeneration. *Molecular and Cellular Neuroscience*, *68*, 1–8. https://doi.org/10.1016/j.mcn.2015.03.011

Toriyama, M., Kozawa, S., Sakumura, Y., & Inagaki, N. (2013). Conversion of a signal into forces for axon outgrowth through Pak1-mediated shootin1 phosphorylation. *Current Biology*, *23*(6), 529–534. https://doi.org/10.1016/j.cub.2013.02.017

Wang, X., Wang, Y., Hu, J. P., Yu, S., Li, B. K., Cui, Y., … Zhang, L. D. (2017). Astragaloside IV, a natural PPARgamma agonist, reduces Aβ production in Alzheimer's disease through inhibition of BACE1. *Molecular Neurobiology*, *54*(4), 2939–2949. https://doi.org/10.1007/s12035-016-9874-6

Wang, Y., Zhang, X., Tian, J., Shan, J., Hu, Y., Zhai, Y., & Guo, J. (2019). Talin promotes integrin activation accompanied by generation of tension in talin and an increase in osmotic pressure in neurite outgrowth. *FASEB Journal*, *33*, 6311–6326. https://doi.org/10.1096/fj.201801949RR

Yang, C., Mo, Y., Xu, E., Wen, H., Wei, R., Li, S., … Wang, Q. (2019). Astragaloside IV ameliorates motor deficits and dopaminergic neuron degeneration via inhibiting neuroinflammation and oxidative stress in a Parkinson's disease mouse model. *International Immunopharmacology*, *75*, 105651. https://doi.org/10.1016/j.intimp.2019.05.036

Yang, J., Li, J., Lu, J., Zhang, Y., Zhu, Z., & Wan, H. (2012). Synergistic protective effect of astragaloside IV-tetramethylpyrazine against cerebral ischemic-reperfusion injury induced by transient focal ischemia. *Journal of Ethnopharmacology*, *140*(1), 64–72. https://doi.org/10.1016/j.jep.2011.12.023

Yao, M., Goult, B. T., Klapholz, B., Hu, X., Toseland, C. P., Guo, Y., … Yan, J. (2016). The mechanical response of talin. *Nature Communications*, *7*, 11966. https://doi.org/10.1038/ncomms11966

Yue, R., Li, X., Chen, B., Zhao, J., He, W., Yuan, H., … Zhang, W. (2015). Astragaloside IV attenuates glutamate-induced neurotoxicity in PC12 cells through Raf–MEK–ERK pathway. *PLOS One*, *10*(5), e0126603. https://doi.org/10.1371/journal.pone.0126603

Zhang, C. H., Yang, X., Wei, J. R., Chen, N. M., Xu, J. P., Bi, Y. Q., … Li, M. H. (2019). Ethnopharmacology, phytochemistry, pharmacology, toxicology and clinical applications of radix astragali. *Chinese Journal of Integrative Medicine*. Advance online publication. https://doi.org/10.1007/s11655-019-3032-8

Zhang, J., Wang, Y., Zheng, Z., Sun, X., Chen, T., Li, C., … Guo, J. (2019). Intracellular ion and protein nanoparticle-induced osmotic pressure modify astrocyte swelling and brain edema in response to glutamate stimuli. *Redox Biology*, *21*, 101112. https://doi.org/10.1016/j.redox.2019.101112

Zhang, W. D., Zhang, C., Liu, R. H., Li, H. L., Zhang, J. T., Mao, C., … Chen, C. L. (2006). Preclinical pharmacokinetics and tissue distribution of a natural cardioprotective agent astragaloside IV in rats and dogs. *Life Sciences*, *79*(8), 808–815. https://doi.org/10.1016/j.lfs.2006.02.032

Zhang, X., Li, G., Guo, Y., Song, Y., Chen, L., Ruan, Q., … Guo, J. (2019). Regulation of ezrin tension by *S*-nitrosylation mediates non-small cell lung cancer invasion and metastasis. *Theranostics*, *9*(9), 2555–2571. https://doi.org/10.7150/thno.32479

SUPPORTING INFORMATION

Additional supporting information may be found online in the Supporting Information section.

Neuronal Apolipoprotein E4 Increases Cell Death and Phosphorylated Tau Release in Alzheimer Disease

Anil R. Wadhwani, BA, Amira Affaneh, BS, Stephanie Van Gulden, BS, and
John A. Kessler, MD

Objective: The apolipoprotein E (*APOE*) E4 isoform is the strongest genetic risk factor for sporadic Alzheimer disease (AD). Although *APOE* is predominantly expressed by astrocytes in the central nervous system, neuronal expression of *APOE* is of increasing interest in age-related cognitive impairment, neurological injury, and neurodegeneration. Here, we show that endogenous expression of E4 in stem-cell–derived neurons predisposes them to injury and promotes the release of phosphorylated tau.

Methods: Induced pluripotent stem cells from 2 unrelated AD patients carrying the E4 allele were corrected to the E3/E3 genotype with the CRISPR/Cas9 system and differentiated into pure cultures of forebrain excitatory neurons without contamination from other cells types.

Results: Compared to unedited E4 neurons, E3 neurons were less susceptible to ionomycin-induced cytotoxicity. Biochemically, E4 cells exhibited increased tau phosphorylation and ERK1/2 phosphoactivation. Moreover, E4 neurons released increased amounts of phosphorylated tau extracellularly in an isoform-dependent manner by a heparin sulfate proteoglycan–dependent mechanism.

Interpretation: Our results demonstrate that endogenous expression of E4 by stem-cell–derived forebrain excitatory neurons predisposes neurons to calcium dysregulation and ultimately cell death. This change is associated with increased cellular tau phosphorylation and markedly enhanced release of phosphorylated tau. Importantly, these effects are independent of glial APOE. These findings suggest that E4 accelerates spreading of tau pathology and neuron death in part by neuron-specific, glia-independent mechanisms.

ANN NEUROL 2019;85:726–739

The apolipoprotein E (*APOE*) E4 allele, the strongest genetic risk factor for sporadic Alzheimer disease (AD), differs from the risk-neutral E3 allele by a single nucleotide polymorphism (SNP).[1,2] E4 patients exhibit greater brain atrophy, accumulation of hyperphosphorylated tau protein, and deposition of amyloid, albeit by unclear mechanisms.[3–6] Although most APOE is expressed by astrocytes in the brain,[7–9] neuronal APOE is of increasing interest in age-related cognitive impairment, neurological injury, and neurodegeneration.[10–12] Disease modeling using isogenic stem cells has demonstrated that, compared to E3, expression of E4 leads to distinct transcriptomic differences in multiple neural cell types and increases tau phosphorylation in neurons.[13,14] However, the effects of *APOE* genotype on neuronal viability and tau release are unknown. Using genome editing and a reductionist human stem cell culture approach, we show that endogenous expression of E4 predisposes pure cultures of forebrain excitatory neurons to injury and promotes release of phosphorylated tau (p-tau). These findings suggest that neuronal APOE can accelerate brain atrophy and the spreading of tau pathology in E4-carrying AD patients independently of glia.

Subjects and Methods

Reprogramming and Culture of Stem Cells

Fibroblast lines from patients diagnosed with AD (AD1, AG11414; AD2, AG05810) were described previously[15] and obtained from Coriell Institute for Medical Research. Cells were reprogrammed through Sendai-virus–mediated overexpression of *Oct4*, *Sox2*, *Klf4*, and c-*myc* (Thermo Fisher Scientific, Waltham, MA) per the manufacturer's instructions. Reprogrammed cells were expanded on

View this article online at wileyonlinelibrary.com. DOI: 10.1002/ana.25455

Received Sep 10, 2018, and in revised form Mar 1, 2019. Accepted for publication Mar 4, 2019.

Address correspondence to Dr Wadhwani, Ward 10-233, 303 E Chicago Avenue, Chicago, IL 60611-3078. E-mail: a-wadhwani@northwestern.edu

From the Department of Neurology, Northwestern University, Chicago, IL

gamma-irradiated mouse embryonic fibroblasts (mEFs) in human induced pluripotent stem cell (hiPSC) medium (Dulbecco modified Eagle medium [DMEM]/F-12, 20% Knockout Serum Replacement [Thermo Fisher Scientific], 1% MEM nonessential amino acids [Thermo Fisher Scientific], 1% Glutamax [Thermo Fisher Scientific], and 0.1% 2-mercaptoethanol [Thermo Fisher Scientific]). Cells were visually inspected, and areas of differentiation were removed by manual dissection. Individual clones were manually picked, expanded in feeder-free conditions on Matrigel (Corning Incorporated, Corning, NY) in mTeSR1 (STEMCELL Technologies, Vancouver, BC, Canada), and passaged with ReLeSR (STEMCELL Technologies). Karyotyping (WiCell Research Institute, Madison, WI) was performed, and live cells were stained with Tra 1-81 and SSEA4 (R&D Systems, Minneapolis, MN) to confirm pluripotency prior to cryopreservation in mFrESR (STEMCELL Technologies). Cells were used from passages 5 to 8 after reprogramming for gene editing and passages 8 to 20 for differentiation.

Generation of Isogenic Cell Lines

Genome editing was performed as previously described[16] with modifications. Guide RNA (gRNA) sequence was designed using an online Web tool (crispr.mit.edu), and was cloned into px458 plasmid (Addgene plasmid # 48138, gift of F. Zhang). Prior to editing, cells were dissociated to single-cell suspension with Accutase (Millipore, Billerica, MA), plated in 1:1 mixture of mTeSR1 (STEMCELL Technologies) and mEF-conditioned hiPSC medium supplemented with 10 ng/ml FGF-2 (R&D Systems) and 10 μM ROCK Inhibitor Y-27632 (Stemgent, Cambridge, MA). The next day, cells were cultured in medium without ROCK Inhibitor and grown for 4 to 5 days. Cells were washed with DPBS−/− (Sigma, St Louis, MO), dissociated to single-cell suspension with Accutase, and pelleted. Two million cells were resuspended in 95 μl of Human Nucleofector Solution 1 (Lonza, Basel, Switzerland), 2 μg of px458 containing APOE gRNA, and 100 μM of ssODN template (IDT, Coralville, IA), then transfected with Nucleofector IIb (Lonza) using program B-016. Cells were immediately treated with prewarmed, prebalanced mTeSR1 and transferred to a 10 cm Matrigel-coated dish in media plus 10 μM ROCK Inhibitor Y-27632. After 48 hours, green fluorescent protein–positive cells were sorted by flow cytometry (Aria; BD Biosciences, Franklin Lakes, NJ) and plated at clonal density in media. Individual clones were picked and screened for editing by polymerase chain reaction (PCR) amplification (New England BioLabs, Ipswich, MA) and direct Sanger sequencing (ACGT, Wheeling, IL). Correctly edited clones were expanded in mTeSR1. Karyotyping was performed, and live cells were stained with anti-Tra-1-81 and anti-SSEA4 (R&D Systems) to confirm maintained pluripotency prior to cryopreservation in mFrESR (STEMCELL Technologies). *In silico* predicted off-target sites[17] were directly sequenced.

Preparation of Lentivirus

Lentiviruses were generated in HEK293T cells using psPAX2 and pMD2.G, as described previously.[18] rtTA plasmid was a gift of E. Kiskinis, and pTetO-Ngn2-puro was a gift of M. Wernig (Addgene plasmid # 52047).

Neuronal Differentiation

Cells were differentiated to forebrain excitatory neurons via lentiviral-mediated overexpression of *neurogenin-2*, as previously described[19] with modifications to remove non-neuronal sources of APOE. hiPSCs was dissociated to single cells using Accutase (Millipore), and resuspended in mTeSR1 with 10 μM ROCK Inhibitor Y-27632 with lentiviruses encoding rtTA and pTetO-Ngn2-puro. The next day, medium was changed to KO-DMEM (Thermo Fisher Scientific), 1× MEM nonessential amino acids, 1× Glutamax, and 0.1% 2-mercaptoethanol, supplemented with 10 μM SB431542 (Stemgent), 100 nM LDN193189 (Stemgent), 2 μM XAV939 (Tocris Bioscience, Bristol, UK), and 3 μg/ml doxycycline (Sigma). Medium was gradually changed over 2 days to neural induction medium (DMEM/F-12, MEM nonessential amino acids, Glutamax, D-glucose [Sigma], N-2 [Thermo Fisher Scientific], 2 μg/ml heparin sulfate (Sigma), supplemented with 3 μg/ml doxycycline and 2 μg/ml puromycin [Sigma]). Induced neurons were replated onto tissue culture plates precoated with poly-L-ornithine (Sigma) and laminin (Roche, Basel, Switzerland) and cultured in neuronal maturation medium (BrainPhys Basal Medium [STEMCELL Technologies], B-27 and N-2 Supplements [Thermo Fisher Scientific], MEM nonessential amino acids, and Glutamax, supplemented with 3 μg/ml doxycycline and 10 ng/ml BDNF [R&D Systems]). After replating to eliminate proliferating cells, 2.75 μM Ara-C was used for 2 days. A 50% exchange with fresh neuronal maturation medium was performed every 2 to 3 days thereafter.

Neuronal Morphometry

Live neuronal cultures at 38 days postinduction were imaged by automated phase contrast microscopy with the IncuCyte S3 Live Cell Analysis System (Sartorius Corporation, Edgewood, NY). Somata were manually counted. Neurite length and neurite branch points were determined using automated morphometric analysis on phase contrast images with the IncuCyte NeuroTrack software module (Sartorius Corporation) as previously described[20] using the following parameters: segmentation mode = brightness; segmentation adjustment = 0.2; hole fill = 0; adjust size = 0; minimum cell width = 7 μm; neurite filtering = best; neurite sensitivity = 0.6; neurite width = 2 μm. Neurite length and neurite branches were normalized to the number of somata per field, and the value for each well of a culture plate was determined by the average of at least 3 fields per well. To measure cell survival, live neuronal cultures at 38 days postinduction were treated with propidium iodide (Thermo Fisher Scientific), and cells were again visualized by epifluorescence microscopy using the IncuCyte S3 Live Analysis System. Positive cells were counted using automated morphometric analysis on epifluorescence images with the IncuCyte Basic Analyzer software module using the following parameters: segmentation adjustment = 0; minimum area = 300 μm^2, maximum eccentricity = 0.97. The value for each well of a culture plate was determined by the average of at least 3 fields per well.

Immunoblotting

Cellular proteins were solubilized in M-PER (Bio-Rad Laboratories, Hercules, CA), and protein concentrations were determined by

Pierce Rapid Gold BCA protein assay kit (Thermo Fisher Scientific), subjected to electrophoresis on 4 to 20% Tris-Glycine gels (Bio-Rad Laboratories), and transferred to polyvinylidene difluoride (Millipore). For APOE immunoblotting, recombinant human APOE3 protein and negative control lysate (RayBiotech, Norcross, GA) were used to generate a standard curve. Human adult brain lysate (Novus Biologicals, Littleton, CO) was used as a positive control. Antibodies used were goat anti-APOE (Millipore), rabbit anti–ß3-tubulin (Abcam, Cambridge, MA), donkey antigoat Alexa Fluor 680 (Thermo Fisher Scientific), and donkey antirabbit IRDye 800CW (LI-COR Biosciences, Lincoln, NE). Two exposures are shown for select lanes. Membranes were blocked in 5% normal donkey serum (Jackson ImmunoResearch, West Grove, PA), and signal was detected with an Odyssey CLx Imaging System (LI-COR Biosciences). For all other immunoblots, membranes were blocked with Blotto (Thermo Fisher Scientific) in Tris-buffered saline (Bio-Rad Laboratories). Primary antibodies were mouse anti–total tau (HT7; Thermo Fisher Scientific), mouse anti–p-tau (AT8; Thermo Fisher Scientific), rabbit anti-ERK1/2 (Cell Signaling Technology, Danvers, MA), rabbit anti–phospho-ERK1/2 (Thr202/Tyr204, Cell Signaling Technology), rabbit anti-GSK3ß (Cell Signaling Technology), rabbit anti–phospho-GSK3ß (Ser9, Cell Signaling Technology), anti–amyloid precursor protein (APP; Karen; a gift of V. Lee), and mouse anti–glyceraldehyde-3-phosphate dehydrogenase (GAPDH; Millipore). Secondary antibodies were donkey antimouse horseradish peroxidase (HRP), donkey antirabbit HRP, or donkey antigoat HRP (Cell Signaling Technology). Membranes were incubated with enhanced chemiluminescent substrate (Thermo Fisher Scientific) and developed to film (GE Healthcare Life Sciences, Logan, UT). Quantitation of all blots was performed with ImageJ (NIH, Bethesda, MD).

Immunocytochemistry

Cells were grown on precoated glass coverslips (Neuvitro Corporation, Vancouver, WA) and fixed in 4% paraformaldehyde solution in phosphate-buffered saline. Cells were blocked with bovine serum albumin and normal serum from the species specific to the primary antibodies. Primary antibodies used were mouse IgG2b anti-TuJ1 (Sigma), chicken anti–glial fibrillary acidic protein (GFAP; Sigma), rabbit anti-S100ß (Dako Corporation, Carpinteria, CA), guinea pig anti-vGluT1 (Synaptic Systems, Göttingen, Germany), mouse anti–Tra-1-60 (Thermo Fisher Scientific), goat anti-Oct3/4 (Santa Cruz Biotechnology, Santa Cruz, CA), and rabbit anti-Sox2 (Millipore). Fluorophore-conjugated donkey secondary antibodies against the primary antibody host species IgG were from Thermo Fisher Scientific. Nuclei were counterstained with DAPI (Thermo Fisher Scientific), and cells were mounted using Prolong Gold media (Thermo Fisher Scientific). Cell counts were performed in ImageJ, and values for each genotype and patient background were determined by the average of 3 fields per coverslip and 3 coverslips.

Enzyme-Linked Immunosorbent Assay

Cells were washed with basal media and then incubated for 4 days with a precise volume of fresh complete media. An aliquot of the cell culture supernatant was collected, mixed with Halt protease and phosphatase inhibitor cocktail (Thermo Fisher Scientific), and centrifuged to remove cellular debris. Where indicated, cells were pretreated with 50 mM sodium chlorate ($NaClO_3$, Sigma). Enzyme-linked immunosorbent assays were performed using kits from Thermo Fisher Scientific for Aß40, Aß42, p-tau Thr181, p-tau Ser199, p-tau Thr231, p-tau Ser396, and total tau per the manufacturer's instructions.

Ionomycin Toxicity Assay

Cells were treated with dimethylsulfoxide (DMSO) or 7.5 μM ionomycin (Tocris Bioscience) in complete media, unless otherwise indicated. Cells were visualized by live phase-contrast microscopy using the IncuCyte S3 system as described above while in culture for 48 hours. At the end of the time course, cells were treated with media containing propidium iodide (Thermo Fisher Scientific), and cells were again visualized by epifluorescence microscopy using IncuCyte S3. Morphometric analysis was performed in Neurotrack and Basic Analyzer software (Sartorius Corporation) as described above.

Statistics

All values are reported as mean ± standard error of the mean. All statistical comparisons were between edited E3/E3 neurons of a single patient background and their respective unedited, isogenic, E4/E3 neurons, unless otherwise indicated for drug treatment experiments. The number of patient backgrounds, gene edited stem cell lines, and independent experimental replicates was chosen based on previously published studies.[21–25] A 2-tailed unpaired Student *t* test was used to assess significance between 2 groups. Where multiple analytes were measured from the same sample, the level of significance was corrected for multiple comparisons by the Holm–Sidak method. A 2- or 3-way analysis of variance followed by Sidak multiple comparisons test was used to assess interactions between multiple variables. All statistical calculations were performed with Prism 8 (GraphPad Software, San Diego, CA) software. A probability level of $p < 0.05$ is considered significant for all tests.

Results

Human induced pluripotent stem cells (hiPSCs) were generated from fibroblasts from 2 unrelated individuals (AD1, AD2) with an *APOE* E4/E3 genotype, the most frequent genotype in the AD population.[26] Neurons derived from these hiPSCs were previously shown to exhibit increased amyloid processing, tau phosphorylation, and vulnerability to calcium dysregulation compared to neurons derived from control patient hiPSCs.[15,27] To determine whether the E4 allele influences this cellular phenotype, both E4/E3 hiPSC lines were corrected to E3/E3 genotype by overexpression of Cas9 nuclease, a single guide RNA sequence (sgRNA) targeted to the terminal exon of the gene, and a homology-directed repair template encoding a segment of the E3 allele (Fig 1). Genotypes of the untargeted and edited cell lines were confirmed by PCR amplification and direct Sanger sequencing. Editing did not alter the expression of markers of embryonic stem cells, including Tra-1-60, Oct3/4, or Sox2, and edited hiPSCs exhibited a normal karyotype.

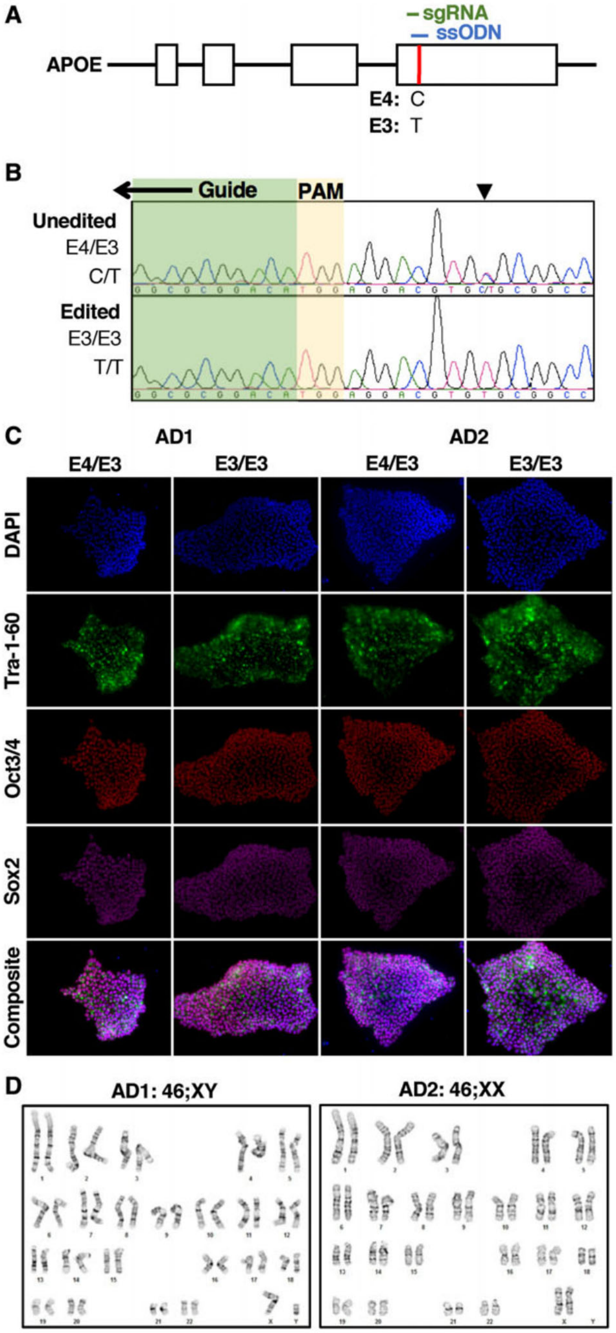

FIGURE 1: Genome editing of E4/E3 human induced pluripotent stem cells (hIPSCs). (A) The *APOE* gene's E3 and E4 alleles are defined by a single nucleotide polymorphism (red) in its terminal exon. The nucleotide code for the E4 and E3 alleles are depicted below. sgRNA (green) = single guide RNA; ssODN (blue), single-stranded oligodeoxynucleotide template for homology-directed repair. (B) Representative chromatograms depicting the targeted editing of a cell line with the E4/E3 genotype (C/T) to E3/E3 (T/T) at the indicated single nucleotide polymorphism *(arrowhead).* A portion of the guide sequence (green) and the positionally adjacent motif (PAM) are indicated. (C) hiPSCs derived from Alzheimer disease patient fibroblasts with E4/E3 genotype expressed characteristic markers of embryonic stem cells. Editing hiPSCs to the E3/E3 genotype did not alter expression of pluripotency markers. (D) Editing iPSCs to the E3/E3 genotype did not alter their karyotype.

The top five in silico predicted off-target binding sites[17] of the sgRNA were PCR-amplified and sequenced, and both edited cell lines were isogenic to their parent lines except for the intended SNP correction in the *APOE* locus.

To assess whether human stem-cell–derived neurons express APOE endogenously, hiPSCs were differentiated to forebrain excitatory neurons via induced overexpression of *neurogenin-2*,[19] with strict modifications to eliminate non-neuronal sources of APOE including glia and fetal bovine serum. Under these stringent conditions, cells expressed ß3-tubulin (TuJ1) and vesicular glutamate transporter 1 (vGluT1), while lacking detectable expression of GFAP or S100ß, demonstrating that hiPSCs differentiated into pure glutamatergic neurons without glial contamination (Fig 2). Isogenic E4/E3 and E3/E3 neurons differentiated with comparable efficiency and survival. There were no differences in soma density or average neurite length per cell in isogenic E4/E3 and E3/E3 neurons. However, E3/E3 neurons exhibited an increased number of neurite branch points per cell compared to unedited isogenic E4/E3 neurons, consistent with previous reports of murine neurons in vivo.[28,29]

Physiologic phosphorylation of cellular tau protein (p-tau) and secretion of 40- and 42-amino acid peptides of amyloid ß (Aß40, Aß42) both steadily increased in our cultures (Fig 3). GAPDH expression increased on the same time course as expected for maturing neurons,[30] and all comparative protein expression analyses were performed on lysates from synchronously differentiated cultures. APOE was detected in the cellular lysate of neurons. The doublet pattern of immunoreactivity mirrored that of human adult brain homogenate and likely represents sialylation, as has been reported previously.[31,32] Recombinant human APOE3 was used to identify full-length unmodified APOE and generate a standard curve. Isogenic E4/E3 and E3/E3 neurons exhibited comparable full-length APOE protein.

We previously reported that AD neurons exhibit an exaggerated glutamate-induced intracellular calcium response and increased susceptibility to calcium dysregulation compared to neurons of cognitively unimpaired patients.[15] In view of the effects of neuronal APOE in aging,[10,11] we used glia-free cultures of forebrain excitatory neurons to examine possible effects of neuronal APOE on cell viability. Cells were treated with DMSO vehicle or ionomycin, a potent calcium ionophore, for 48 hours, and neuronal morphology was observed by live phase-contrast microscopy. In both AD patient backgrounds, ionomycin reduced neurite length, whereas DMSO had no significant effect; however, neurite retraction was significantly reduced in E3/E3 neurons compared to similarly treated isogenic E4/E3 neurons (Fig 4A, C). To confirm this glia-independent effect of APOE isoform, neurons were treated with various doses of ionomycin for

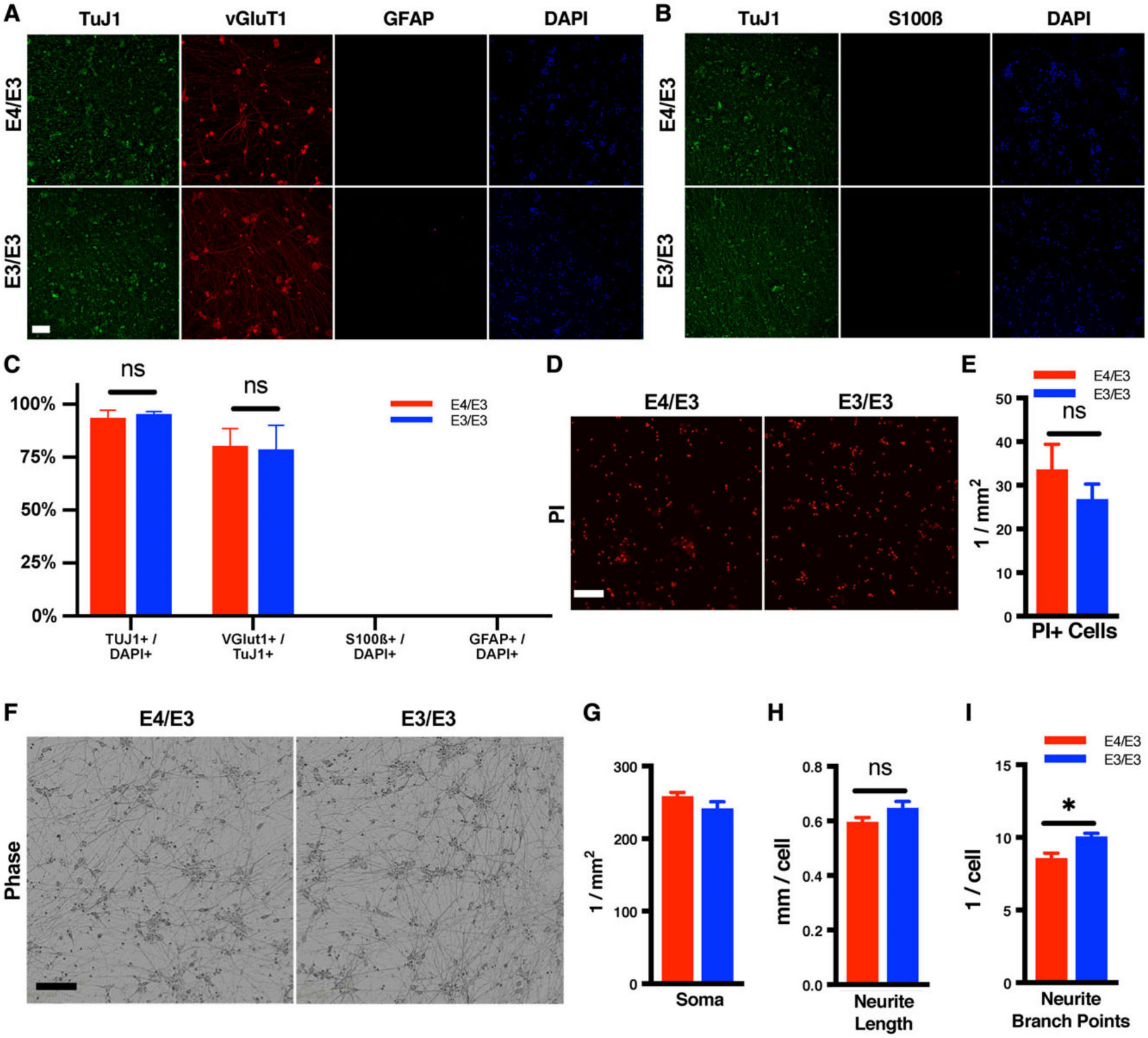

FIGURE 2: **Isogenic E4/E3 and E3/E3 human induced pluripotent stem cells (hiPSCs) differentiate to forebrain excitatory neurons with comparable efficiency, survival, and morphology.** (A, B) Representative photomicrographs of immunostained neuronal cultures with no glial contamination. Cultures were fixed at 38 days postinduction. Nuclei were counterstained with DAPI. (C) Editing iPSCs to the E3/E3 genotype did not alter the differentiation efficiency. Differentiation of isogenic E4/E3 and E3/E3 iPSCs yielded comparable proportions of $\text{vGlut1}^{+}\text{TuJ1}^{+}$ neurons. There were n = 3 independent differentiations per genotype. Each data point is the average of 3 fields per coverslip and 3 coverslips per differentiation. (D) Representative photomicrographs of propidium iodide (PI) labeling of dead cells in isogenic E4/E3 and E3/E3 neurons at 38 days postinduction. (E) Quantitation of PI^{+} dead cells from D. There were n = 4 independent differentiations per genotype. Each data point is the average of 3 fields per differentiation. (F) Representative phase contrast photomicrographs of isogenic E4/E3 and E3/E3 neurons at 38 days postinduction. (G–I) Morphometric analysis of images in F. There were n = 4 independent differentiations per genotype. Each data point is the average of 3 fields per differentiation. For all measures, the statistical test was a 2-tailed unpaired Student *t* test, with Holm–Sidak correction for multiple comparisons: $*p < 0.05$; ns = not significant. Scale bar = 200 μM.

48 hours, and dead cells then were labeled with propidium iodide. Concordant with changes in neuritic morphology, ionomycin was significantly less cytotoxic to E3/E3 neurons than to isogenic E4/E3 neurons at every treatment dose (see Fig 4B, D). These findings demonstrate that endogenous E4 sensitizes human neurons to calcium dysregulation and neurotoxic insult, suggesting that neuronal APOE, independent of glial APOE, is a modifier of genetic risk for and progression of AD.

Alterations in tau and Aß are both central to AD pathogenesis and are separately associated with calcium dysregulation in multiple model systems.[33] Therefore, we next assessed whether neuronal *APOE* genotype altered tau phosphorylation or amyloid processing. There were no

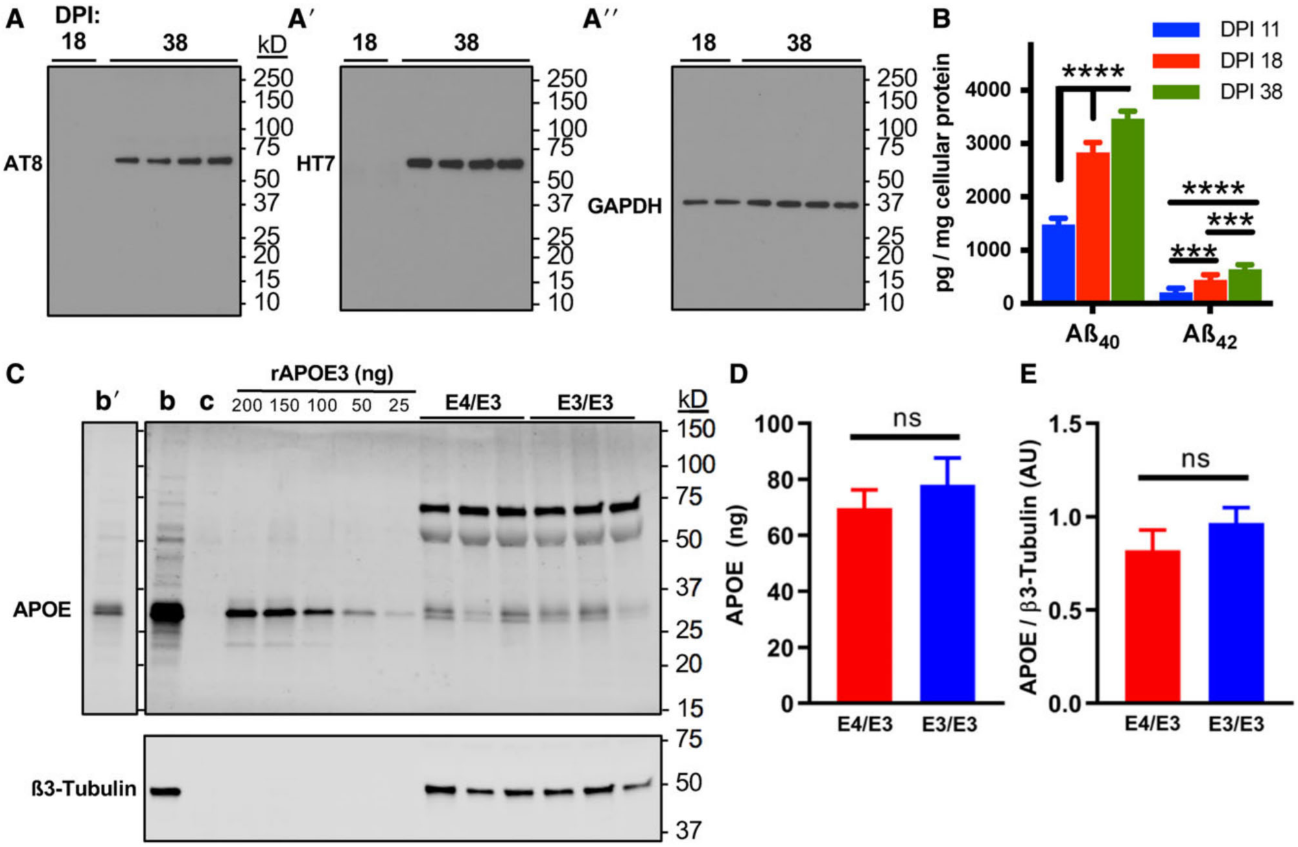

FIGURE 3: Forebrain excitatory neurons express p-tau, Aß, and apolipoprotein E (APOE). (A) Immunoblotting of p-tau detected by AT8, total tau detected by HT7, and glyceraldehyde-3-phosphate dehydrogenase (GAPDH) during the maturation of neuronal cultures at 18 and 38 days postinduction (DPI). Blots were stripped and probed sequentially. (B) Aß40 and Aß42 peptides were detected by peptide-specific immunoassay in the cell culture supernatant of developing and mature neurons by 11 DPI, and secretion increased over time until plateauing by 38 DPI. There were n = 3 independent differentiations. Each data point is the average of 3 measurements per differentiation. The statistical test was a 2-way repeated measures analysis of variance followed by Tukey range test: $***p < 0.001$, $****p < 0.0001$. (C) Isogenic E4/E3 and E3/E3 neurons at 38 DPI express APOE. Representative immunoblot depicts APOE with ß3-tubulin to control for neuronal protein loading. b = positive control human adult brain lysate; c = negative control lysate of HEK293 cells transfected with an empty vector. Recombinant APOE3 (rAPOE3) purified from HEK293 cells was serially diluted to generate a standard curve to quantify the expression of APOE in lysates from E4/E3 and E3/E3 neurons. Human brain lysates are also depicted at a shorter exposure time (b′). (D, E) Absolute (D) and relative (E) quantitation of immunoblotting experiments in C. There were n = 6 independent differentiations. The statistical test was 2-tailed unpaired Student *t* test: ns = not significant.

differences in total tau expression between genotypes, but in both patient backgrounds, the cellular p-tau/tau ratio was significant reduced in E3/E3 neurons compared to isogenic E4/E3 neurons (Fig 5). Contrastingly, *APOE* genotype did not alter the ratio of secreted Aß42/Aß40 or cellular expression of APP. Tau phosphorylation can result from multiple kinase signaling cascades, including calcium-dependent activation of ERK1/2 and Aß-induced activation of GSK3ß.[34] Compared to isogenic E4/E3 neurons, E3/E3 neurons exhibited a significant reduction in the ratio of phosphoactivated to total ERK1/2 in both patient backgrounds but no change in the phosphoactivation of GSK3ß (Fig 6). There was no difference in the total level of expression of either kinase. This finding demonstrates that independent of injury, there is an isoform-dependent and neuron-specific effect of endogenous E4 on kinase activation and tau phosphorylation.

The anatomically stereotyped and progressive spread of p-tau pathology is a fundamental feature of AD and is accelerated in E4-carriers.[35,36] P-tau released by neurons into the cerebrospinal fluid (CSF) is a predictor of progressive cognitive impairment,[37] and presymptomatic patients with the E4-allele exhibit an accelerated p-tau biomarker trajectory compared with E4-noncarriers.[38] Given that E4 increased cellular tau phosphorylation at baseline in our glia-free neuronal cultures, we next examined whether tau release is altered similarly. Strikingly, in both patient backgrounds, the p-tau/tau ratio in the culture media was reduced in E3/E3 neurons compared to isogenic E4/E3 neurons for the Thr181, Thr231, and Ser396 phosphoepitopes (Fig 7A). In CSF, the presence of these epitopes distinguishes between AD and non-AD pathology.[39–41] There was no difference in the level of secretion of total tau protein between the genotypes. We were not able to detect the Ser199 epitope in the cell culture

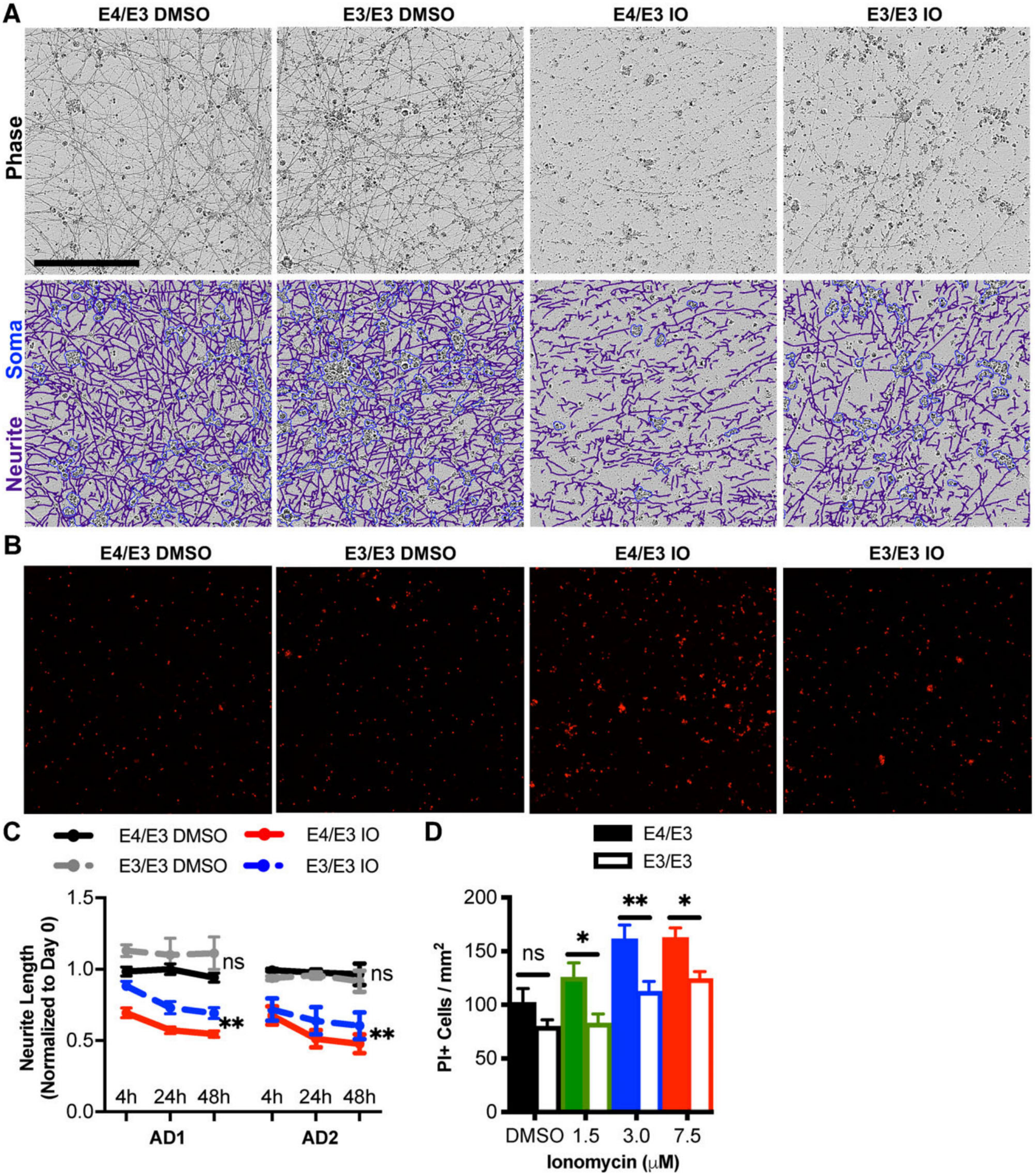

FIGURE 4: **Genetic editing of E4 to E3 protects neurons from ionomycin-induced toxicity.** (A) Phase contrast images of apolipoprotein E (APOE)-isogenic neurons were captured 0, 4, 24, and 48 hours after treatment with ionomycin (IO) or dimethylsulfoxide (DMSO) vehicle. Depicted are representative phase contrast images at 24 hours and corresponding neurite (purple) and cell body (blue) masks beneath. Scale bar = 200 μm. (B) Propidium iodide (PI) epifluorescence labeling dead cells were counted after cultures were treated for 48 hours with 1.5, 3.0, or 7.5 μM IO or DMSO vehicle. Depicted are representative images treated with 7.5 μM IO or DMSO vehicle. (C) Quantitation of neurite lengths from A. There were n = 4 independent treatments per genotype and patient background. Each data point is the average of 3 fields per treatment. The statistical test was a 2-way repeated measures analysis of variance for interaction between *APOE* genotype and time for each drug treatment: $^{**}p < 0.01$; ns = not significant. Not all statistical comparisons are shown for clarity. (D) Quantitation of dead cells from B. There were n = 12 independent treatments per concentration and genotype. The statistical test was 2-way analysis of variance followed by Sidak multiple comparison test for each concentration: $^{*}p < 0.05$, $^{**}p < 0.01$.

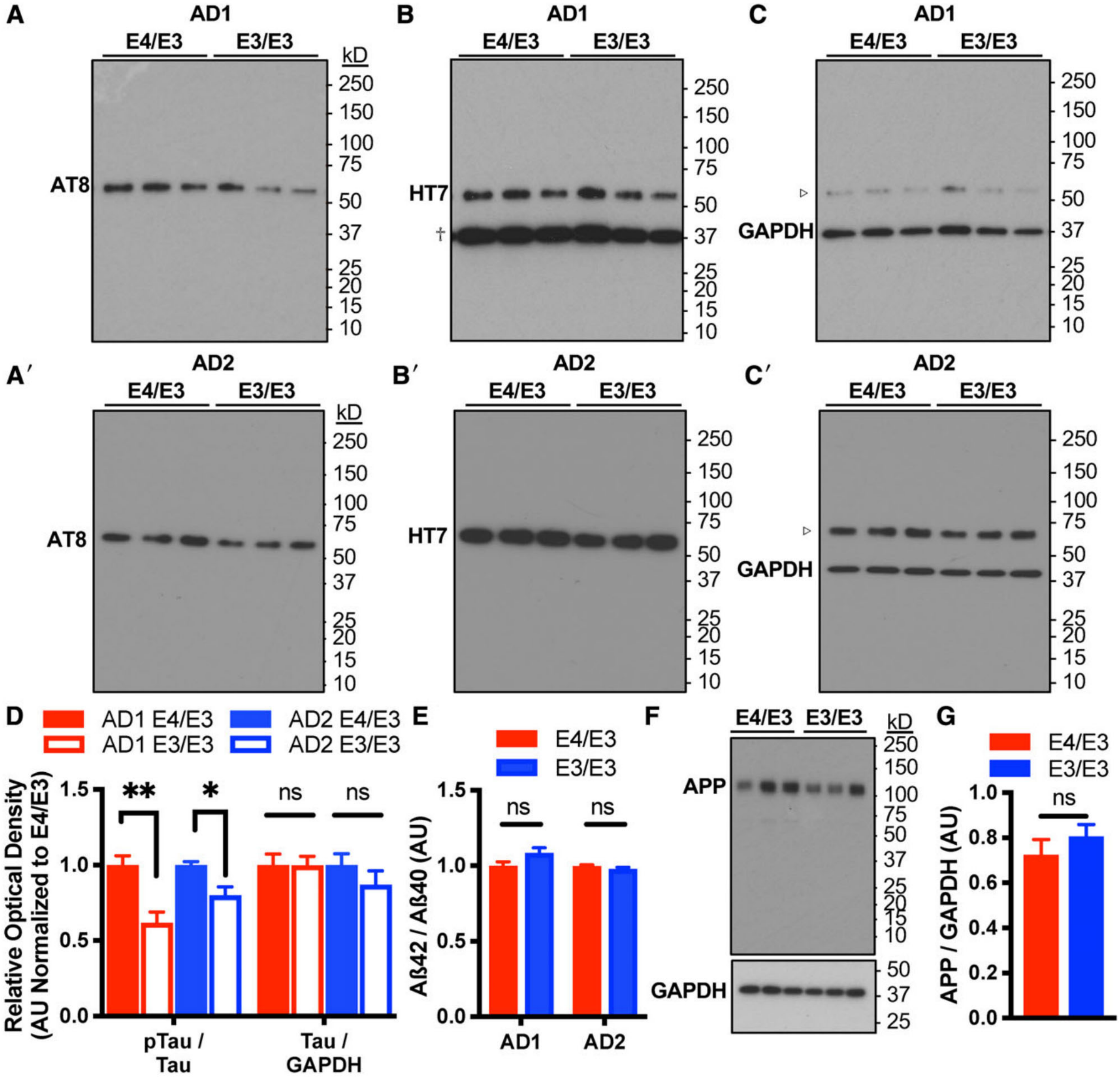

FIGURE 5: **Genetic editing of E4 to E3 reduces tau phosphorylation but not amyloid processing.** (A–C) Representative immunoblotting of lysates of isogenic E4/E3 and E3/E3 neurons from AD1 and AD2 for p-tau (AT8) and total tau (HT7). Blots were stripped and probed sequentially to distinguish phosphorylated and total forms of tau. Glyceraldehyde-3-phosphate dehydrogenase (GAPDH) was used to control for protein loading. HT7 and GAPDH were detected simultaneously. Dagger indicates GAPDH immunoreactivity depicted at a longer exposure time not used for quantitation. Open arrowhead indicates HT7 immunoreactivity depicted at a shorter exposure time not used for quantitation. (D) Quantitation of p-tau/tau ratio and total tau expression. Measures are normalized to the E4/E3 genotype within each patient background. There were n = 6 independent differentiations per genotype and patient background. The statistical test was Student *t* test between isogenic E4/E3 and E3/E3 neuronal lysates with Sidak correction for multiple comparisons: $*p < 0.05$, $**p < 0.01$; ns = not significant. (E) Calculation of the secreted Aß42/Aß40 ratio in the conditioned media of isogenic E4/E3 and E3/E3 neurons detected by enzyme-linked immunoassay. There were n = 5 independent differentiations per genotype and patient background. Each data point is the average of 3 measurements per differentiation. (F) Representative immunoblotting of lysates of isogenic E4/E3 and E3/E3 neurons for amyloid precursor protein (APP; detected with Karen antibody). GAPDH was used to control for protein loading. (G) Quantitation of APP immunoblotting in F. There were n = 6 independent differentiations per genotype. The statistical test was 2-tailed unpaired Student *t* test.

supernatant of either E4/E3 or E3/E3 neurons. There were no differences in cell number or cell death (see Fig 2D–G).

We sought to determine whether this finding simply reflected the overall E4-associated increase of cellular p-tau, or whether E4 also facilitated tau release. In a heterologous expression system, p-tau is released extracellularly by type I unconventional protein secretion, an exosome-independent process dependent on cellular production of heparin sulfate

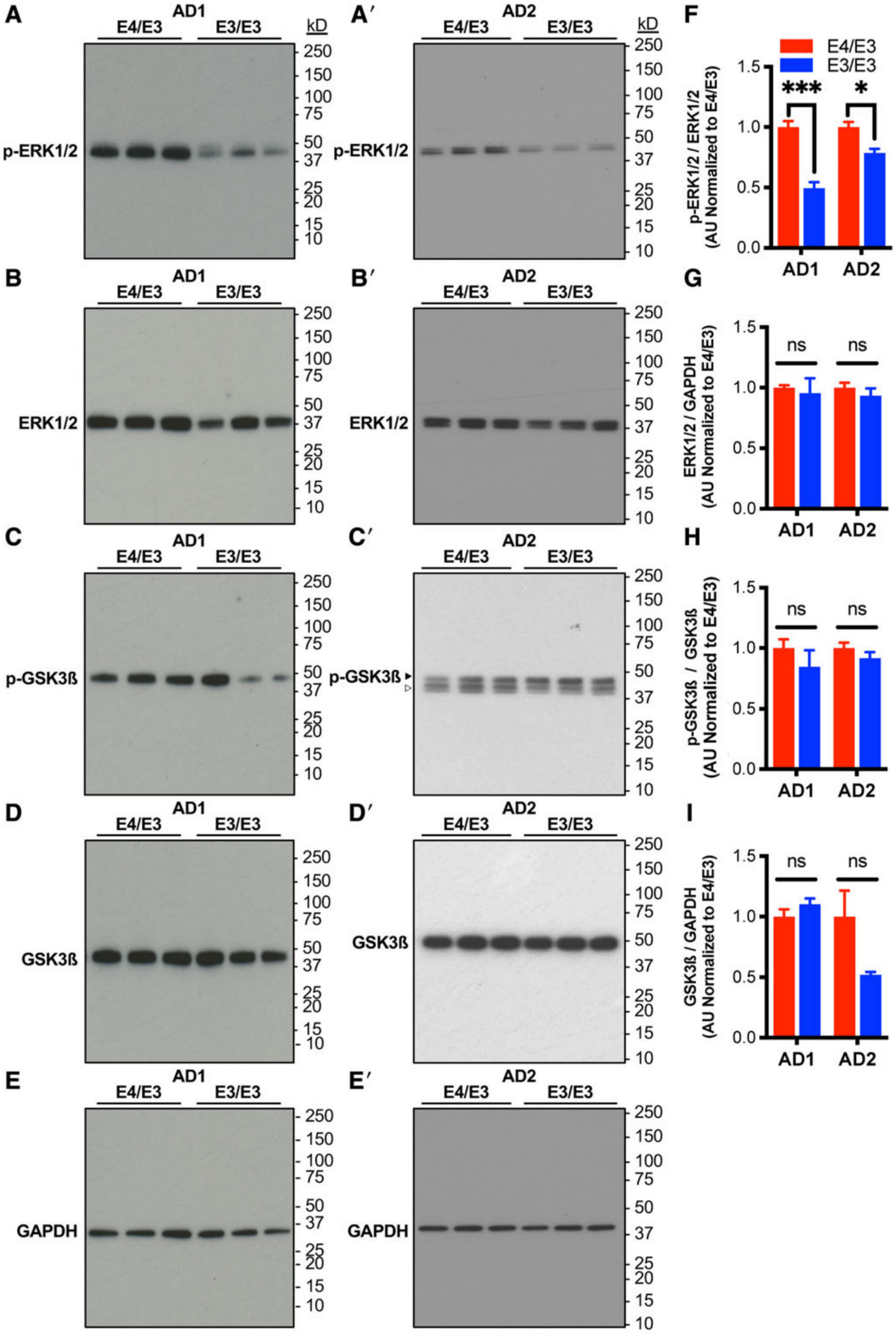

FIGURE 6: **Neurons expressing E4 exhibit increased phosphoactivation of ERK1/2 but not GSK-3ß.** (A–E) Representative immunoblotting of lysates of isogenic E4/E3 and E3/E3 neurons from AD1 and AD2 with antibodies directed against phosphorylated or total ERK1/2 and GSK3ß. Glyceraldehyde-3-phosphate dehydrogenase (GAPDH) was used as a control for protein loading. Blots were stripped and probed sequentially. Open arrowhead indicates residual ERK1/2 immunoreactivity not used for quantitation. (F–I) Quantitation of phosphokinase/total kinase ratio and total kinase expression from A–E. There were n = 6 independent differentiations per genotype and patient background. Measures are normalized to the E4/E3 genotype within each patient background. The statistical test was Student *t* test between isogenic E4/E3 and E3/E3 neuronal lysates with Sidak correction for multiple comparisons: *$p < 0.05$, ***$p < 0.001$; ns = not significant.

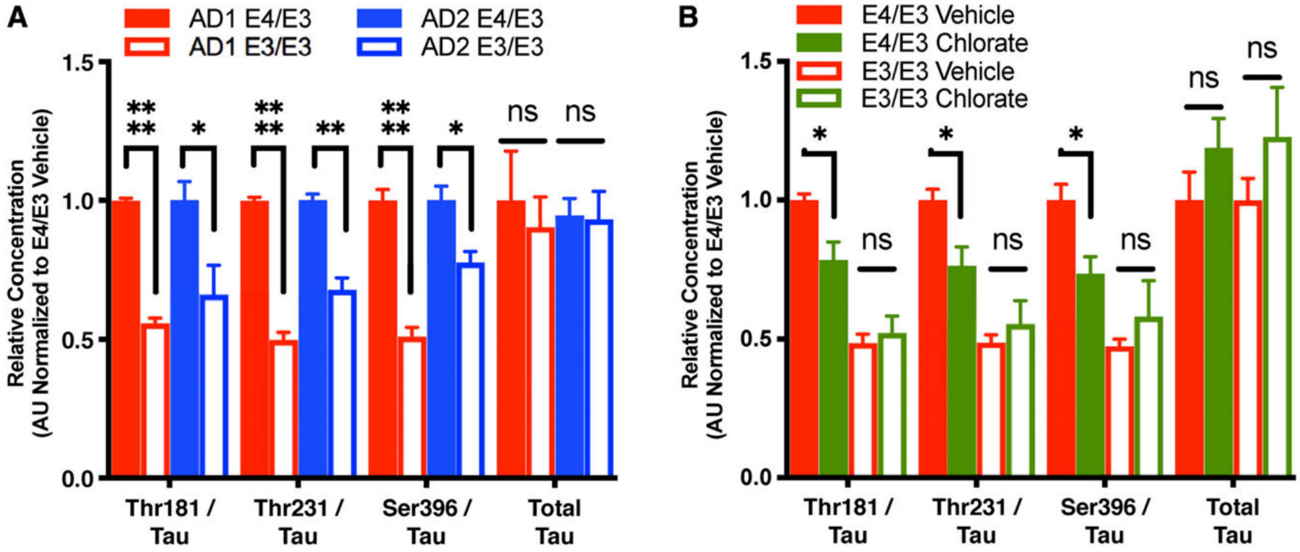

FIGURE 7: **Neuronal E4 increases p-tau release by a heparin sulfate proteoglycan–dependent mechanism.** (A) Calculation of p-tau/tau ratio for each phosphoepitope and total secreted tau in cell culture supernatant of isogenic E4/E3 and E3/E3 neurons from AD1 and AD2. Measures are normalized to the E4/E3 genotype within each patient background. There were n = 4 biologically independent differentiations per genotype and patient background. Each data point is the average of 3 measurements per differentiation. A 3-way interaction between genotype, analyte, and patient background by 3-way analysis of variance was not significant ($F_{3,\ 56} = 0.3128$, $p = 0.8160$); however, there was a main effect of apolipoprotein E (APOE) genotype ($F_{1,\ 56} = 66.39$, $p < 0.0001$). The analysis was therefore followed up with 2-tailed unpaired Student *t* tests between isogenic E4/E3 and E3/E3 neurons for each analyte, with Holm–Sidak correction for multiple comparisons: *$p < 0.05$, **$p < 0.01$, ****$p < 0.0001$; ns = not significant. (B) Calculation of p-tau/tau ratio for each phosphoepitope and total secreted tau in cell culture supernatant of isogenic APOE neurons after 3-day treatment with 50 mM sodium chlorate or saline vehicle. There were n = 3 independent treatments per genotype. Each data point is the average of 3 measurements per treatment. A 3-way interaction between genotype, chlorate treatment, and analyte by 3-way analysis of variance was not significant ($F_{3,\ 32} = 0.7656$, $p = 0.5217$); however, there was a significant interaction between *APOE* genotype and chlorate treatment ($F_{1,\ 32} = 8.666$, $p = 0.006$). The analysis was therefore followed up with 2-way analyses of variance for interaction between *APOE* genotype and treatment for each analyte, followed by Sidak multiple comparison test within each genotype. *$p < 0.05$.

proteoglycans (HSPGs).[42] Pretreatment of E4/E3 neurons with sodium chlorate, which inhibits HSPG biosynthesis,[43] reduced the p-tau/tau ratio for all 3 phosphoepitopes Fig. 7B. Intriguingly, similarly treating isogenic E3/E3 neurons had no effect suggesting that APOE participates in HSPG-dependent p-tau release in an isoform-dependent manner. Chlorate treatment had no effect on total tau protein secretion in either genotype, suggesting that this mechanism of release is specific to p-tau. Taken together, these data suggest that neuronal E4 may contribute to increased tau pathology in AD patients by 2 distinct mechanisms: increased cellular kinase activity and more rapid neuronal release of p-tau.

Discussion

Human stem-cell–based models of AD recapitulate pathophysiologic hallmarks of the disease, including amyloid alterations, tau hyperphosphorylation, and calcium dysregulation, even in the absence of overexpressed mutant alleles that precipitate amyloidosis or tauopathy.[15,44–48] Given this feature, we leveraged the abilities to precisely edit the genome with the CRISPR/Cas9 system and to differentiate hiPSCs into a specific neural subtype to assess whether neuronal expression of APOE contributes to the AD cellular phenotype.

Most APOE in the central nervous system is synthesized and secreted by astrocytes. Neuronalization of a human neural cancer cell line was associated with a decrease of APOE expression suggesting that neurons do not express APOE.[49] However, APOE also has been detected by in situ hybridization and immunofluorescence in primary human neurons in a manner indicative of *de novo* protein synthesis.[12,50] Corroborating this, we find that APOE is expressed by human stem-cell–derived forebrain excitatory neurons. Furthermore, genetic correction of E4 to E3 did not alter the level of APOE expression in neurons, so the genotype-associated differences in cytotoxicity and tau phenotypes observed in the isogenic lines are attributable to APOE isoform-specific effects. Of note, when the human *APOE* alleles are expressed in both neuronal and nonneuronal cells under the control of the endogenous murine promoter, E4 protein expression is reduced compared to E3.[51] The difference between the 2 systems may be due to a cell-type–specific effect at the post-transcriptional or post-translational level, as has been described in other model systems.[47,52] Further experimentation is required to determine whether the differential effects of the E4 and E3 alleles involve gene regulatory elements, post-translational modifications, APOE secretion, or receptor-mediated signaling.

At baseline, E4 neurons exhibited decreased neurite branching per soma compared to isogenic E3 neurons, with no difference in other morphological characteristics. This finding is consistent with a report in murine cortical neurons in which expression of human E4 was associated with reduced dendritic complexity and arborization compared to E3-expressing littermates.[28] The mouse study also noted that E4 reduced apical but not basal dendrite length. In our 2-dimensional culture system, there is no obvious cellular polarity, and we did not detect a difference in average neurite length per soma between *APOE* genotypes. Separately, it was shown that the effect of *APOE* genotype on neurite branching requires neuronal but not astrocytic expression.[29] Taken together, these data suggest that APOE regulates neurite complexity in a cell-intrinsic and isoform-dependent manner, and in future studies, it may be possible to assess whether the gene exerts a similar effect on the length of subsets of neurites of human neurons cultured in a 3-dimensional system.

Although there were no differences between cultures in neurite length at baseline, when cells were subjected to ionomycin-induced calcium dysregulation, E4 neurons exhibited a marked increase in neurite retraction and cell death compared to genetically corrected E3 neurons. Effects of APOE isoform on calcium homeostasis have heretofore been attributed to differential binding of glial APOE on neuronal APOE receptors.[53] Our observations indicate that endogenous expression of E4 in neurons sensitizes them to calcium dysregulation, independently of glial APOE. This finding offers an interesting human correlate to murine models that suggest a toxic gain-of-function role of E4 in neuronal injury and aging.[10,11,54]

Genetic editing of *APOE* also led to multiple distinct effects on tau. We observed an E4-associated increase in tau phosphorylation in pure cultures of forebrain excitatory neurons in both patient backgrounds. Our findings are consistent with previous reports differentiating hiPSCs into mixed cultures of glutamatergic and GABAergic neurons with a minority population of astrocytes.[14,55] Of the many kinases for which tau is a substrate, we found that E4 was associated with increased phosphoactivation of ERK1/2. ERK1/2 interactions are strongly modulated by intracellular calcium,[56] and increased activity of the signaling cascade is consistent with our hypothesis that E4 cells are more sensitive to calcium dysregulation.

In addition, E4 is associated with a remarkable increase in release of p-tau from neurons compared to isogenic E3 neurons, and we show for multiple epitopes a reduction in p-tau after treatment with sodium chlorate to inhibit HSPG biosynthesis. Because p-tau is more readily able to spread trans-synaptically,[57,58] the increase in cellular p-tau may itself increase p-tau release. However, because sodium chlorate treatment had no effect on p-tau release in E3 neurons, our findings raise the interesting possibility that E4 specifically recruits this additional mechanism. Once in the extracellular milieu, p-tau would be accessible to other neurons, either by direct uptake or via other intermediates such as microglia.[59,60] In AD, it has been argued that the highly stereotyped anatomical progression of tau pathology may be attributable to a prion-like, trans-synaptic spreading of tau assemblies,[61] and phosphomimetic tau enhances this process in a transgenic mouse model.[62] The more rapid spread of tau pathology observed in AD patients with the E4 allele[36,37] may therefore be attributable in part to an enhanced release of p-tau by neuronal APOE.

Clinically, E4-carriers exhibit greater amyloid burden. Recombinant E4 has been reported to increase Aß production by receptor-mediated effects,[63] and in transgenic mouse models, E4 promotes the seeding of amyloid plaques.[4,5,63] Aß can in turn induce tau phosphorylation via GSK3ß activation.[64] In our neuronal cultures, genetic correction of E4 did not increase APP expression, Aß42/Aß40 ratio, or GSK3ß phosphoactivation. Therefore, these findings suggest that neuronal *APOE* genotype does not influence amyloid processing or secretion, and furthermore, that the observed effect of APOE on tau in our cultures is likely to be amyloid-independent. The vast majority of Aß and APOE in the central nervous system is released into the extracellular milieu by neurons and astrocytes, respectively, where they interact in an isoform-dependent manner.[65] The effect of APOE on amyloid processing, clearance, and plaque formation is therefore more likely to be a distinct function of glial APOE. Resolving the effects of APOE isoforms in different cell types in vitro will ultimately require a combinatorial coculture model with human neuronal and glial subtypes. The APOE-associated cellular tau phenotype of forebrain excitatory neurons is consistent with reports using alternative hiPSC differentiation strategies yielding mixed populations of neural cells.[13,14] Taken together, these findings suggest that E4 increases tau phosphorylation by a cell-intrinsic mechanism. In contrast, APOE's effect on neuronal Aß depends highly on cellular context; genetic correction of E4 to E3 had no effect in our pure excitatory neuronal cultures but reduced Aß secretion in mixed excitatory and inhibitory neuronal cultures.[13] This suggests that an effect of E4 on Aß release may be activity-dependent.

Discrepancies in these stem-cell–based models stress the importance of cross-validation with intact neural systems. Our morphometric observations both at baseline and in response to calcium dysregulation are consistent with a murine model in which E4 is overexpressed in neurons. However, there is currently no murine AD model in which neuronal APOE's effect on human tau can be modelled *in vivo* without covarying glial APOE. Conditional expression models, in which either human E3 or E4 expression is restricted to a single neural cell type,[10] may prove useful for this purpose when crossed with a knockin line expressing human wild-type tau or a tau variant associated with familial tauopathy.[66] Importantly, our findings only demonstrate a role for neuronal APOE in AD pathophysiology, and editing of hiPSCs from nondemented control patients will be required to determine whether these effects are generalizable to aging or other disorders.

In summary, although it is widely believed that astrocytic and microglial APOE mediates the gene's effect on neurodegeneration in AD,[52,67] we demonstrate that endogenous expression of E4 in neurons is sufficient to alter multiple AD-relevant cellular pathways. Notably, E4-expressing human neurons are more susceptible to neurotoxic insult. Moreover, neuronal E4 increases both tau phosphorylation and its release, possibly explaining the more rapid progression of tau pathology and cognitive impairment experienced by E4-carrying patients. Our observations indicate that APOE predisposes neurons to injury and accelerates neurodegeneration, at least in part, by a glia-independent mechanism. Almost certainly, APOE from non-neuronal sources has combinatorial but distinct effects, for instance on amyloid clearance and neuroinflammation. APOE's multiple cell-type–specific effects may explain why the gene has been an elusive target for drug discovery despite its strong clinical correlates. Targeting neuron-specific effects of APOE, for example by reducing ERK1/2 activity, may slow tau spreading and offer a more successful neuroprotective strategy in E4-carriers.

Acknowledgment

This project was supported by NIH-NIA grant R01 AG054429 to J.A.K. A.R.W. was supported by NIH-NIA training grants F30AG051327 and T32AG20506, and NIH-NIGMS training grant T32GM008152.

We thank Drs L. Lyass and C.-Y. Peng for technical assistance.

Author Contributions

Conception and design of the study: A.R.W., J.A.K
Acquisition and analysis of data: A.R.W., A.A., S.V.G., J.A.K.
Drafting the text or preparing figures: A.R.W., A.A., S.V.G., J.A.K.

Potential Conflicts of Interest

Nothing to report.

References

1. Corder EH, Saunders AM, Strittmatter J, et al. Gene dose of apolipoprotein E type 4 allele and the risk of Alzheimer's disease in late onset families. Science 1993;261:921–923.
2. Strittmatter WJ, Saunders AM, Schmechel D, et al. Apolipoprotein E: high-avidity binding to beta-amyloid and increased frequency of type 4 allele in late-onset familial Alzheimer disease. Proc Natl Acad Sci U S A 1993;90:1977–1981.
3. Shi Y, Yamada K, Liddelow SA, et al. ApoE4 markedly exacerbates tau-mediated neurodegeneration in a mouse model of tauopathy. Nature 2017;549:523–527.
4. Huynh T-PV, Liao F, Francis CM, et al. Age-dependent effects of apoE reduction using antisense oligonucleotides in a model of β-amyloidosis. Neuron 2017;96:1013–1023.e4.
5. Liu C-C, Zhao N, Fu Y, et al. ApoE4 accelerates early seeding of amyloid pathology. Neuron 2017;96:1024–1032.e3.
6. Yasuda M, Mori E, Kitagaki H, et al. Apolipoprotein E epsilon 4 allele and whole brain atrophy in late-onset Alzheimer's disease. Am J Psychiatry 1998;155:779–784.
7. Raber J, Wong D, Buttini M, et al. Isoform-specific effects of human apolipoprotein E on brain function revealed in ApoE knockout mice: increased susceptibility of females. Proc Natl Acad Sci U S A 1998; 95:10914–10919.
8. Holtzman DM, Herz J, Bu G. Apolipoprotein E and apolipoprotein E receptors: normal biology and roles in Alzheimer disease. Cold Spring Harb Perspect Med 2012;2:a006312.
9. Huang Y, Mucke L. Alzheimer mechanisms and therapeutic strategies. Cell 2012;148:1204–1222.
10. Knoferle J, Yoon SY, Walker D, et al. Apolipoprotein e4 produced in GABAergic interneurons causes learning and memory deficits in mice. J Neurosci 2014;34:14069–14078.
11. Buttini M, Masliah E, Yu G-Q, et al. Cellular source of apolipoprotein E4 determines neuronal susceptibility to excitotoxic injury in transgenic mice. Am J Pathol 2010;177:563–569.
12. Xu Q, Bernardo A, Walker D, et al. Profile and regulation of apolipoprotein E (ApoE) expression in the CNS in mice with targeting of green fluorescent protein gene to the ApoE locus. J Neurosci 2006; 26:4985–4994.
13. Lin Y-T, Seo J, Gao F, et al. APOE4 Causes widespread molecular and cellular alterations associated with Alzheimer's disease phenotypes in human iPSC-derived brain cell types. Neuron 2018;98:1294.
14. Wang C, Najm R, Xu Q, et al. Gain of toxic apolipoprotein E4 effects in human iPSC-derived neurons is ameliorated by a small-molecule structure corrector. Nat Med 2018;24:647–657.
15. Duan L, Bhattacharyya BJ, Belmadani A, et al. Stem cell derived basal forebrain cholinergic neurons from Alzheimer's disease patients are more susceptible to cell death. Mol Neurodegener 2014;9:3.
16. Ran FA, Hsu PD, Wright J, et al. Genome engineering using the CRISPR-Cas9 system. Nat Protoc 2013;8:2281–2308.
17. Hsu PD, Scott DA, Weinstein JA, et al. DNA targeting specificity of RNA-guided Cas9 nucleases. Nat Biotechnol 2013;31:827–832.
18. Zufferey R, Dull T, Mandel RJ, et al. Self-inactivating lentivirus vector for safe and efficient in vivo gene delivery. J Virol 1998;72:9873–9880.
19. Zhang Y, Pak C, Han Y, et al. Rapid single-step induction of functional neurons from human pluripotent stem cells. Neuron 2013;78: 785–798.
20. Mengel D, Hong W, Corbett GT, et al. PrP-grafted antibodies bind certain amyloid β-protein aggregates, but do not prevent toxicity. Brain Res 2018;pii:S0006-8993(18)30664-4
21. Xu X, Tay Y, Sim B, et al. Reversal of phenotypic abnormalities by CRISPR/Cas9-mediated gene correction in Huntington disease

patient-derived induced pluripotent stem cells. Stem Cell Reports 2017;8:619–633.

22. Imamura K, Sahara N, Kanaan NM, et al. Calcium dysregulation contributes to neurodegeneration in FTLD patient iPSC-derived neurons. Sci Rep 2016;6:34904.
23. Reinhardt P, Schmid B, Burbulla LF, et al. Genetic correction of a LRRK2 mutation in human iPSCs links parkinsonian neurodegeneration to ERK-dependent changes in gene expression. Stem Cell 2013;12:354–367.
24. Murakami N, Imamura K, Izumi Y, et al. Proteasome impairment in neural cells derived from HMSN-P patient iPSCs. Mol Brain 2017; 10:771.
25. Paquet D, Kwart D, Chen A, et al. Efficient introduction of specific homozygous and heterozygous mutations using CRISPR/Cas9. Nature 2016;533:125–129.
26. Farrer LA, Cupples LA, Haines JL, et al. Effects of age, sex, and ethnicity on the association between apolipoprotein E genotype and Alzheimer disease. A meta-analysis. APOE and alzheimer disease meta analysis consortium. JAMA 1997;278:1349–1356.
27. Kim H, Yoo J, Shin J, et al. Modelling APOE ε3/4 allele-associated sporadic Alzheimer's disease in an induced neuron. Brain 2017;140: 2193–2209.
28. Dumanis SB, Tesoriero JA, Babus LW, et al. ApoE4 decreases spine density and dendritic complexity in cortical neurons in vivo. J Neurosci 2009;29:15317–15322.
29. Jain S, Yoon SY, Leung L, et al. Cellular source-specific effects of apolipoprotein (Apo) E4 on dendrite arborization and dendritic spine development. PLoS One 2013;8:e59478.
30. Zhou L, Lim Q-E, Wan G, Too H-P. Normalization with genes encoding ribosomal proteins but not GAPDH provides an accurate quantification of gene expressions in neuronal differentiation of PC12 cells. BMC Genomics 2010;11:75.
31. Brecht WJ, Harris FM, Chang S, et al. Neuron-specific apolipoprotein e4 proteolysis is associated with increased tau phosphorylation in brains of transgenic mice. J Neurosci 2004;24:2527–2534.
32. Pitas RE, Boyles JK, Lee SH, et al. Astrocytes synthesize apolipoprotein E and metabolize apolipoprotein E-containing lipoproteins. Biochim Biophys Acta 1987;917:148–161.
33. Alzheimer's Association Calcium Hypothesis Workgroup. Calcium hypothesis of Alzheimer's disease and brain aging: a framework for integrating new evidence into a comprehensive theory of pathogenesis. Alzheimers Dement 2017;13:178–182.e17.
34. Brunden KR, Trojanowski JQ, Lee VMY. Advances in tau-focused drug discovery for Alzheimer's disease and related tauopathies. Nat Rev Drug Discov 2009;8:783–793.
35. Braak H, Braak E. Neuropathological staging of Alzheimer-related changes. Acta Neuropathol 1991;82:239–259.
36. Ohm TG, Kirca M, Bohl J, et al. Apolipoprotein E polymorphism influences not only cerebral senile plaque load but also Alzheimer-type neurofibrillary tangle formation. Neuroscience 1995;66: 583–587.
37. Olsson B, Lautner R, Andreasson U, et al. CSF and blood biomarkers for the diagnosis of Alzheimer's disease: a systematic review and meta-analysis. Lancet Neurol 2016;15:673–684.
38. Sutphen CL, Jasielec MS, Shah AR, et al. Longitudinal cerebrospinal fluid biomarker changes in preclinical Alzheimer disease during middle age. JAMA Neurol 2015;72:1029.
39. Buerger K, Zinkowski R, Teipel SJ, et al. Differential diagnosis of Alzheimer disease with cerebrospinal fluid levels of tau protein phosphorylated at threonine 231. Arch Neurol 2002;59:1267–1272.
40. Hampel H, Buerger K, Zinkowski R, et al. Measurement of phosphorylated tau epitopes in the differential diagnosis of Alzheimer disease: a comparative cerebrospinal fluid study. Arch Gen Psychiatry 2004; 61:95–102.
41. Buerger K, Ewers M, Pirttilä T, et al. CSF phosphorylated tau protein correlates with neocortical neurofibrillary pathology in Alzheimer's disease. Brain 2006;129:3035–3041.
42. Katsinelos T, Zeitler M, Dimou E, et al. Unconventional secretion mediates the trans-cellular spreading of tau. Cell Rep 2018;23:2039–2055.
43. Safaiyan F, Kolset SO, Prydz K, et al. Selective effects of sodium chlorate treatment on the sulfation of heparan sulfate. J Biol Chem 1999;274:36267–36273.
44. Muratore CR, Rice HC, Srikanth P, et al. The familial Alzheimer's disease APPV717I mutation alters APP processing and Tau expression in iPSC-derived neurons. Hum Mol Genet 2014;23:3523–3536.
45. Yagi T, Ito D, Okada Y, et al. Modeling familial Alzheimer's disease with induced pluripotent stem cells. Hum Mol Genet 2011;20:4530–4539.
46. Sproul AA, Jacob S, Pre D, et al. Characterization and molecular profiling of PSEN1 familial Alzheimer's disease iPSC-derived neural progenitors. PLoS One 2014;9:e84547.
47. Kondo T, Asai M, Tsukita K, et al. Modeling Alzheimer's disease with iPSCs reveals stress phenotypes associated with intracellular Aβ and differential drug responsiveness. Cell Stem Cell 2013;12: 487–496.
48. Israel MA, Yuan SH, Bardy C, et al. Probing sporadic and familial Alzheimer's disease using induced pluripotent stem cells. Nature 2012;482:216–220.
49. Ferreira S, Dupire M, Delacourte A, et al. Synthesis and regulation of apolipoprotein E during the differentiation of human neuronal precursor NT2/D1 cells into postmitotic neurons. Exp Neurol 2000;166: 415–421.
50. Dekroon RM, Armati PJ. Synthesis and processing of apolipoprotein E in human brain cultures. Glia 2001;33:298–305.
51. Sullivan PM, Han B, Liu F, et al. Reduced levels of human apoE4 protein in an animal model of cognitive impairment. Neurobiol Aging 2011;32:791–801.
52. Xu Q, Walker D, Bernardo A, et al. Intron-3 retention/splicing controls neuronal expression of apolipoprotein E in the CNS. J Neurosci 2008;28:1452–1459.
53. Lane-Donovan C, Herz J. ApoE, ApoE receptors, and the synapse in Alzheimer's disease. Trends Endocrinol Metab 2017;28:273–284.
54. Tesseur I, Van Dorpe J, Bruynseels K, et al. Prominent axonopathy and disruption of axonal transport in transgenic mice expressing human apolipoprotein E4 in neurons of brain and spinal cord. Am J Pathol 2000;157:1495–1510.
55. Chambers SM, Fasano CA, Papapetrou EP, et al. Highly efficient neural conversion of human ES and iPS cells by dual inhibition of SMAD signaling. Nat Biotechnol 2009;27:275–280.
56. Agell N, Bachs O, Rocamora N, Villalonga P. Modulation of the Ras/Raf/MEK/ERK pathway by Ca(2+), and calmodulin. Cell Signal 2002;14:649–654.
57. Strittmatter WJ, Saunders AM, Goedert M, et al. Isoform-specific interactions of apolipoprotein-E with microtubule-associated protein tau: implications for Alzheimer disease. Proc Natl Acad Sci U S A 1994;91:11183–11186.
58. Futamura M, Dhanasekaran P, Handa T, et al. Two-step mechanism of binding of apolipoprotein E to heparin: implications for the kinetics of apolipoprotein E-heparan sulfate proteoglycan complex formation on cell surfaces. J Biol Chem 2005;280:5414–5422.
59. Asai H, Ikezu S, Tsunoda S, et al. Depletion of microglia and inhibition of exosome synthesis halt tau propagation. Nat Neurosci 2015; 18:1584–1593.
60. Maphis N, Xu G, Kokiko-Cochran ON, et al. Reactive microglia drive tau pathology and contribute to the spreading of pathological tau in the brain. Brain 2015;138:1738–1755.

61. Jucker M, Walker LC. Self-propagation of pathogenic protein aggregates in neurodegenerative diseases. Nature 2014;501: 45–51.

62. Iba M, Guo JL, McBride JD, et al. Synthetic tau fibrils mediate transmission of neurofibrillary tangles in a transgenic mouse model of Alzheimer's-like tauopathy. J Neurosci 2013;33:1024–1037.

63. Huang Y-WA, Zhou B, Wernig M, Südhof TC. ApoE2, ApoE3, and ApoE4 differentially stimulate APP transcription and Aβ secretion. Cell 2017;168:427–441.e21.

64. Takashima A, Noguchi K, Michel G, et al. Exposure of rat hippocampal neurons to amyloid β peptide (25–35) induces the inactivation of phosphatidyl inositol-3 kinase and the activation of tau protein kinase I/glycogen synthase kinase-3β. Neurosci Lett 1996; 203:33–36.

65. Ladu MJ, Falduto MT, Manelli AM, et al. Isoform-specific binding of apolipoprotein-E to beta-amyloid. J Biol Chem 1994;269:23403–23406.

66. Frank S, Clavaguera F, Tolnay M. Tauopathy models and human neuropathology: similarities and differences. Acta Neuropathol 2007; 115:39–53.

67. González-Reyes RE, Nava-Mesa MO, Vargas-Sánchez K, et al. Involvement of astrocytes in Alzheimer's disease from a neuroinflammatory and oxidative stress perspective. Front Mol Neurosci 2017;10:50.

Application Note

January 20, 2023

Keywords or phrases:
Neuroscience, Neurite Outgrowth, Neuroprotection, iPSC, Cell Analysis Systems

Quantification of Neurite Dynamics in Mono-cultures and Co-cultures Using the Incucyte® Live-Cell Analysis System

Jasmine Trigg[1], John Rauch[2], Libby Oupicka[2], Nevine Holtz[2], Eric Endsley[2], Timothy Dale[1]*
[1] Sartorius UK Ltd., Royston, Hertfordshire, UK
[2] Sartorius Corporation, Ann Arbor, MI, USA
*With thanks to Susana L. Alcantara, Tom Campbell (talisman-therapeutics.com), Timothy Jackson, Aaron Overland, Jeremiah Brown, Tricia Garay

Introduction

Neurite dynamics play a fundamental role in the development and function of the nervous system. Formation and maintenance of synaptic networks are necessary for healthy brain function and plasticity and occurs through continuous changes in the fine structure of neurons. Neurite dynamics can be altered in disease states, injury, or following exposure to neurotoxic agents. Monitoring neuronal morphology in long-term *in vitro* cell cultures is critical for the characterization and evaluation of disease models and to understand neuronal development. Ideally, approaches to track neurite dynamics would allow continuous automated measurements of structural parameters, including neurite length and number of branch points. These methods should be non-perturbing and enable quantification of neurons in mono- or co-culture with glia.

This application note describes the use of live-cell imaging to kinetically quantify neuronal outgrowth using the Incucyte® Live-Cell Analysis System in conjunction with the Incucyte® Neurotrack Analysis Software Module. This assay permits the analysis of neurons in mono-culture (label-free) or in co-culture with astrocytes (Figure 1), using a non-perturbing Incucyte® Neurolight Red or Orange Lentivirus for continuous analysis of neurite length and branch points. Furthermore, the neurite analysis assay can be multiplexed with cell health reagents, Incucyte® Annexin V Red, Orange, or NIR Dye, to determine the onset of apoptosis in real time.

Find out more: www.sartorius.com/incucyte-neurite-outgrowth

Mono-culture: Primary Rat Cortical Neurons

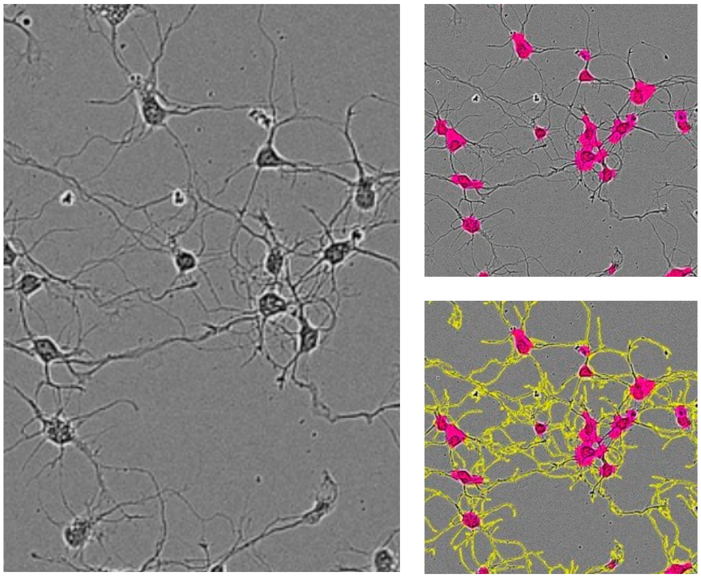

Co-culture: Primary Rat Cortical Neurons + Rat Astrocytes

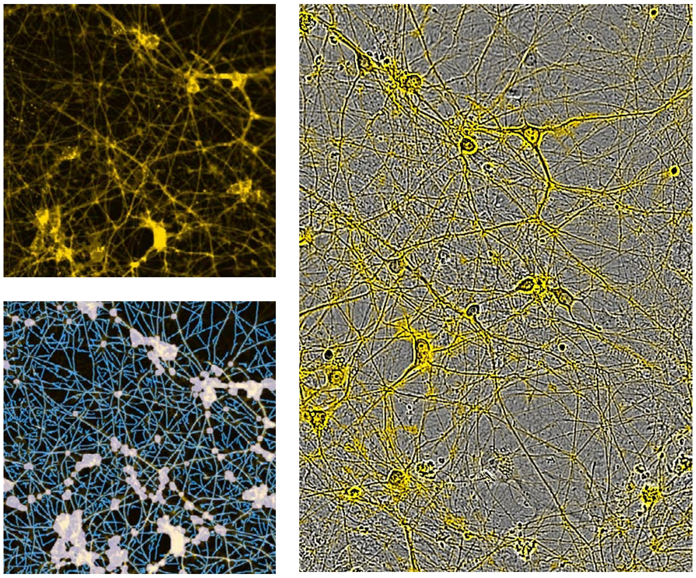

Figure 1

Automated Analysis and Visualization of Neuronal Mono-cultures and Co-cultures

Analysis of primary rat cortical neuron structures using label-free segmentation masking (top panel) showing phase image of neurons at Day 5 post-seeding, cell body cluster (pink), and neurite masks (yellow). Assessment of neurite structures in co-culture with astrocytes using Incucyte® Neurolight Orange Lentivirus (bottom panel) at Day 7 post-infection, cell body cluster (white), and neurite masks (blue).

Assay Principle and Quantification

An overview of the workflow to enable quantification of neurite outgrowth is represented in Figure 2. For mono-cultures, label-free measurements are enabled by direct phase imaging post cell seeding. When co-cultures are preferred, an initial infection with Incucyte® Neurolight Lentivirus is required to visualize the neurons. Optimization of cell density, well coatings, multiplicity of infection (MOI), and viral exposure time are required based on the research model used.

The Incucyte® Neurolight Lentivirus is a live-cell neuronal labeling reagent driven by a synapsin promoter, resulting in the long-term expression of red (mKate2) or orange (TagRFP) fluorescent protein in neuronal cell bodies and neurites. The Incucyte® Neurolight Lentivirus ensures highly efficient, yet non-disruptive labeling of primary or induced pluripotent stem cells (iPSC)-derived neurons over weeks enabling the kinetic quantification of neurite length and branching in the presence of astrocytes and other non-neuronal cell types. Purpose-built integrated Incucyte® Neurotrack Analysis Software automatically segments phase or fluorescent images and generates full time-course plots for each well in 96- and 384-well plates. Metrics such as Total Neurite Length (mm/mm^2), Branch Points (count/mm^2), Cell Body Clusters (count or area/mm^2), or Nuclear Count (for cells with a nuclear fluorescent label), and corresponding normalization values are generated in real time.

Finally, combining novel, non-perturbing reagents that deploy longer wavelength fluorophores designed for neuronal-specific measurements along with lab-tested protocols ensures reproducible and unprecedented access to phenotypic information.

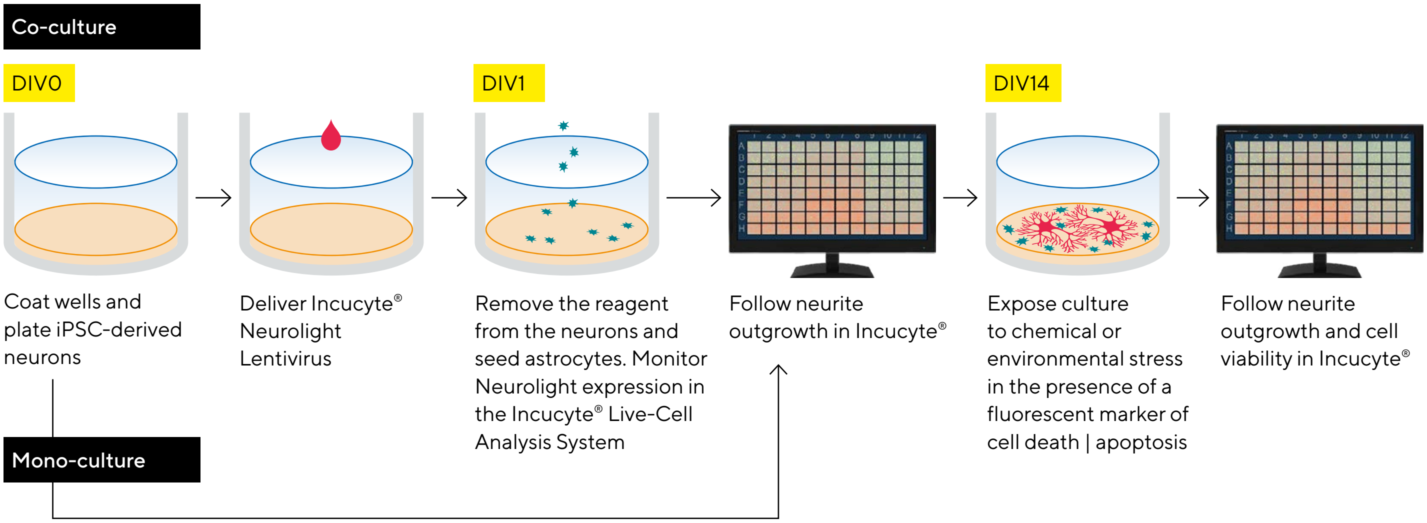

Coat wells and plate iPSC-derived neurons

Deliver Incucyte® Neurolight Lentivirus

Remove the reagent from the neurons and seed astrocytes. Monitor Neurolight expression in the Incucyte® Live-Cell Analysis System

Follow neurite outgrowth in Incucyte®

Expose culture to chemical or environmental stress in the presence of a fluorescent marker of cell death | apoptosis

Follow neurite outgrowth and cell viability in Incucyte®

Figure 2

Quick Guide of Neurite Outgrowth Assay Workflow for Both Mono-culture and Co-culture Models

This simplified workflow enables label-free quantification of neurite dynamics in mono-culture or utilizes the Incucyte® Neurolight Orange Lentivirus for non-perturbing fluorescence analysis of neurons in co-culture. Using the Incucyte® Live-Cell Analysis System, visualize and quantify long-term changes in neurite outgrowth alongside optional readouts of cell viability using fluorescence cell death reporters.

Measuring Neuronal Parameters in Mono-cultures

A major limitation in studying human diseases affecting the nervous system is the ability to culture, monitor, and analyze neuronal cells that accurately represent human phenotypes of these disorders. The use of human-induced pluripotent stem cell (hiPSC)-derived neurons has provided a valuable approach aimed at modeling neurological diseases in humanized models. Monitoring neuronal morphology in long-term cultures is critical for the characterization and evaluation of these advanced model systems. Continuous real-time monitoring offers a significant advantage as it provides a more physiologically relevant picture of neuronal cell behavior, allows for non-invasive, repeated measurements of the same neuronal networks over time, and enables the capture of rare or transient events that are often missed with end-point assays.

When external modification of precious cellular models is not an option, either to minimize handling and perturbance (stem cells) or due to difficulties of genetic modification (primary cells), label-free phase imaging of seeded cultures provides an optimal solution. Figure 3 exemplifies the value of quantifying neuronal outgrowth in such environments and provides an example of the power of automatic segmentation and quantification. These metrics quantify biologically relevant processes such as neurite extension, branching, and loss of neurite length due to retraction or fragmentation. Statistical data, such as standard deviation and standard error of the mean, are automatically produced for user-defined replicates.

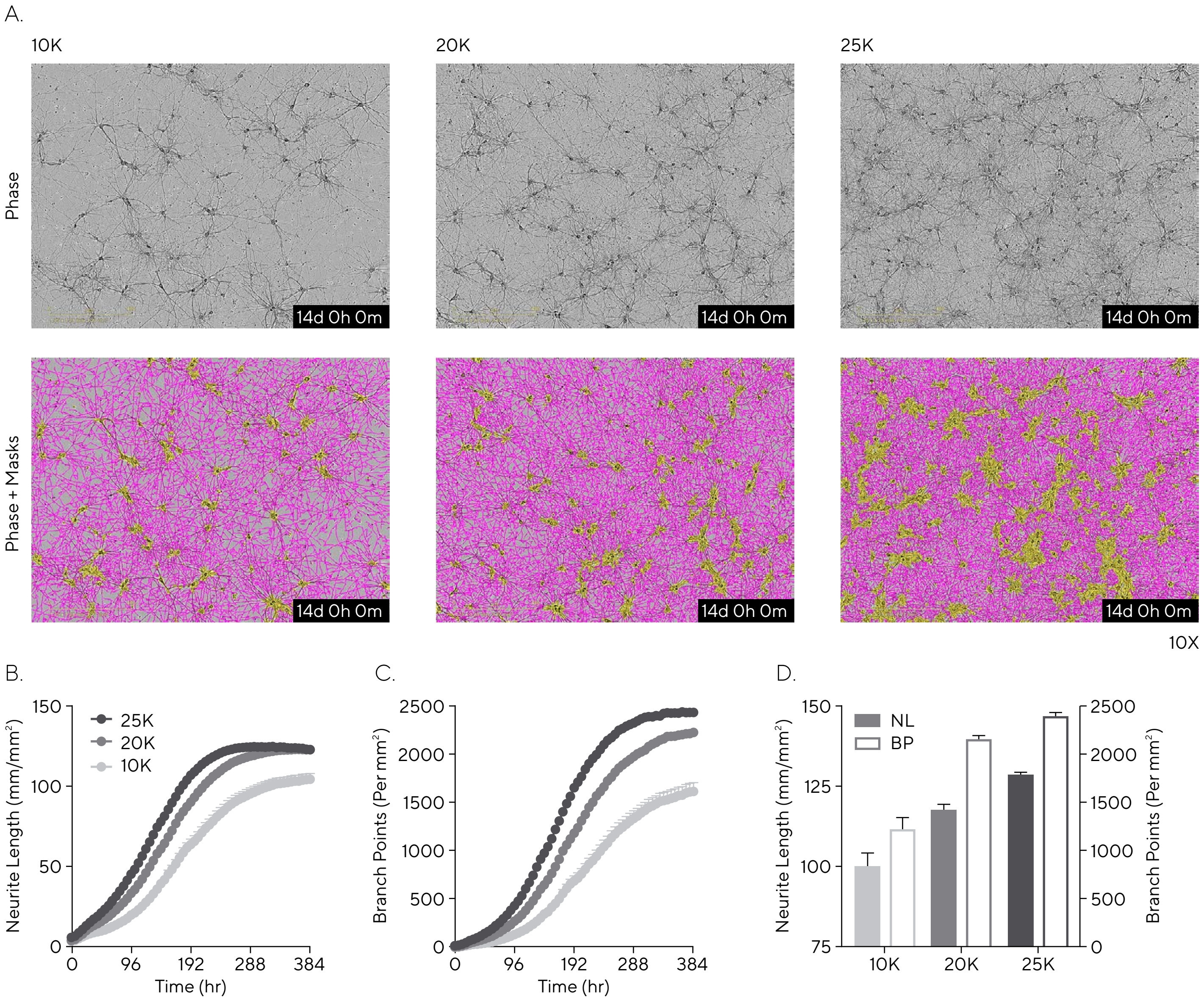

Figure 3

Label-Free Quantification of Neurite Outgrowth in Neuronal Mono-cultures

Rat primary cortical neurons were seeded into poly-D-lysine (PDL)-coated 96-well plates at a range of cell densities (10–25K cells/well). High-definition phase contrast images were acquired using the Incucyte® Live-Cell Analysis System over 16 days and automatically quantified using integrated Incucyte® Neurotrack Analysis Software. Representative images shown for phase and segmentation masks (cell body cluster in orange, neurites in pink) for each seeding density at Day 14 (A). Kinetic quantification reveals density-dependent differences in neurite length (B) and branch points (C), which both increase with an increase in seeding density (D). Data shown as mean ± SEM, n = 24 replicates.

Quantifying Neuronal Outgrowth in Co-cultures

Incucyte® Neurolight Lentivirus is a lentiviral reagent designed to transduce multiple neuronal cell types specifically and efficiently with low toxicity. Cell-handling protocols and assay conditions were optimized to produce a robust 96-well plate format capable of supporting medium throughput screening activities and mechanistic studies.

When developing an *in vitro* assay using a fluorescent protein, it is important to show that the expressed label does not affect the global biology of the system. We examined the effects of the Incucyte® Neurolight Lentivirus on neurite dynamics in rat primary neurons and astrocytes using an antibody against βIII-tubulin to assess total neurite length in cultures exposed to varying Incucyte® Neurolight Red Lentivirus MOIs. Quantification of βIII-tubulin antibody-stained fluorescent images using Incucyte® Neurotrack Analysis Software provides an independent measure of neurite length and can expose possible adverse effects of the reagent (Figure 4). The MOI graph represents the neurite length calculated at 7 days post-infection following exposure to control solution (no Incucyte® Neurolight Red Lentivirus). Incucyte® Neurolight Red Lentivirus produced no significant changes in total neurite length up to MOI 3.3 (pink circles) indicating that Neurolight infection does not significantly alter neurite length (Figure 4A).

Figure 4 displays a 96-well microplate view measuring neurite length over 12 days post-infection. Examination of the assay time course shows consistent responses across all wells. Low intra-plate variation was observed with a standard deviation of less than 9.2 mm/mm² at each time point (Figure 4B). The coefficient of variation (%) measured in individual experiments at 12 days post-infection ranged from 1.4% –12.6% with an overall mean value of 4.4%. Further, inter-plate variation in maximum neurite length was assessed for control wells from 13 plates run over a 5-month period. The cross-plate variability of all experiments was within 20% of the overall mean neurite length (Figure 4C). Heat maps of individual experiments revealed no significant position effects (data not shown). The Incucyte® Neurotrack co-culture assay provides a robust, medium throughput measurement of neurite dynamics over a minimum of a 12-day period.

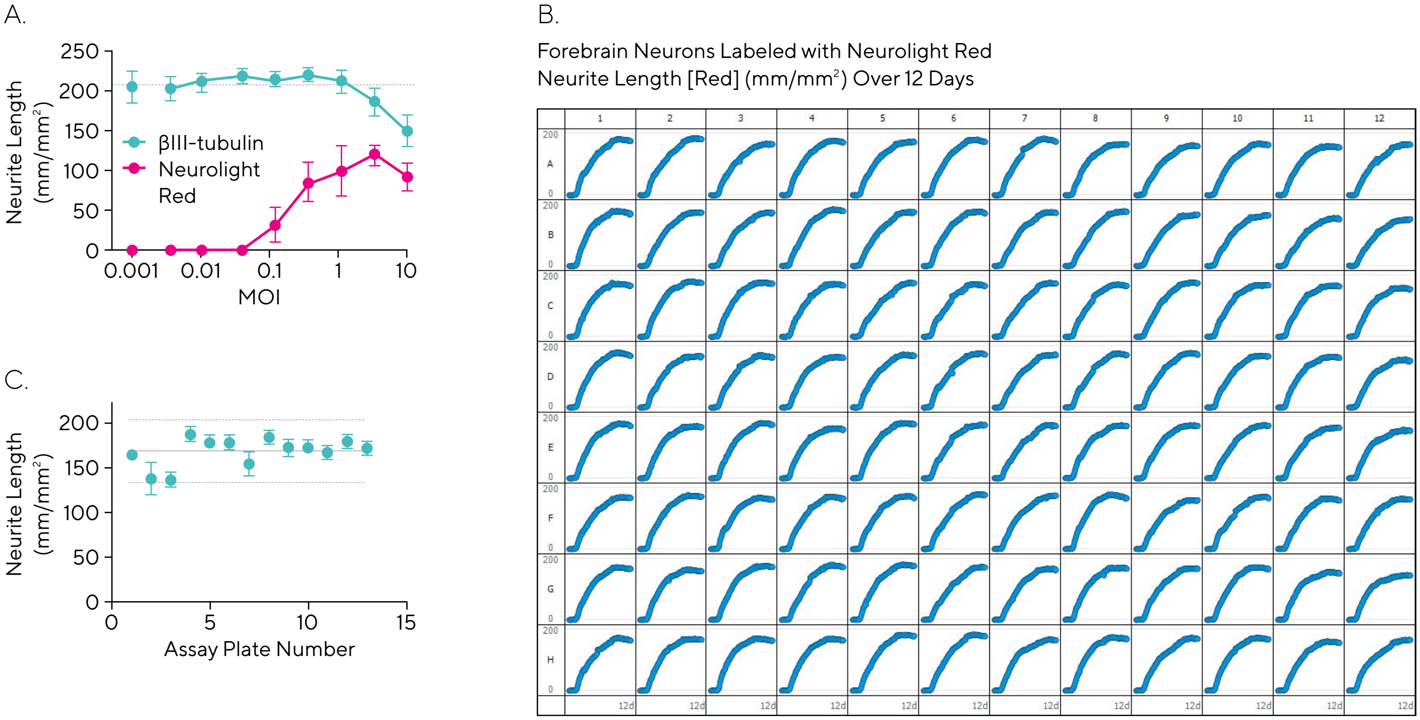

Forebrain Neurons Labeled with Neurolight Red
Neurite Length [Red] (mm/mm²) Over 12 Days

Figure 4

Validation of Incucyte® Neurolight Lentivirus Infection

Fluorescent images of βIII-tubulin-stained (teal) or Incucyte® Neurolight Red (pink) infected rat forebrain neurons were quantified using the Incucyte® Neurotrack Analysis Software Module. Neurite length values (mm/mm², mean ± SD, n = 4) were obtained and MOIs (0.001–10) compared from the same wells at 7 days following infection (A). The 96-well plate view displays neurite lengths over 12-day assay and data combined in time course (mean ± SD) to understand intra-assay variability (B).Neurite length was calculated in untreated control wells at 12 days post infection (mean ± SD, n = 8) for 13 separate plates run over 5 months to obtain inter-assay variability. Solid line represents overall mean neurite length (167.0 ± 16.0 mm/mm²) and dashed lines represent the ± 20% limits from the overall mean (C).

Importance of Astroglia in iPSC Differentiation

It is widely accepted that the nervous system presents a coordinated involvement of neurons and glia. Glial cells are active partners to neurons in brain development and activity via bidirectional communication. This is orchestrated at the tripartite synapse, which is composed of the neuronal pre- and post-synapses and their close interaction with the surrounding astroglia.

To investigate the effect of astrocytes in neurite development, a humanized live-cell model of neuronal activity was developed in collaboration with Talisman Therapeutics. Recent advances in hiPSCs offer a powerful *in vitro* model strategy for the study of both healthy and disease stages of the human nervous system. Non-perturbing neurite outgrowth measurements performed in mono-cultures or co-cultures via automatic segmentation of time-lapse imaging using the Incucyte® Neurotrack Analysis Software Module were performed and are shown in Figure 5. When co-cultured with astrocytes, neurons developed a greater number of neurites with increased branching compared to mono-cultures, demonstrating the importance of astroglia in iPSC differentiation.

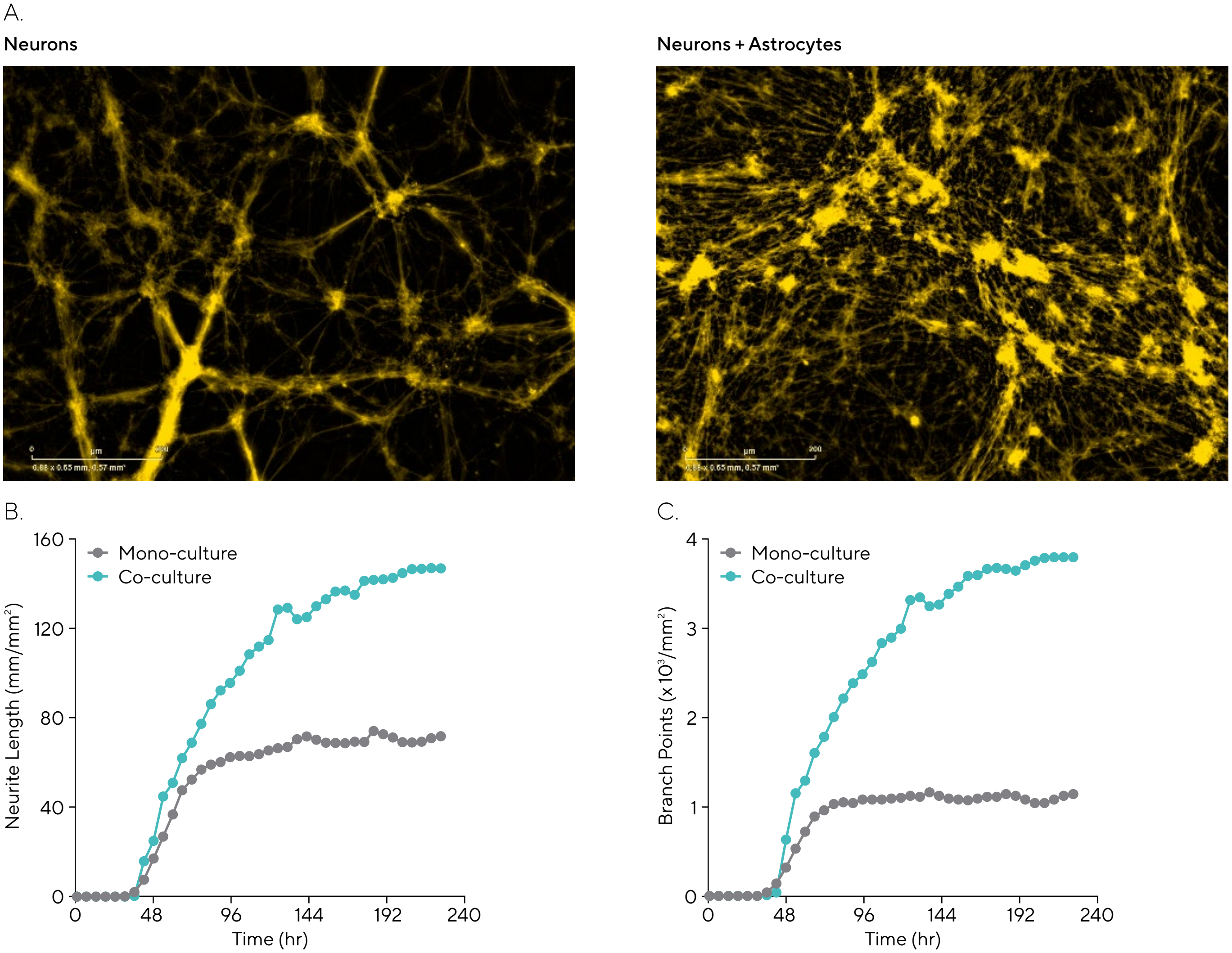

Neurons

Neurons + Astrocytes

Figure 5

iPSC-Derived Neurons Co-cultured with Astrocytes Show Increased Neurite Outgrowth

iPSC-derived neurons developed by Talisman Therapeutics were infected with Incucyte® Neurolight Orange Lentivirus, co-cultured with mature astrocytes and monitored and quantified using the Incucyte® Live-Cell Analysis System. Representative fluorescence images shown for both mono-cultures and co-cultures (A). Time-course plots revealed that neurons in co-cultures yield greater neurite outgrowth (B, neurite length) and branching (C, branch points) when compared to neurons cultured in isolation (mean ± SEM).

Quantitative Pharmacology in a Parkinson’s Disease Model

Neurodegenerative diseases, such as Parkinson’s disease (PD), are chronic and debilitating disorders that progressively cause degeneration and/or death of neuronal cells. Neurite length can be a sensitive marker of neurodegenerative disease and neurotoxicity. To develop a model of Parkinson’s disease, we created a co-culture system of rat primary striatal neurons and astrocytes (Figure 6). Following a period of neurite development (10 days), the dopaminergic-specific neurotoxin 6-hydroxydopamine (6-OHDA) was applied to induce disease-relevant neuronal damage. A time- and concentration-dependent effect on neurite disruption was observed, yielding an IC_{50} value for 6-OHDA of 70.5 µM for neurite length. 6-OHDA at the maximum concentration tested (500 µM) caused 95% of neurites to be abolished. This model system may provide a quantitative phenotypic assay for agents designed to reverse or minimize the neurotoxic effect of 6-OHDA and aid in the development of improved therapeutics for Parkinson’s disease.

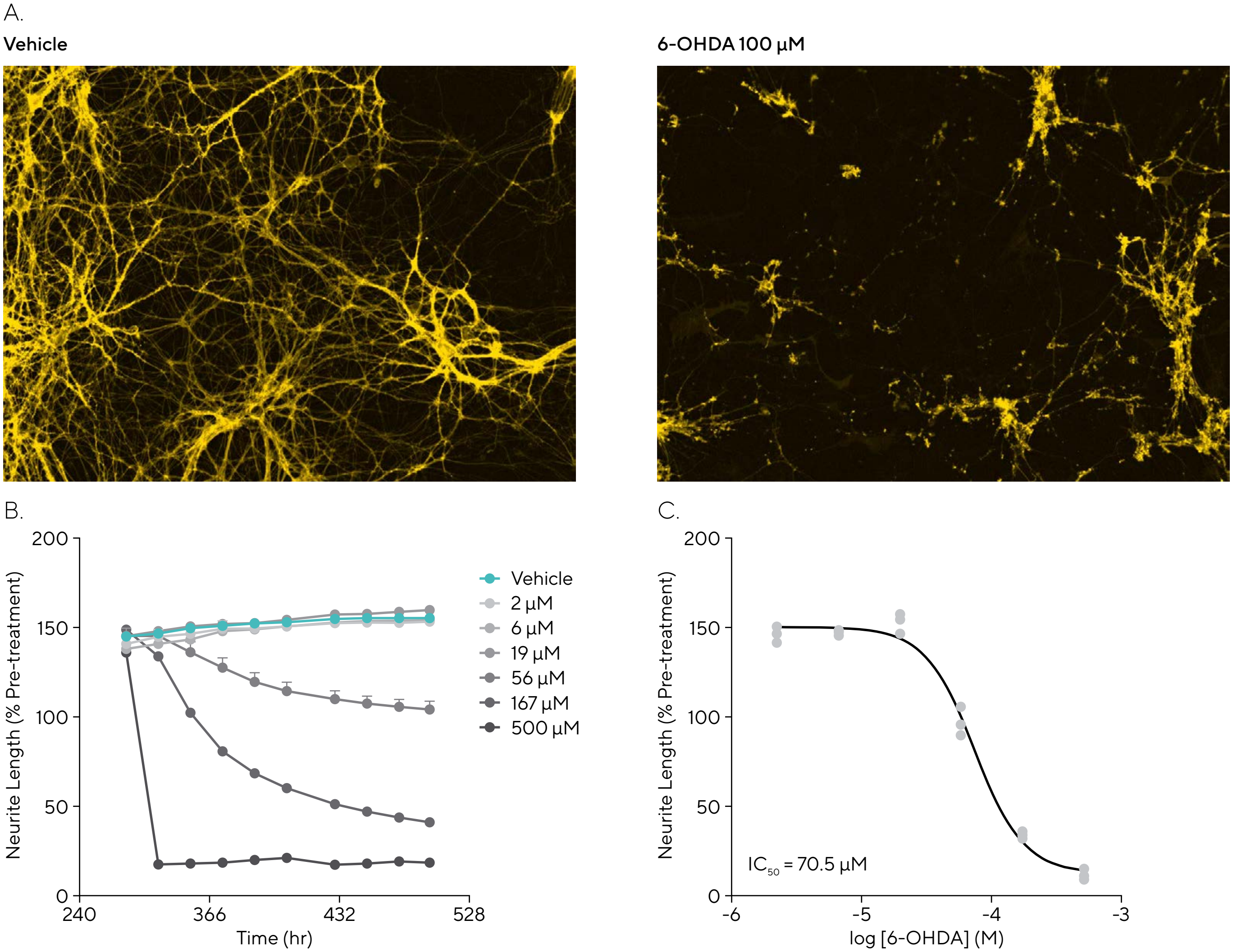

Figure 6

6-OHDA-Induced Neurite Disruption in a Parkinson’s Disease Model

Rat primary cortical neurons were labeled with Incucyte® Neurolight Lentivirus and co-cultured with astrocytes. 10 days post-seeding, once the neurite network had stabilized, co-cultures were treated with varying concentrations of 6-OHDA and monitored for 12 days (A). Representative fluorescence images are shown for vehicle and 100 µM 6-OHDA (10 days). (B) Time-course graphs represent the change in neuronal length normalized to pre-treatment value at the different drug concentrations (%, mean ± SEM, 3 replicates). (C) Concentration response curve derived from temporal profiles shows individual neurite length values at 12 days post-treatment.

Conclusions

The Incucyte® Live-Cell Analysis System, combined with Incucyte® Neurotrack Analysis Software Module and when necessary, the Incucyte® Neurolight Lentivirus, provides a robust method to image neurons in mono-cultures and co-cultures and quantify changes in neurite length of living cultures from days to weeks. The image analysis software is flexible for quantification of many cell types, from immortalized cell lines to primary neurons and iPSCs. An intuitive user interface allows rapid assay optimization and automated quantification of neurite dynamics. All data and time points can be verified by inspecting individual images and/or time-lapse movies. Observation of cell morphology provides additional validation and insight into the biological effect of treatment groups. This approach provides a sensitive method to detect pharmacological manipulations that alter neurite dynamics, including processes such as elongation and retraction.

North America
Sartorius Corporation
300 West Morgan Road
Ann Arbor, Michigan 48108
USA
Phone +1 734 769 1600

Europe
Sartorius UK Ltd.
Longmead Business Centre
Blenheim Road
Epsom
Surrey, KT19 9QQ
United Kingdom
Phone +44 1763 227400
Email:

Asia Pacific
Sartorius Singapore Pte. Ltd.
30 Pasir Panjang Road,
#06-32, Mapletree Business City
Singapore 117440
Phone +65 6872 3966

Received: 25 March 2021 | Revised: 9 November 2021 | Accepted: 12 November 2021

DOI: 10.1002/glia.24122

GLIA

WILEY

RESEARCH ARTICLE

Dysfunction of cerebellar microglia in Ataxia-telangiectasia

Hadar Levi[1] | **Ela Bar**[1] | **Stav Cohen-Adiv**[1] | **Suzan Sweitat**[1] | **Sivan Kanner**[1] | **Ronit Galron**[1] | **Yulia Mitiagin**[1] | **Ari Barzilai**[1,2]

[1]Department of Neurobiology, George S. Wise, Faculty of Life Sciences, Tel Aviv University, Tel Aviv, Israel

[2]Sagol School of Neuroscience, Tel Aviv University, Tel Aviv, Israel

Correspondence

Ari Barzilai, Department of Neurobiology, George S. Wise, Faculty of Life Sciences, Tel Aviv University, Ramat Aviv, Tel Aviv, 69978, Israel.

Email: arib@tauex.tau.ac.il

Funding information

Tel Aviv University Research Authority, Grant/Award Number: 0604912581390000; Joint Italian-Israeli Laboratory on Application of Neuroscience, Grant/Award Number: 590308; German Israeli Foundation, Grant/Award Number: I-192-418.13-2014; Ministry of Science and Technology, Grant/Award Number: 3-14260-2016; Israel Science Foundation, Grant/Award Numbers: 1307/19, 41/15

Abstract

Ataxia-telangiectasia (A-T) is a multisystem autosomal recessive disease caused by mutations in the *ATM* gene and characterized by cerebellar atrophy, progressive ataxia, immunodeficiency, male and female sterility, radiosensitivity, cancer predisposition, growth retardation, insulin-resistant diabetes, and premature aging. ATM phosphorylates more than 1500 target proteins, which are involved in cell cycle control, DNA repair, apoptosis, modulation of chromatin structure, and other cytoplasmic as well as mitochondrial processes. In our quest to better understand the mechanisms by which ATM deficiency causes cerebellar degeneration, we hypothesized that specific vulnerabilities of cerebellar microglia underlie the etiology of A-T. Our hypothesis is based on the recent finding that dysfunction of glial cells affect a variety of process leading to impaired neuronal functionality (Song et al., 2019). Whereas astrocytes and neurons descend from the neural tube, microglia originate from the hematopoietic system, invade the brain at early embryonic stage, and become the innate immune cells of the central nervous system and important participants in development of synaptic plasticity. Here we demonstrate that microglia derived from *Atm*$^{-/-}$ mouse cerebellum display accelerated cell migration and are severely impaired in phagocytosis, secretion of neurotrophic factors, and mitochondrial activity, suggestive of apoptotic processes. Interestingly, no microglial impairment was detected in Atm-deficient cerebral cortex, and Atm deficiency had less impact on astroglia than microglia. Collectively, our findings validate the roles of glial cells in cerebellar attrition in A-T.

KEYWORDS

Ataxia-telangiectasia, A-T, ATM, microglia, astrocytes, brain degenerative diseases

1 | INTRODUCTION

Ataxia-telangiectasia (A-T; OMIN#208900) is a highly pleiotropic autosomal recessive human disorder (Lavin, 2008; Perlman et al., 2012; Rothblum-Oviatt et al., 2016; Shiloh & Lederman, 2017) caused by null mutations in the *ATM* gene, which encodes the ATM protein kinase (Savitsky, Bar-Shira, et al., 1995; Savitsky, Sfez, et al., 1995; Shiloh & Ziv, 2013; Ziv et al., 1997). Patients experience progressive cerebellar ataxia that develops into severe motor dysfunction. The cerebellar cortical degeneration primarily involves Purkinje neurons and granule neurons. Peripheral neuropathy may develop during the second decade of life. Oculocutaneous telangiectasia (dilated small blood vessels) appear variably. Marked immunodeficiency is typically manifested by reduction of IgG4, IgA, IgG2, and IgE isotypes and diminished B and T lymphocyte counts. Lung infections often result from food aspiration emanating from neuromotor dysfunction combined with the immunodeficiency. Another hallmark is gonadal and thymic dysgenesis. Cancer predisposition is manifested

---

Hadar Levi and Ela Bar contributed equally to this work.

as increased tendency to develop lymphoreticular malignancies, and various carcinomas appear in older patients. Growth retardation and occasional endocrine abnormalities are also seen, particularly insulin-resistant diabetes. Premature aging has recently been recognized in A-T (Shiloh & Lederman, 2017). Major laboratory findings are elevated serum levels of α-fetoprotein and carcinoembryonic antigen.

A-T patients show striking sensitivity to the cytotoxic effect of ionizing radiation, and A-T cells exhibit marked chromosomal instability, sensitivity to radiation and radiomimetic chemicals, and reduced telomere length (Metcalfe et al., 1996; Pandita, 2002; Shiloh et al., 1983; Taylor et al., 1975; Ziv et al., 1989). Ionizing radiation sensitivity results from a profound defect in the cellular response to DNA double-strand breaks (DSBs) due to the lack of the ATM protein kinase, which mobilizes the DSB response (Bhatti et al., 2011; McKinnon, 2012; Shiloh & Ziv, 2013). Many A-T symptoms can be attributed to the abrogation of the cellular response to DSBs, whether physiological or induced by endogenous reactive oxygen species (ROS) (McKinnon, 2012). However, the mechanism behind the most devastating symptom of A-T—the progressive cerebellar atrophy—is still being debated (Biton et al., 2008; Ditch & Paull, 2012; Herrup, 2013; Herrup et al., 2013; Hoche et al., 2012; McKinnon, 2012; Shiloh, 2014; Shiloh & Ziv, 2013; Vail et al., 2016; Y. Yang et al., 2014). Although patients with the classical form of A-T have null mutations in both copies of the *ATM* gene (Savitsky, Bar-Shira, et al., 1995; Savitsky, Sfez, et al., 1995; Ziv et al., 1997), *ATM* mutations that cause milder forms of the disease have been identified (Gilad et al., 1996; Gilad et al., 1998) (Alterman et al., 2007; Claes et al., 2013; Meneret et al., 2014; Nakamura et al., 2014; Saunders-Pullman et al., 2012; Silvestri et al., 2010; Soresina et al., 2008; Taylor et al., 2014; Verhagen et al., 2009; Verhagen et al., 2012; Worth et al., 2013).

DNA damage—a major threat to genome stability—is caused in living organisms primarily by endogenous ROS or radicals produced during metabolism, which induce tens of thousands of DNA lesions per cell per day (Cadet & Wagner, 2013; Crouch & Brosh Jr., 2016; Jena, 2012; Jeppesen et al., 2011; Lindahl, 1993). Defense against threats to genome integrity is critical for cellular homeostasis and timely development and for prevention of undue cell death, cancer, and premature aging (Abbas et al., 2013; Ciccia & Elledge, 2010; Jeppesen et al., 2011; McKinnon, 2013; Negrini et al., 2010; Thompson, 2012; Vijg & Suh, 2013). The DNA damage response is a vast signaling network that activates DNA repair mechanisms and rapidly modulates many physiological processes, leading to numerous protein post-translational modifications and marked modulation of the transcriptome (Goodarzi & Jeggo, 2013; Panier & Durocher, 2013; Polo & Jackson, 2011; Shiloh & Ziv, 2013; Sirbu & Cortez, 2013; Thompson, 2012). The importance of the DNA damage response to human health is highlighted by mutations that lead to genome instability syndromes, one of which is A-T (Aguilera & Garcia-Muse, 2013; Ciccia & Elledge, 2010; Jeppesen et al., 2011; McKinnon, 2013; O'Driscoll, 2012; Perlman et al., 2012; Vijg & Suh, 2013).

The DNA damage response is more vigorously activated by DSBs than other DNA lesions (Bhatti et al., 2011; Ciccia & Elledge, 2010; Marechal & Zou, 2013; Shiloh & Ziv, 2013; Sirbu & Cortez, 2013; Stracker et al., 2013; Thompson, 2012). DSBs are induced by DNA damaging agents or endogenous ROS (Schieber & Chandel, 2014) or are formed during physiological processes such as meiotic recombination (Borde & de Massy, 2013; Lange et al., 2011) and the rearrangement of antigen receptor genes in the adaptive immune system (Alt et al., 2013). The primary transducer of the DSB response network is ATM (Bhatti et al., 2011; McKinnon, 2012; Shiloh & Ziv, 2013); the protein kinase activity of ATM is markedly enhanced in response to DSBs (Bakkenist & Kastan, 2003; Bensimon et al., 2010; Bhatti et al., 2011; Kaidi & Jackson, 2013; Kozlov et al., 2006; Paull, 2015; Shiloh & Ziv, 2013; Sun et al., 2007). Activated ATM phosphorylates numerous proteins in various pathways of the DSB response (Bensimon et al., 2010; Bensimon et al., 2011; Matsuoka et al., 2007; Mu et al., 2007; Shiloh & Ziv, 2013). ATM belongs to a family of PI-3 kinase-like protein kinases (Lovejoy & Cortez, 2009) that includes, among other proteins, the catalytic subunit of the DNA-dependent protein kinase (B. P. Chen et al., 2012; Kong et al., 2011) and ATR (Errico & Costanzo, 2012; Marechal & Zou, 2013). Like ATM, the DNA-dependent protein kinase is involved in the response to genotoxic and other stresses. ATM might also be involved in regulating other aspects of genome integrity such as nucleotide metabolism, the response to replication stress, and resolution of the occasional conflicts between DNA damage and the transcription machinery. Further, ATM is active in metabolic pathways (Ambrose & Gatti, 2013; Ditch & Paull, 2012; Eaton et al., 2007; Herrup, 2013; D. Q. Yang et al., 2011) that maintain cellular redox balance (Cremona & Behrens, 2014; Ditch & Paull, 2012; Semlitsch et al., 2011; D. Q. Yang et al., 2011) and mitochondrial metabolism (Ambrose & Gatti, 2013; Eaton et al., 2007; Sharma et al., 2014; Stern et al., 2002; Valentin-Vega et al., 2012; Valentin-Vega & Kastan, 2012). Different functions of ATM involve different modes of ATM activation (Ditch & Paull, 2012; Guo et al., 2010; Paull, 2015). Thus, evidence is emerging that ATM's capacity as a protein kinase is exploited in signaling pathways that are not associated with DNA damage including pathways that operate in the cytoplasm (Ambrose & Gatti, 2013; Ditch & Paull, 2012; Eaton et al., 2007; Herrup, 2013; Herrup et al., 2013; Vail et al., 2016; D. Q. Yang et al., 2011; Y. Yang et al., 2014). Thus, when functional ATM is missing, as it is in A-T patients, the modulation of numerous pathways in response to occasional stresses becomes suboptimal and the cumulative DNA damage disrupts genome homeostasis.

Between 5% and 15% of the cells in the central nervous system (CNS) are microglia (Herculano-Houzel, 2014; Ohtaki et al., 2013). These cells are derived from early embryonic myeloid progenitors of the hematopoietic system. It was long thought that microglia were derived from peripheral macrophages that enter the brain after birth. In 2010, a landmark fate mapping study challenged this dogma by showing that microglia develop from myeloid progenitors in the yolk sac (Ginhoux et al., 2010). These cells then make a pilgrimage into the brain very early in embryonic development (Kierdorf et al., 2013; Ransohoff & Cardona, 2010). The realization that microglia develop alongside neurons during this critical period of brain development has led to a change of thinking about microglia in the healthy brain. New data implicate microglia in many functions required to build and wire the developing CNS, ranging from neurogenesis to synaptic pruning.

Microglial cells that colonize the brain (Ginhoux et al., 2010) continually monitor the microenvironment (Nimmerjahn et al., 2005) and are implicated in neuro-plasticity, host defense, homeostasis, cell migration, debris scavenging, peripheral immune cell recruitment, and immune response regulation (Aloisi, 2001). In response to a variety of stressors, microglia are capable of migrating and undergo morphological and functional changes. Pathological stimuli such as cytokines, chemokines, and growth factors, polarize microglial cells and play important roles in either the deterioration or the repair of the CNS. Microglia are active contributors to neuronal damage in brain degenerative diseases, and over-activation or dysregulation of microglia can result in disastrous and progressive neurotoxic consequences. Although these observations have been widely reviewed in recent years (Kim & Joh, 2006; McGeer et al., 2006; Zecca et al., 2006), the characteristics defining deleterious microglial activation and the mechanisms that result in neurotoxic microglial activation remain poorly understood.

Microglia are also crucial part to maintenance of brain homeostasis (Napoli & Neumann, 2009). They release a number of neurotrophic factors and structurally remove synapses from damaged neurons (Cullheim & Thams, 2007; Trapp et al., 2007). Microglia also function in neurogenesis, enabling the integration of new neurons into neuronal circuits in adult animals (Wake et al., 2013), and BDNF secreted by microglia modulates neuronal plasticity in a mouse model of neuropathic pain (Coull et al., 2005). Neuronal plasticity is important for learning, memory, and cognition (Morris et al., 2013). Programmed cell death is integral to CNS development (de la Rosa & de Pablo, 2000). For example, most of cerebellar Purkinje cells that undergoing developmental apoptosis are engulfed by amoeboid microglia that release superoxide ions to trigger cell death (Marin-Teva et al., 2004). Abnormalities in cerebellar development, including alterations in neuronal numbers and neural circuit formation, can lead to sensory motor coordination deficits and cerebellar ataxia (Manto & Jissendi, 2012). This suggests that microglia have a role in the loss of cerebellar Purkinje cells in A-T. Following injury or disease, microglia are rapidly recruited to sites of damage where they engulf, or phagocytose, debris and unwanted and dying cells. Although critical for the immune response to infection or trauma, microglia also contribute to pathological neuroinflammation by releasing cytokines and neurotoxic proteins (Perry et al., 2010; Ransohoff & Cardona, 2010).

It has been estimated that the total number of microglia in adult mouse brain is around 3.5×10^6, but these cells are not evenly distributed throughout the brain. Compared to cerebral cortex, the cerebellum is much less densely populated with microglia. The gray matter of the cerebellar deep nuclei contains most of the microglial cells, whereas much lower density was found in the granular and the molecular layers (Lawson et al., 1990). FACS analysis based on immunoregulatory markers revealed distinct regional and immunological diversity (de Haas et al., 2008). Genome-wide analysis of microglial cells derived from different brain regions revealed that these cells display region-specific transcriptional identities. Interestingly, the cerebellum has high expression of genes related to immune as well as defense responses. Lower density of cerebellar microglia implies that each cells has to survey a larger volume of tissue with increased energy demands on each glial cell (Grabert et al., 2016). Deep single–cell RNA sequencing shows higher microglia heterogeneity in early postnatal as compared to adult microglia, which display less regional diversity. A subset of a proliferative-region-associated microglia are detected in developing white matter. These cells have an amoeboid morphology similar to that of disease-associated microglia. These microglial cells are metabolically active and capable of phagocytosis of newly formed oligodendrocytes (Q. Li et al., 2019). During early development, the amoeboid microglial cells invade the white matter, but during development these cells are replaced by ramified microglia that colonize the gray matter (Ling & Tan, 1974; Stensaas & Reichert, 1971). Grabert et al. further suggested that the transcriptome of the microglia undergoes an aging process that is non-uniform across brain regions. The cerebellar microglia age faster than those in the forebrain regions (Grabert et al., 2016).

Similar to neurons and microglia, astrocytes also display functional and regional heterogeneity. Hoft et al. showed that astrocytes have physiological differences within the same brain region (Hoft et al., 2014). Five different astrocytic populations were found in several different brain regions. Interestingly, each astrocytic population displayed different regulation of synaptogenesis (John Lin et al., 2017). Astrocytes are closely interconnected with various types of neuronal populations. In response to insults, astrocytes can secrete either pro- or anti-inflammatory signals. They react to neuronal insults by becoming reactive, hypertrophic, and senescent or by increased proliferation (Miller, 2018). Under certain pathological conditions the astrocyte become reactive and heterogeneous (Liddelow & Barres, 2017). Thus, reactive astrocytes cannot be divided into simple binary phenotypes such as neuroprotective or neurotoxic. Escartin et al. suggested that reactive astrocytes could adopt multiple states depending on context (Escartin et al., 2021).

Co-culturing of cerebral cortical astrocytes with cerebellar astrocytes led to the demise of the astrocytes and also demonstrated the heterogenic functionality of astrocytes; however, cerebellar astrocytes fully support the viability and the functionality of age-matched granule neurons (Kanner et al., 2018). Astrocytes and microglia seem to be interconnected. Activated microglia can induce A1 astrocytes by the release of IL-1a, TNF, and C1q and thereby become toxic (Liddelow et al., 2017). Together, these findings and others support the notion that both microglia and astrocytes are highly interconnected as well as heterogenic.

Important tools in the investigation of the physiological and molecular bases of A-T syndrome are mouse models obtained using gene targeting or transgene expression. Atm-deficient mice exhibit many of the characteristics of human A-T (Barlow et al., 1996; Elson et al., 1996; Hande et al., 2001; Y. Xu et al., 1996) as well cerebellar abnormalities as shown in our recent publication (Kanner et al., 2018). Here we show that Atm deficiency in mice severely affects the functionality of the cerebellar but not cerebral cortical microglial cells. Atm-deficient cerebellar microglia display impaired secretion of vital neurotrophic factors, accelerated migration, and deterioration of mitochondrial functionality. On the other hand, no microglial impairment was detected in Atm-deficient cerebral cortex. Further, Atm deficiency had less impact on astroglia than microglia. These findings validate the roles of glial cells in cerebellar attrition in A-T.

2 | MATERIALS AND METHODS

2.1 | Atm-deficient mice and animal care

Atm$^{+/-}$ mice were a generous gift from Dr. Anthony Wynshaw-Boris (University of California, San Diego, CA, USA). The construction of the Atm-deficient mice (allele designation Atmins 5790neo) was previously described (Barlow et al., 1996). Mice from heterozygous crosses were genotyped by PCR (Barlow et al., 1996). Heterozygotes were derived from mating in a completely inbred 129SvEv background. Experiments were performed using young (4 day old) *Atm*$^{-/-}$ mice or wild type (WT) littermates as controls. All animal care protocols and all experimental protocols used for this study were conducted according to the animal research guidelines from Tel Aviv University and were approved by the Tel Aviv University Animal Care Committee.

2.2 | Cerebellar and cerebral cortical cultures enriched in microglia

Mixed glial cultures were prepared from cerebella and cerebral cortices of 4-day-old WT and *Atm*$^{-/-}$ SvEv129 mice and grown in MEM-EAGLE (Beit Haemek) with essential amino acids, 0.6 mg/ml glucose, 10% FCS (heat inactivated), 0.2% L-glutamine, 0.8% GlutMAX (100X) (Gibco), 0.5% penicillin (100 U/ml), and streptomycin (100 μg/ml). After 12 days in culture, microglia isolation was performed as previously described (Giulian & Baker, 1986). Briefly, after mechanical dissociation, microglia cerebellar cells were collected and centrifuged. The cells were then resuspended in cold PBS with 1% FCS, labeled with CD11b-PE, and subjected to FACS isolation to assess microglial purity.

2.3 | Cerebellar and cerebral cortical cultures enriched in astrocytes

Mixed glial cultures were prepared from cerebella and cerebral cortical of 4-day-old *Atm*$^{-/-}$ and WT SV129 mice. After16 days in culture, glial cultures reached confluency, and more than 90% of cells were astrocytes. Isolation was performed using pre-warmed trypsin incubation for 5 min, followed by a short aggressive shaking by hand. Trypsin and floating astrocytes were transferred to a tube containing DMEM, which was centrifuged for 5 min at 2300 rpm [Eppendorf 5242R, rotor FA-45-24-11 (541*g*)]. The numbers of live and dead cells, identified based on dye exclusion or uptake, were counted. The yield of astrocytes was a density of approximately 4,500,000 cells/ml. The cells were then cultured using technics that depended on the experiment or were reseeded. Each culture was prepared from a single mouse.

2.4 | Immunocytochemical analyses

Following isolation, microglial cells were grown on poly-L-lysine-coated 13-mm glass coverslips in 24-well plates at 37°C for 2–3 days prior to fixation. Cultures were washed twice with PBS, then fixed with 4% paraformaldehyde (Merck) for 10 min and left in PBS until staining. For immunocytochemical staining, fixed cultures were washed three times with PBS (10 min each). Next, cells were permeabilized with 0.5% Triton x100 (Sigma) in PBS for 10 min. Cultures were blocked with 2% BSA, 10% normal donkey serum, and 0.5% Triton x100 in PBS for 1 h at room temperature. The cultures were incubated overnight with the primary antibodies GFAP (1:400, Sigma-Aldrich, cat# G9269) and Iba-1 (1:500, Synaptic Systems cat# 234-004) at 4°C. Cultures were then washed three times with PBS and incubated with the secondary antibodies for GFAP (Alexa Fluor® 546 Goat Anti-Rabbit), for Iba-1 (Alexa Fluor® 488 Goat Anti-Guinea pig) for 1 h at room temperature. After washing three times with PBS, cells were incubated with DAPI (1:1000, Jackson) in PBS for 15 min and then washed again with PBS. The coverslips containing the stained cells were mounted on microscope slides using Fluoroshield (Sigma-Aldrich cat# F6182). Slides were visualized in a Leica TCS SP8 confocal laser-scanning platform. Analyses of cerebellar activated microglia was carried out using an F4/80 antibody that specifically labels activated microglia (1:400, Abcam, cat #6640) and an appropriate secondary antibody (Alexa Fluor® 546 Goat Anti-Rat). Analyses of proliferation was carried out using a Ki67 antibody (1:200, BioVision, cat #A1135-100; secondary antibody Alexa Fluor® 546 Goat Anti-Rabbit).

2.5 | Immunocytochemical analyses of cerebellar sections

WT and *Atm*$^{-/-}$ mice at 1.5 months of age were perfused with PBS. Whole brains were removed and placed in 4% PFA overnight, then rinsed with PBS and submerged in 30% sucrose solution overnight and followed by microtome coronal sectioning to 40-μm thick slices. Sections were kept at −20°C in cryo-protectant. For immunohistochemical staining, the slides were washed three times in PBS, then permeabilized with 0.3% Triton x100 (Merk) in PBS for 1 h and then blocked (10% INGS, 0.25% Triton x100 in PBS) for 1 h at room temperature. Slices were then incubated overnight with primary antibodies (F4/80, Iba-1) at 4°C, washed three times with PBS, and incubated with matching secondary antibody (1:400, Alexa Invitrogen) in a fresh blocking solution for 1 h at room temperature.

Thereafter, the slices were washed three times with PBS, for total of 30 min. Slices were mounted on slides with ProLong Gold antifade reagent (Molecular Probes) and DAPI. Slides were visualized in a Leica SP5 Confocal Laser Scanning Platform. Z-stack images were acquired at 1-μm intervals. Maximum intensity projections were then generated from the Z-stacks, and analysis was performed with image J software.

2.6 | EDU staining

Following isolation, 2×10^5 cells/well were seeded on poly-L-lysine coated 13-mm glass coverslips in a 24-well plate at 37°C overnight prior to fixation. 5-Ethynyl-2′-deoxyuridine (EdU) was added at final concentration of 10 μM for 24 h, then cells were washed twice with PBS for 10 min. Cells were then fixed with 4% paraformaldehyde (Merck) for 10 min and washed twice with PBS. Next, cells were permeabilized with 0.5% Triton x100 (Sigma) in PBS for 10 min. Blocking was performed in 5% BSA, and 0.5% Triton x100 in PBS for 1 h at room temperature. Cells were incubated overnight with primary antibodies (Iba-1, 1:500, Wako) at 4°C. Cells were then washed with PBS three times for 10 min and incubated with secondary antibodies (Alexa) for 1 h at room temperature on an orbital shaker covered in aluminum foil. After washing three times with PBS, cells were incubated with DAPI (1:500, Jackson Laboratories) in PBS for 10 min and then washed again three times with PBS. Coverslips containing the stained cells were mounted on microscope slides using Fluoroshield. Slides were visualized in Leica SP8 microscope.

2.7 | Western blot analyses

Western blots were performed on extracts from both primary microglial cells cultures and 4-month-old WT and *Atm*$^{-/-}$ mice cerebellar tissues as previously described (4). In brief, lysis buffer was added to tissue or cells in a homogenizer tube or well, incubated for 40 min on ice, transferred to 1.5-ml tubes, and centrifuged for 20 min at 10,000*g* at 4°C. The supernatants were transferred to new 1.5-ml tubes and stored at −70°C. Protein concentrations were determined using Bradford reagent (Bio-Rad Laboratories), and 10 μg total protein from each sample were loaded in each well. For electrophoretic separations, 10% polyacrylamide gels were used. Samples were transferred to nitrocellulose membranes. The membranes were blocked with 5% bovine serum albumin blocking buffer for 1 h, washed with 0.05% Tween in TBS, (TBST), and reacted with mouse anti-GAPDH (1:5000, Synaptic Systems, Cat# 106001), mouse anti-actin (1:5000, Thermo Scientific, Cat# MA1-045), rat anti-CD11b (1:50, Abcam, Cat# 8878), anti-BDNF (1:1000, Abcam, Cat# 10319), and rabbit anti-Akt (1:1000, Cell Signaling, Cat# 4691) overnight at 4°C. The membranes were washed three times with TBST and reacted with secondary goat-anti-mouse-HRP (1:10,000, Jackson Laboratories) for 1 h at room temperature. The membranes were washed with TBST, reacted with ECL western blot substrate, and analyzed using the Amersham imager 600UV (GE Life Technologies). Coomassie blue and Ponceau red staining were used as loading controls.

2.8 | Automatic migration assay

To assess the effect of Atm deficiency on microglial migration, microglia were seeded in wells of 96-well, glass-bottomed plates (Sartorius Group) at 3×10^5 cells per well. After incubation at 37°C overnight, a scratch was made using a 96-pin Wound-Maker^{TM} in the middle of each well. Two washes were performed with glial medium (MEM with 10% FBS, 0.6 mg/ml glucose, 2 mM glutamine, 0.8% Gmax, 0.5% penicillin, and 0.5% streptomycin). Time-lapse microscopy was performed with a Sartorius Incucyte® S3 Live-Cell imager with a 10X objective. Images were acquired every 120 min for 48 h. Wound closing was quantified using the Incucyte® software system.

2.9 | Phagocytosis assay

Microglia were suspended in the presence or absence of fluorescent beads (1 μm diameter) for 2 h. Cells were washed thoroughly to remove uninternalized beads and centrifuged. Pellets were resuspended in ice-cold PBS. Cell sorting was performed using the Stratedigm S100EXi flow cytometry instrument. The percentage of cells that had phagocytosed latex beads phagocytosis and fluorescence intensity per cell was calculated using the Flowing software.

2.10 | Mitochondrial activity assay

Mitochondrial activity was evaluated by the 3-(4,5-dimethylthiazol-2-yl)-2,5-diphenyltetrazolium bromide (MTT) reduction assay. In brief, purified primary cultured microglial cells were seeded at 1×10^4 cells/well into 96-well microtiter plates with glial medium. After 24 h, the medium was removed, and the cells were incubated with MTT (0.5 mg/ml) diluted in MEM medium for 1 h at 37°C. The formazan crystals in the cells were solubilized with DMSO. The level of MTT converted to formazan was determined by measuring absorbance at 570 nm relative to absorbance at 630 nm with a Tecan SpectraFluor.

2.11 | Methylene blue cell viability assay

Microglia cell survival was evaluated using methylene blue staining {Yamazaki, 1986 #162}. Microglia were seeded at 1×10^4 cells/well in 96-well microtiter plates with glial medium [MEM-EAGLE (without L-glutamine, with essential amino acid, Biological Industries Beit Haemek, Israel), 0.6 mg/ml Glucose, 10% Fetal calf serum (heat inactivated, Biological Industries Beit Haemek, Israel, 0.8% GlutaMAX, 0.5% Pen/Strep (100 U/ml), 2 mM glutamine]. After 24 h, microglia were fixed with 4% formaldehyde in PBS for 2 h. Cells were washed with 0.1 M boric acid. 1% methylene blue in 0.1% boric acid was placed on cells for 30 min. Cells were washed eight times with doubly distilled water, and the remaining color was eluted from cells using 0.1% HCl. Absorption at 595 nm was measured using a Synergy HTX multi-mode reader (BioTek).

2.12 | Measurement of levels of intracellular ROS

Determination of ROS levels in primary cultures of microglia was performed according to the method reported by Goldshmit et al. (2001). Briefly, 2,7-dichlorodihydrofluorescein diacetate (DCFH-DA, Sigma-Aldrich) was dissolved in DMSO and diluted with MEM lacking phenol red to a final concentration of 10 μM. Cells were plated on poly-ʟ-lysine-coated, 96-well culture plates at a density of 1×10^4 cells/well in glial medium. After 24 h, the medium was replaced with MEM with 10 μM DCFH-DA (without phenol red). After 30 min at 37°C, cells were washed with MEM lacking phenol red. The fluorescence was monitored using a Bio-TEK Instruments FL500 microplate reader with an excitation wavelength of 485 nm and an emission wavelength 530 nm. The increase in fluorescence for each genotype was calculated compared to the control without cells and was normalized to the number of cells as determined by the methylene blue assay.

2.13 | Assessment of mitochondrial mass and membrane potential

For estimation of mitochondrial membrane potential ($\Delta\psi_m$), we used tetramethylrhodamine ethyl ester (TMRE). The assessment of mitochondrial mass/content was performed using MitoTracker Green FM. After microglial isolation, cells were centrifuged to obtain a cell pellet, and the supernatant was removed by aspiration. The cells were suspended in pre-warmed (37°C) staining solution containing the MitoTracker/TMRE probe diluted in glial medium. Cells were incubated for 30 min in the dark. After staining was complete, cells were pelleted by centrifugation and resuspended in fresh pre-warmed PBS for analysis by flow cytometry. The lengths of microglial processes after staining with anti-Iba1 were measured in ImageJ software.

2.14 | Statistical analyses

Following a Shapiro–Wilk normality test, data comparisons were carried out using a two-tailed *t*-test or two-tailed Mann–Whitney *U* test for two groups and one-way analysis of variance (ANOVA) followed by Tukey's multiple comparison test or Kruskal–Wallis test followed by a Dunn's multiple comparison post-hoc test for multiple group comparisons and two-sample Kolmogorov–Smirnov test. All statistical analyses were performed using GraphPad Prism version 6 for Windows or MATLAB. The *p* values of <0.05 were considered statistically significant. Values are expressed as means ± SEM. Statistical details of experiments can be found in the figure legends.

3 | RESULTS

3.1 | Preparation of highly purified microglia and astroglia dissociated cultures

To specifically interrogate the effects of Atm deficiency and microglial origin, we studied their functionality under fully controlled conditions using highly purified dissociated primary cultures of cerebellar and cerebral microglial cells. To obtain highly purified microglial cultures, we adopted the "shaking" method reported previously (Giulian & Baker, 1986; Tamashiro et al., 2012). The purity of microglial cells harvested from mixed glial cultures was evaluated utilizing flow cytometry analysis (FACS) using the microglia/macrophage marker CD11b combined with an Fc receptor blocker. The purity degree of the cerebellar microglia primary cultures was 96.1% for WT and 95.9% for *Atm*$^{-/-}$ cells. Similar results were obtained for cerebral cortical microglial cells: 96.7% for WT and 97.5% for *Atm*$^{-/-}$ cells. The purified microglial cells were cultured and subjected to immunohistochemical analyses using Iba-1, GFAP, and the latter a marker of astrocytes. The major population in culture consists of microglial cells with negligible amounts of astrocytes (Figure 1). Similarly, we found over 90% purity of cerebellar and cerebral cortical astroglial cell cultures (not shown). To verify the specificity of the Iba1 antibody, the cultures were exposed to only the secondary antibody. As shown in Figure S1, no staining was observed demonstrating the specificity of primary anti-Ibs1 antibody.

To explore the differences between cerebellar and cerebral cortical microglia, we compared the amount of microglial cells that can be purified from the mixed glial cultures. Compared to WT cells, the yield of the cerebellar *Atm*$^{-/-}$ microglia was significantly lower, 21.7% that of WT cells (Figure 2a). The yield of the *Atm*$^{-/-}$ microglia derived from cerebral cortex was also significantly lower at 55% of the yield of the WT culture, but markedly higher than that of cerebellar microglia (Figure 2b). Using EdU and Ki67 as markers of cell division, we found no evidence of cell proliferation in cultured cerebellar and cerebral cortical WT and *Atm*$^{-/-}$ microglia. In contrast, both WT and *Atm*$^{-/-}$ astrocytes proliferated demonstrating the specificity of the anti-EdU and Ki67 antibodies (Figure S2a–f). Our results further showed that cerebellar WT and *Atm*$^{-/-}$ were highly sensitive to the presence of EdU, whereas cortical WT and *Atm*$^{-/-}$ were not affected by EdU. No cell division was detected as shown by staining for Ki67, a nuclear protein that serves as a marker of cellular proliferation. Together, these findings suggest that the lower yield of cerebellar and to lesser extent cerebral cortical WT and *Atm*$^{-/-}$ stemmed mainly from cell demise rather than from reduced cell proliferation.

3.2 | Atm deficiency activates cerebellar but not cerebral cortical microglia

Microglial cells change their morphology in response to their activation state from highly ramified non-activated cells to amoeboid or unipolar activated status. In an attempt to validate the notion that Atm

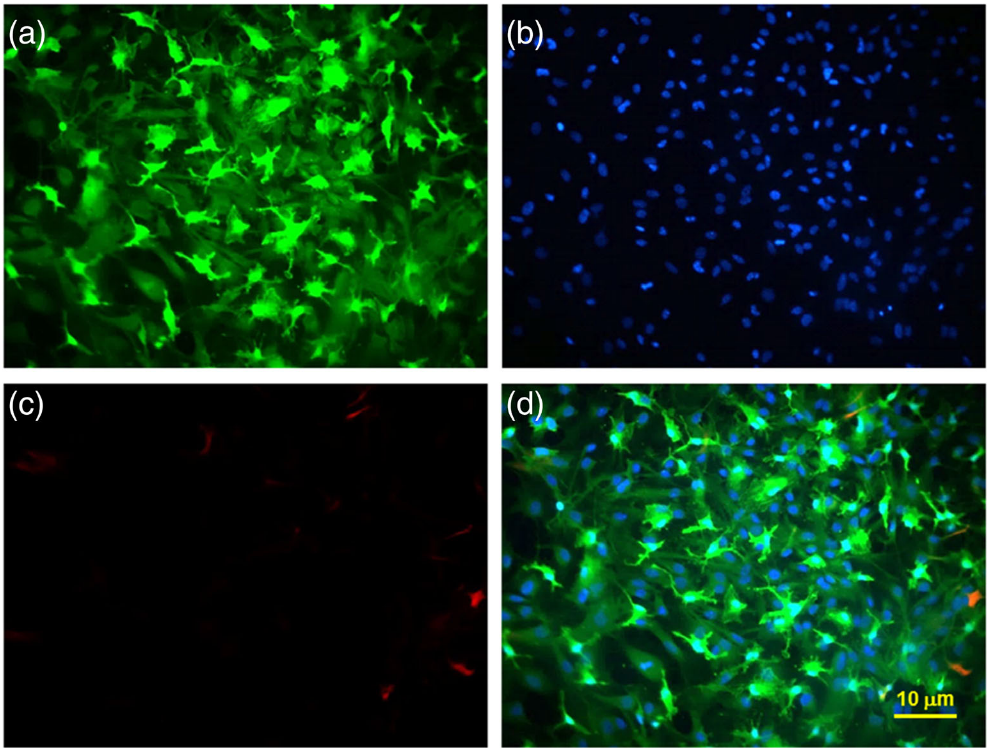

FIGURE 1 Procedure employed results in highly purified microglial cells from WT cerebella. (a) Representative confocal images of cells purified from WT cerebella stained for (a) microglia/macrophage marker Iba-1 (green), (b) cell nuclei with DAPI (blue), and (c) for astrocyte-specific marker GFAP (red). (d) Merged staining showing that most of the cells are microglia with a very low amount of astrocytes

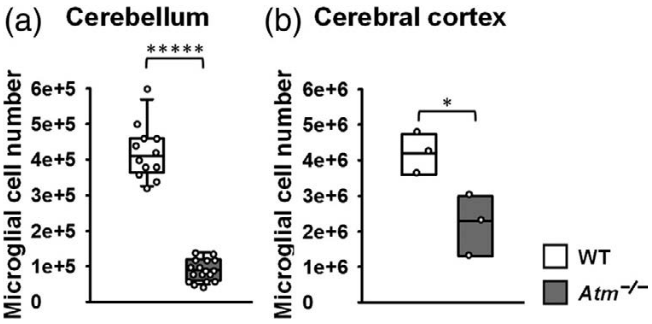

FIGURE 2 The yield of purified Iba-1-positive cells isolated from WT and *Atm*$^{-/-}$ cerebellar and cerebral cortical mixed glial cultures. Plots of numbers of purified Iba-1-positive cells derived from mixed glial cultures prepared from WT ($n = 12$) and *Atm*$^{-/-}$ ($n = 17$) cerebella and cerebral cortices ($n = 3$). Significance determined by two-tailed Student's *t*-test unequal variance. *$p < 0.05$, *****$p < 0.0001$

deficiency leads to microglial activation, we measured the lengths of the processes of cultured, purified microglial cells. Since it is problematic to determine whether each protuberance is indeed a real process, we measured the length of the microglial processes. The average length of the processes of the cerebellar WT microglia was 28.05 ± 13.8 A.U. as compared to 5.22 ± 2.4 A.U. in Atm-deficient cells ($p < 2E{-}25$) (Figure 3a,b). In contrast to cerebellar microglia, there was not a significant difference between the lengths of the cerebral cortical WT microglial cell processes (32.1 ± 15.1 A.U.) and *Atm*$^{-/-}$ microglial processes (27.6 ± 16.6 A.U.) (Figure 3c,d, $p < 0.1$).

To further confirm that Atm deficiency leads to microglial activation in the whole cerebellum, we immuno-reacted cerebellar sections derived from 1.5-month-old WT and *Atm*$^{-/-}$ with antibodies to Iba1, a marker of macrophages and microglia, and F4/80, which serves as a marker of microglial activation (Jurga et al., 2020; Wada et al., 2000). We found a 5-fold increase in the number of cells labeled with F4/80 antibody in *Atm*$^{-/-}$ cerebella. Moreover, most of the WT microglia assume ramified morphology with extended processes (Figure 3e). In contrast, the *Atm*$^{-/-}$ microglia are markedly less ramified and have amoeboid morphology indicative of their activated state as previously reported (Quek et al., 2017a, 2017b; X. Song et al., 2019).

To quantify the activated microglia cultured from WT and *Atm*$^{-/-}$ cerebella and cerebral cortices, we counted the quantity of bipolar non-activated as well as amoeboid and unipolar activated microglia (Figure 4 and Figure S3). Quantification of the different microglial morphologies showed that only 42% of the cultured WT cerebellar microglial cells had resting ramified or bipolar appearance, and around 58% of the cells had either amoeboid or unipolar morphologies indicative of activated status (Figure 5a). In cultures of Atm-deficient cerebellar microglial cells, 75% of microglia were activated [amoeboid (50%) and the unipolar (25%)] (Figure 5b). In contrast to cerebellar microglia, most of the cerebral cortical microglia were non-activated; 55% of cells in WT cultures and 53% in Atm-deficient cultures were ramified or bipolar in appearance (Figure 5c,d). Activated amoeboid and unipolar morphologies were present at 29% and 16%, respectively, in WT cultured cerebral cortical microglia and at 30% and 17%, respectively, in *Atm*$^{-/-}$ cells (Figure 5c,d). Thus, the frequency of activated microglial cells was higher in the WT cerebella than in cerebral cortex, and loss of Atm

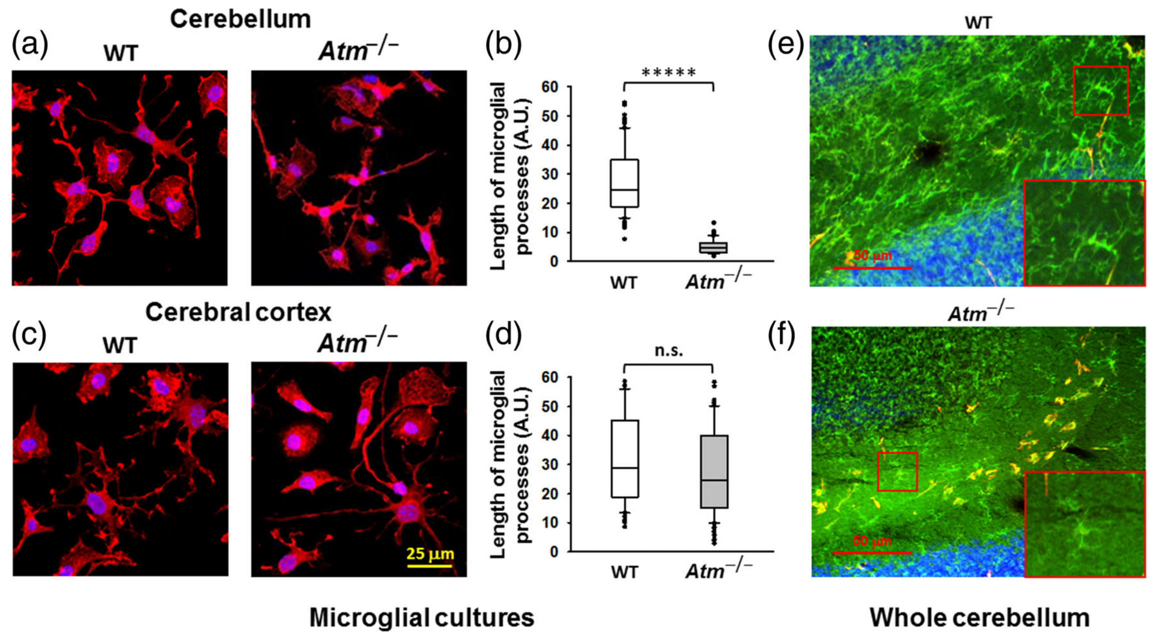

FIGURE 3 Atm deficiency reduces the length of cerebellar microglial processes. (a) Representative confocal images of cultured WT and *Atm*$^{-/-}$ cerebellar microglia stained for microglial marker Iba-1 (red) and nuclei (with DAPI, blue). (b) Quantification of the lengths of cerebellar microglial processes with ImageJ software. (c) Representative confocal images of cultured WT and *Atm*$^{-/-}$ cerebral cortical microglia stained for microglial marker Iba-1 (red) and nuclei (with DAPI, blue). (d) Quantification of the lengths of cerebral cortical microglial processes with ImageJ software. (e and f) Representative micrographs of cerebellar sections derived from (e) WT and (f) *Atm*$^{-/-}$ mice stained with Iba1 (green) shows ramified, non-activated microglia with long processes. Nuclei were stained with DAPI (blue). Immunostaining with anti-F4/80 antibody (red) shows unramified activated microglia in cerebellum sections of 1.5-month-old *Atm*$^{-/-}$ mice. Significance determined by two-tailed Student's *t*-test unequal variance. *****$p < 0.0001$

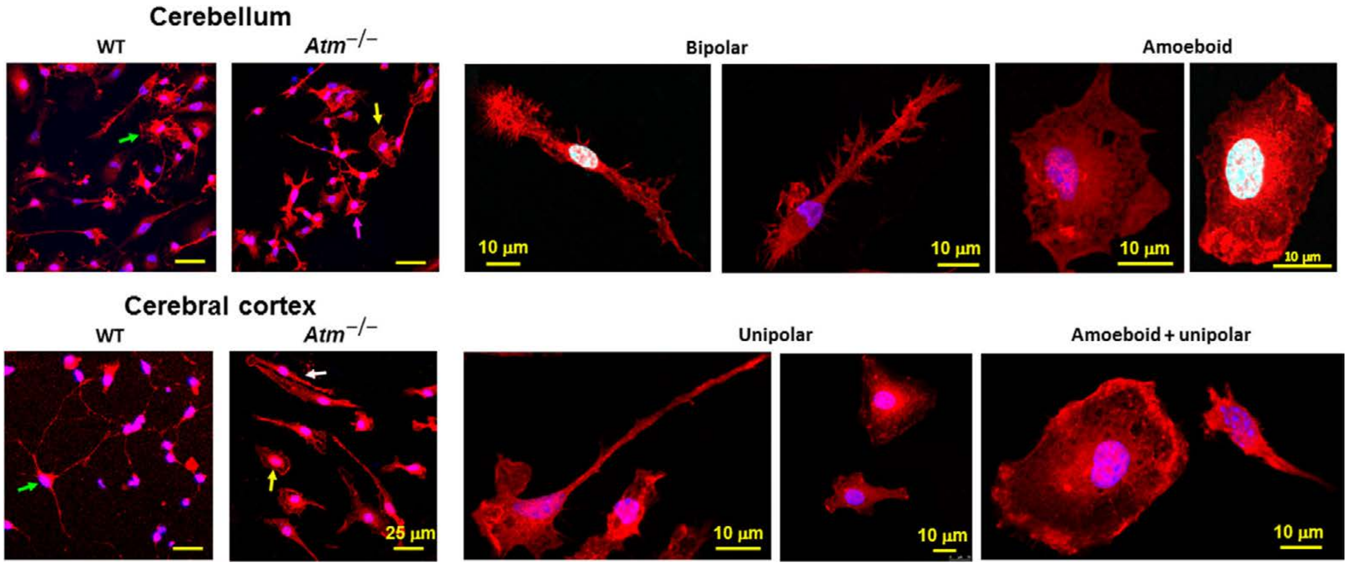

FIGURE 4 Microglial cells derived from *Atm*$^{-/-}$ mice have different morphologies than those derived from WT mice. Left-most panels: Representative confocal images of WT and *Atm*$^{-/-}$ cerebellar microglia stained for microglial marker Iba-1 (red) and nuclei (with DAPI, blue). Green arrows indicate ramified microglial cells, white arrows indicate bipolar microglia, and pink and yellow arrows indicate unipolar or amoeboid cells, respectively. Scale bars, 25 μm. Right panels: Magnified images of resting bipolar microglia and activated amoeboid and unipolar microglial cells from WT cultures. Scale bars, 10 μm

resulted in abnormal activation in cerebella but not cerebral cortex. These results support the notion that cerebellar and cerebral cortical microglia have different innate properties.

One of the characteristics of activated microglia is the enlargement of their soma size (Davis et al., 2017). To test whether Atm deficiency led to increased soma area of activated microglia, we

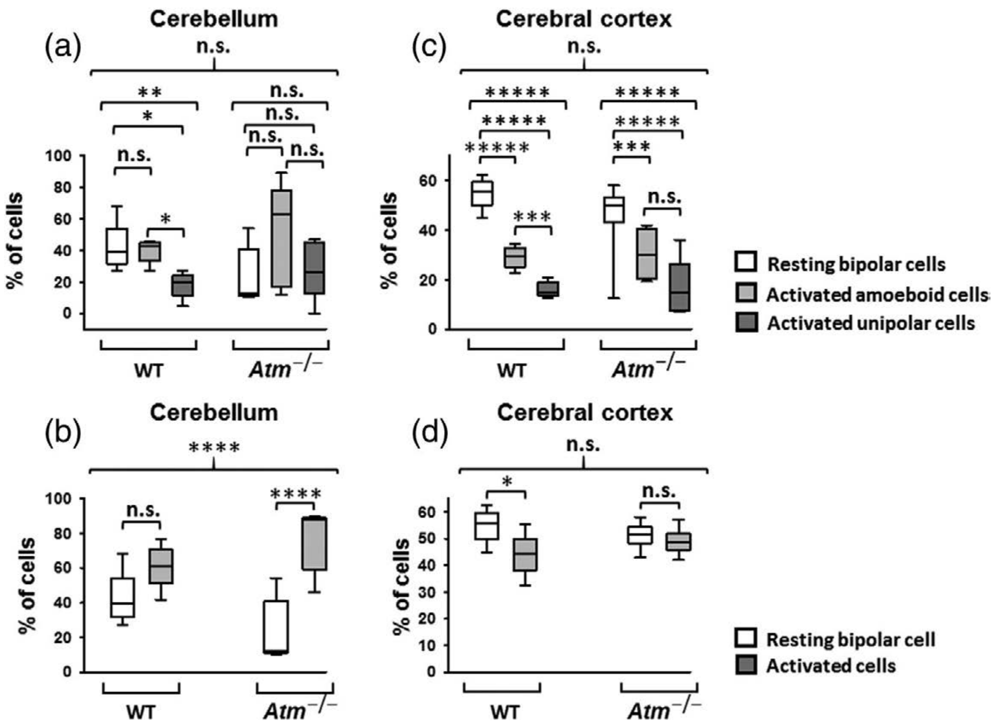

FIGURE 5 Quantification the distribution of resting versus activated microglial derived from WT and *Atm*$^{-/-}$ cerebella and cerebral cortices. (a) Quantification of resting and activated microglia from purified microglial cultures prepared from cerebella derived of WT and *Atm*$^{-/-}$ mice ($n \geq 5$). (b) Quantification of resting, amoeboid, and unipolar microglia from purified microglial cultures prepared from cerebella derived of WT and *Atm*$^{-/-}$ mice ($n \geq 5$). (c) Quantification of resting and activated microglia from purified microglial cultures prepared from cerebral cortices derived of WT and *Atm*$^{-/-}$ mice ($n \geq 5$). (d) Quantification of resting, amoeboid, and unipolar microglia from purified microglial cultures prepared from cerebral cortices derived of at least five WT and five *Atm*$^{-/-}$ mice ($n \geq 5$). Statistical analyses: one-way ANOVA and unequal variant Student's *t*-test

measured the soma size of cultured WT and *Atm*$^{-/-}$ microglia derived from the cerebellum and cerebral cortex. The average area of cerebellar bipolar microglia was 31% larger than that of the average area of cerebral cortical microglia, and the average area of the cerebellar amoeboid cells was 25% larger than that of amoeboid cells in the cerebral cortex (Figure S4). In Atm-deficient cerebellar cultures, the average area of bipolar microglia was significantly higher relative to that of WT cells by 36%; in the cerebral cortex cultures, it was higher by 33%. Atm inactivation also increased the average area of the cerebellar amoeboid cells by 33% but had no effect on the cerebral cortical amoeboid microglia. Collectively, these data show that both location and the presence of Atm influences microglial morphology.

3.3 | Atm deficiency accelerates cell migration in *Atm*$^{-/-}$ microglia

Microglia are highly motile cells, capable of surveying the brain to maintain neuronal and astrocytic functionality. To investigate the effects of microglial origin and Atm in microglial cell migration, cerebellar and cerebral cortical cultures of purified microglia were subjected to a migration assay. Surprisingly, our results showed that Atm deficiency in cerebellar microglia significantly elevated their migration capabilities compared to WT cells (Figure 6a and Figure S5). In contrast to cerebellar microglia, the migration capabilities of *Atm*$^{-/-}$ cerebral cortex microglia were slightly but significantly reduced compared to WT cells (Figure 6b and Figure S6). Interestingly, astrocytes, which are considered to be more “territorial cells” (Bushong et al., 2004), had better migration capacities than microglial cells. The migration rate of cerebellar *Atm*$^{-/-}$ astrocytes was significantly lower than that of WT (Figure 6C and Figure S7). On the other hand, the migration capabilities of cerebral cortical WT and *Atm*$^{-/-}$ astrocytes were indistinguishable (Figure 6d and Figure S8). The migration rate of WT cerebellar and cerebral cortical microglia were similar (Figure 6e) and reached around 20% gap confluence at a very early stage and remained unchanged for at least 24 h. In contrast to microglia, the migration rate of astrocytes was almost linear (the R^2 of cerebellar WT is 0.9906 and 0.9873 for *Atm*$^{-/-}$) for up to 72 h. Whereas Atm deficiency in the cerebellum accelerated the migration rate of cerebellar microglia, no such acceleration was evident in cerebral cortical microglia (Figure 6f). These results suggest that Atm expression rather than microglia origin is the dominant factor that regulates cell migration. On the other hand, origin mainly determines the migration rates of astrocytes, and Atm has a marginal effect on astrocytic cell migration (Figure 6g,h).

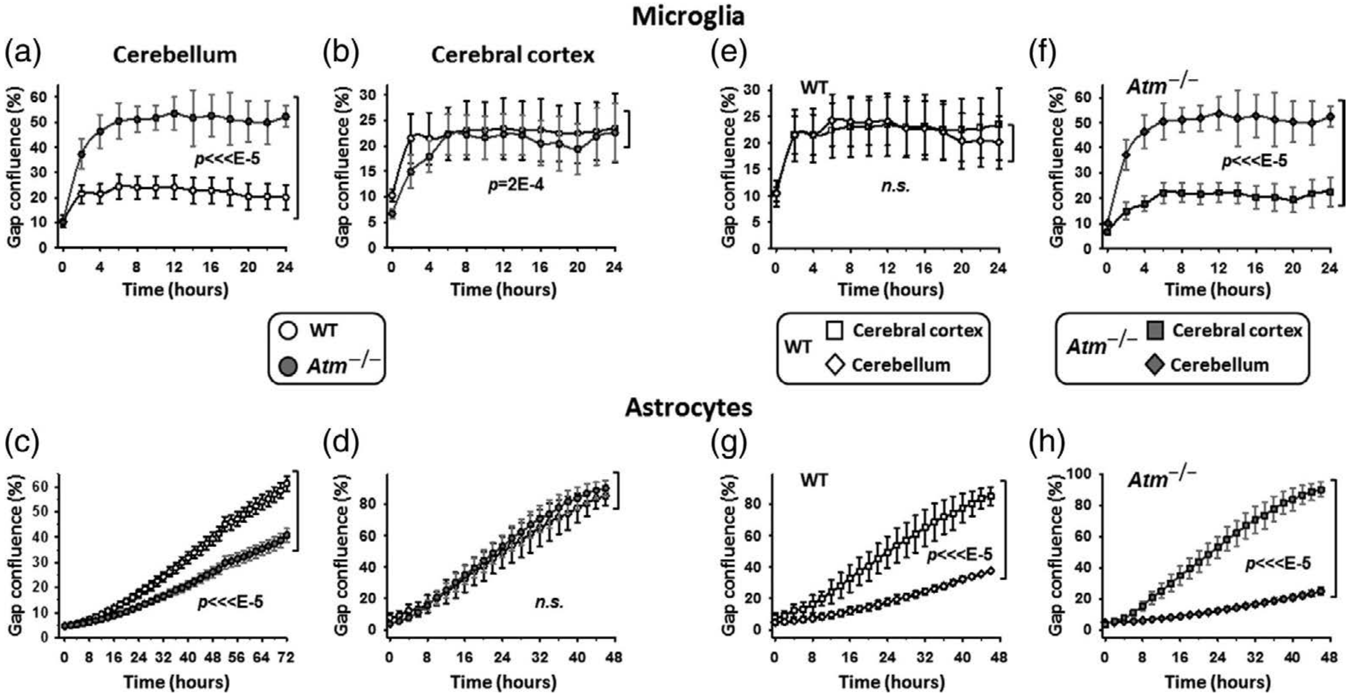

FIGURE 6 Atm deficiency significantly increases cell migration of cerebellar but not of cerebral cortical microglia. (a–d) Quantification of percent cell migration on cultures of (a) WT ($n = 7$) and *Atm*$^{-/-}$ ($n = 4$) cerebellar microglia, (b) WT ($n = 9$) and *Atm*$^{-/-}$ ($n = 5$) cerebral cortical microglia, (c) WT ($n = 10$) and *Atm*$^{-/-}$ ($n = 6$) cerebellar astrocytes (the R^2 of cerebellar WT is 0.9906 and that for *Atm*$^{-/-}$ is 0.9873), and (d) WT ($n = 7$) and *Atm*$^{-/-}$ ($n = 4$) cerebral cortical astrocytes (the R^2 of cerebellar WT is 0.9952 and that for *Atm*$^{-/-}$ is 0.9927). (e) Comparison between the migration rates of WT cerebellar and cerebral cortical microglia. (f) Similar to E but for microglia derived from Atm-deficient cerebella and cerebral cortices. (g) Comparison between the migration rates of WT cerebellar and cerebral cortical astrocytes. (h) Similar to G but for astrocytes derived from Atm-deficient cerebella and cerebral cortices. Statistical analyses: two-sample Kolmogorov–Smirnov test

3.4 | ROS production is increased in *Atm*$^{-/-}$ cerebellar microglia

It has been shown that Atm deficiency leads to oxidative stress, especially in the cerebellum (Kamsler et al., 2001; Stern et al., 2002). Elevated ROS levels due to Atm loss are involved in increased cell migration through Rac1 activation; oxidative stress directly activates Rac1 resulting in cytoskeleton reorganization (Tolbert et al., 2019). To evaluate the connection between cell migration and oxidative stress, we analyzed the ROS levels in WT and *Atm*$^{-/-}$ microglia derived from the cerebellum and the cerebral cortex. We treated the microglia cultures with DCFH-DA and measure its oxidation to 2′,7′-dichlorofluorescin (DCF) due to the presence of ROS. The intensity of DCF fluorescence is proportional to the ROS levels. To account for effects of altered cell proliferation or cell death on DCF levels in the various genotypes and regions, the DCF levels were normalized to the number of viable cells in each measurement. In Atm-deficient cerebellar cultures, ROS levels were significantly higher than in WT cultures by 45% (Figure 7a). In contrast, ROS levels in Atm-deficient cerebral cortical microglial cultures were slightly but not significantly reduced (Figure 7a). In contrast to microglial cells, there were no significant differences in ROS levels between cerebellar WT and *Atm*$^{-/-}$ astrocytes, but levels of ROS were significantly lower in *Atm*$^{-/-}$ cerebral cortical astrocyte cultures than in WT cerebral cortical astrocyte cultures (Figure 7b).

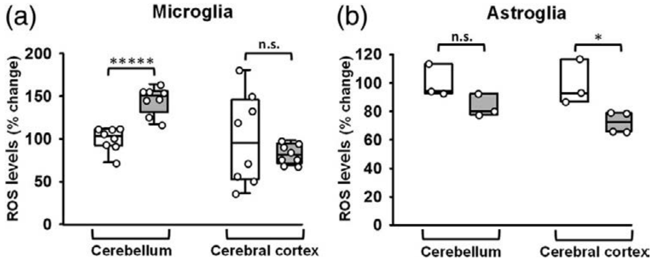

FIGURE 7 ROS levels are higher in *Atm*$^{-/-}$ cerebellar and lower in *Atm*$^{-/-}$ cerebral cortical astrocyte cultures. ROS levels in cultures of WT and *Atm*$^{-/-}$ (a) microglia and (b) astrocyte cultures. Fluorescence was normalized to numbers of living cells in cultures ($n = 8$) for microglia (cerebellum and cerebral cortex) and $n =$ 3-4 for astrocytes (cerebellum and cerebral cortex). The Kolmogorov–Smirnov normality test shows that all the data are in the 95% region of acceptance. Statistical analyses: two-tailed Student's t-test unequal variance. $^*p < 0.05$, $^{*****}p < 0.0001$

3.5 | Functionality of *Atm*$^{-/-}$ cerebellar microglia is impaired

Microglia phagocytose and degrade infectious agents (Neumann et al., 2009), extracellular protein aggregates, and apoptotic cell debris thereby regulating inflammation and protecting neurons

(Fu et al., 2014). In addition to these functions in pathogenic conditions, microglial phagocytosis is also involved in CNS development and synaptogenesis as microglia eliminate malfunctioning synapses (Brown & Neher, 2014). Inadequate microglial phagocytic ability leads to abnormal synaptic connections and accumulation of aggregated proteins (Lian et al., 2016; Schafer et al., 2012). Using latex beads as substrates, we measured the phagocytic activities of microglial and astroglial cells derived from WT and *Atm*$^{-/-}$ cerebella and cerebral cortices. Using FACS analyses, we measured the phagocytic activity of WT and *Atm*$^{-/-}$ cerebellar and cerebral microglial cells (Figure 8a–d). More than 80% of the microglial cells derived from WT and *Atm*$^{-/-}$ cerebellar microglial cells took up inert fluorescent beads (Figure 8e). Per cell, there was significantly more signal in WT cerebellar microglia than in *Atm*$^{-/-}$ cells (Figure 8b,f). There was a slight and non-significant reduction in phagocytic activity for *Atm*$^{-/-}$ cerebral cortical microglia compared to WT, and the amount of phagocytosis per cell did not differ significantly (Figure 8g,h). Similarly to microglia, around 80% of the WT and the *Atm*$^{-/-}$ cerebellar astrocytes showed phagocytic activity (Figure S9a). A slight, non-significant reduction was measured in the phagocytic signal per cell detected in *Atm*$^{-/-}$ cerebellar astrocytes (Figure S9b), and there were small, non-significant reductions in the percentage of *Atm*$^{-/-}$ cortical astrocytes capable of phagocytosis of the latex beads (Figure 9c) and in the phagocytic signal per cell detected in *Atm*$^{-/-}$ cerebral cortical astrocytes compared to WT cells (Figure S9d). Together, these results suggest that loss of Atm impairs phagocytic activity of microglia from the cerebellum but not the cerebral cortex. In contrast, Atm deficiency did not affect the phagocytic activity of cerebellar or cerebral cortical astrocytes.

3.6 | Atm deficiency downregulates the expression of key proteins in cerebellar microglia

In the healthy brain, microglia are in close contact with the dendrites and synapses of neighboring neurons (Wu et al., 2015). Microglia secrete neurotrophic factors such as BDNF that remodel synapses and maintain proper neuronal network function (M. Song et al., 2017). Using western blot analysis, we examined the pro-BDNF (34 kDa) produced by WT and *Atm*$^{-/-}$ microglia. Levels of pro-BDNF were reduced by 87% in cerebellar *Atm*$^{-/-}$ microglia lysates compared to WT lysates (Figure 9a), indicating that pro-BDNF might play a role in the abnormalities seen concerning learning and motor-function in A-T disease. The 14-kDa mature form of BDNF could not be detected in most samples, due to the young age of the animals tested (P4). At this age, the dominant form of BDNF is the pro-BDNF (Hempstead, 2015; Ulmann et al., 2008).

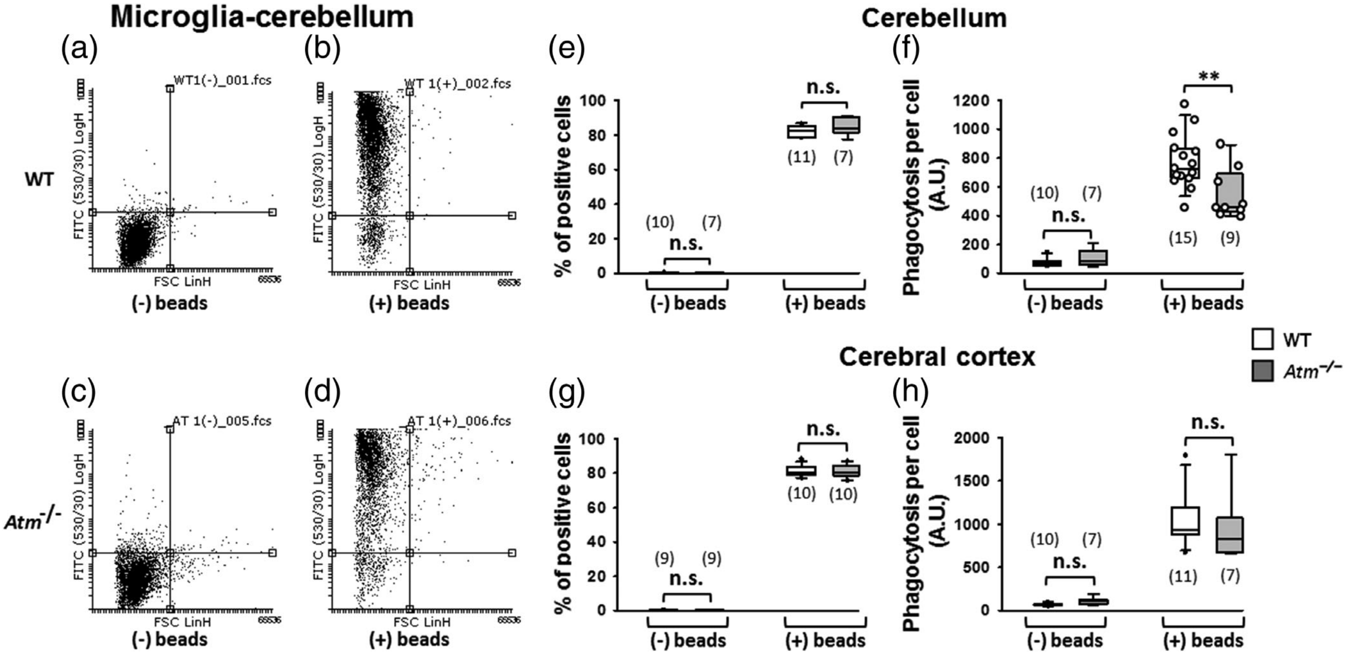

FIGURE 8 *Atm*$^{-/-}$ deficiency decreases the phagocytic activity of cerebellar but not in cerebral cortical microglia. (a–d) Flow cytometry analysis of phagocytosis by microglial cells derived from WT and *Atm*$^{-/-}$ mice for (a) untreated WT cultured purified microglia, (b) WT cultured purified microglia treated with fluorescently labeled latex beads, (c) untreated *Atm*$^{-/-}$ cultured purified microglia and (d) *Atm*$^{-/-}$ cultured purified microglia treated with fluorescently labeled latex beads. (e) Percent of WT and *Atm*$^{-/-}$ cerebellar microglia that phagocytose latex beads. (f) Fluorescence intensity per cell for WT and *Atm*$^{-/-}$ cerebellar microglia. (g) Percent of WT and *Atm*$^{-/-}$ cerebral cortex microglia that phagocytose latex beads. (h) Fluorescence intensity per cell for WT and *Atm*$^{-/-}$ cerebral cortex microglia. The data presented in the figures are the fluorescent intensity of the stained cells compared to the fluorescent intensity per cell of the unstained cells, which was around 23%. The numbers of mice used in each experiments are shown in the graph. Statistical analyses: two-tailed unequal Student's *t*-test). $^{**}p < 0.01$

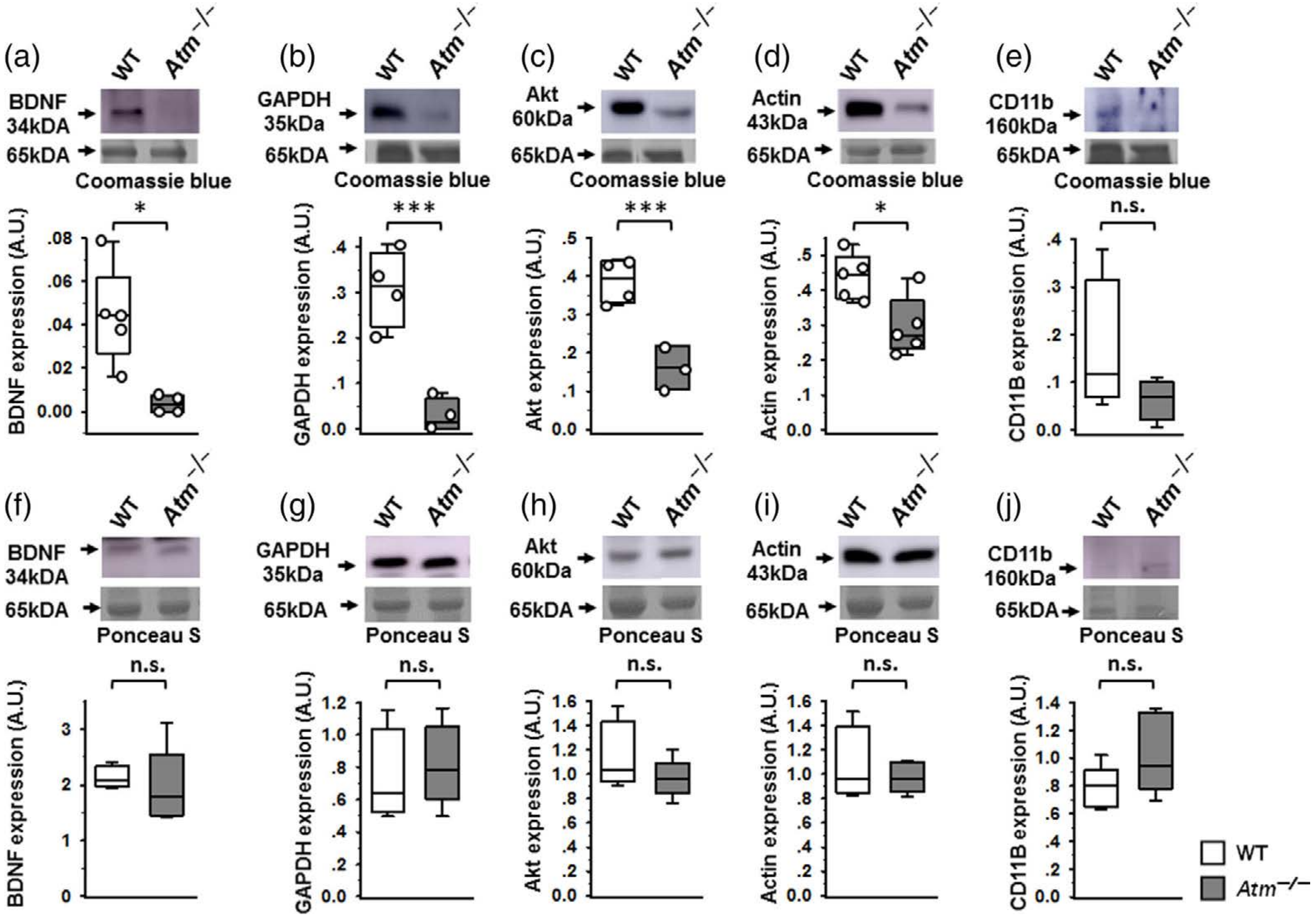

FIGURE 9 Altered protein expression levels in *Atm*$^{-/-}$ CD11b-positive cells derived from mouse cerebella. (a–e) Upper: Representative western blots of (a) pro-BDNF protein, (b) GAPDH protein, (c) Akt, (d) actin, and (e) CD11b in lysates of microglia derived from WT and *Atm*$^{-/-}$ cerebella. Lower: Quantification of protein levels in cerebellar lysates normalized to selected Coomassie blue stained bands ($n = 3$–5). (f–j) Upper: Representative western blots of (f) pro-BDNF, (g) GAPDH, (h) Akt, (i) actin, and (j) CD11B in lysates of WT and *Atm*$^{-/-}$ microglia derived from cerebral cortices. Lower: Quantification of protein levels in cerebral cortex lysates normalized to selected Ponceau S red stained bands ($n = 3$–5). Statistical analyses: two-tailed unequal Student's *t*-test. *$p < 0.05$, ***$p < 0.005$

The housekeeping GAPDH is often used for normalized of protein levels by western blot (Mergia et al., 2003; Rao et al., 1997; N. Wang et al., 2017). GAPDH functions in both cytoplasmic and nuclear pathways (Kornberg et al., 2010), and, in addition to its well-known glycolytic functions, GAPDH regulates gene transcription, RNA transport, DNA replication (Sirover, 1999), and the initiation of apoptosis once oxidative stress occurs (Nakajima et al., 2017). It is possible that in certain cells or in response to certain stimuli, GAPDH levels are altered. In repeated experiments, we observed a significant reduction of 91.2% in the expression levels of GAPDH protein in *Atm*$^{-/-}$ cerebellar microglial cells compared to WT cells (Figure 9b). Thus, not only was GAPDH unreliable as a control protein, its levels appear be affected by Atm deficiency.

ATM and AKT intersect in several pathways (Halaby et al., 2008; Khalil et al., 2011). Interestingly, *Akt*$^{-/-}$ and *Atm*$^{-/-}$ mice are similar in terms of phenotypic abnormalities such as growth retardation, defects in the maturation of the immune system, infertility, resistance to insulin, and radiosensitivity (Barlow et al., 1996; W. S. Chen et al., 2001). The significant reduction of 58% seen in Akt in the *Atm*$^{-/-}$ cerebellar microglia cells supports a role of Akt in Atm-dependent pathways (Figure 9c), supporting conclusions of other studies (W. S. Chen et al., 2001; Khalil et al., 2011).

Like GAPDH, actin is also widely used for normalization in protein quantification experiments. As with GAPDH, there was a clear disparity in actin levels between *Atm*$^{-/-}$ and WT cerebellar microglial cells. Actin levels in *Atm*$^{-/-}$ microglia were significantly lower by 33% (Figure 9d). Actin is a cytoskeleton protein, and its cleavage has an effect on microglial cell morphology and motility (Franco-Bocanegra et al., 2019). We assumed that the reduced actin levels observed in *Atm*$^{-/-}$ cerebellar microglia would result in the formation of stress fibers that support higher motility of microglia. We tested this possibility and found no evidence for elevated levels of actin stress fibers (Figure S10). Thus, alterations in actin levels do not explain alterations in microglial migration.

CD11b, also known as integrin αM, is a membrane protein that serves a marker of microglia and macrophages. This protein is involved in phagocytosis and cell migration. Western blot analyses revealed a non-significant 55% reduction, in the expression of CD11b in *Atm*$^{-/-}$ cerebellar microglia compared to WT cerebellar microglia (Figure 9e). Remarkably, no alterations in the expression of pro-BDNF, GAPDH, Akt, actin, and CD11b were detected in cerebral cortical *Atm*$^{-/-}$ microglia (Figure 9f–j). This shows that cerebral cortical microglia are fundamentally different than cerebellar microglia.

3.7 | Atm deficiency impairs the functionality of cerebellar microglial mitochondria

In metabolically active cells, MTT is reduced to a formazan by the mitochondrial succinate dehydrogenase (SDH). This enzyme has a role both in the citric acid cycle as well as in electron transport. When cells die, their mitochondria lose the ability to convert MTT into formazan, thus color formation serves as a useful and convenient marker of mitochondrial activity (Berridge & Tan, 1993). To insure that we measured mitochondrial activity and not cell viability, the MTT assay data were normalized to viability as monitored by methylene blue staining. The conversion of MTT to formazan in viable *Atm*$^{-/-}$ cerebellar microglia was significantly lower, by 39%, compared to WT cells, but there was no difference between mitochondrial activity in WT and *Atm*$^{-/-}$ cerebral cortical microglia (Figure 10a), indicating that Atm deficiency specifically affects the mitochondrial functionality of cerebellar microglia. Similar to effects on microglia, Atm deficiency significantly reduced mitochondrial activity in cerebellar astrocytes but not in cerebral cortical astrocytes (Figure 10b).

Based on these findings, we looked more closely at the role of Atm in mitochondrial functionality in microglia and astrocytes. To reveal mitochondrial involvement in Atm-dependent pathways, we first used MitoTracker green, which stains mitochondria regardless of their membrane potential (Reipert et al., 1995). FACS analyses (Figure 11a–d) of percentage of MitoTracker green-positive cells showed a similar percentage of labeled cells in WT and *Atm*$^{-/-}$ cerebellar microglia (55 ± 20.05% and 63 ± 10.43%, respectively) and in WT and *Atm*$^{-/-}$ cerebral cortical labeled (60.74 ± 9.98% and 69.72 ± 5.93% respectively). However, the fluorescence intensity per cell was significantly higher (1.48-fold increase) in the cerebellar *Atm*$^{-/-}$ cells (Figure 11e) but not in cerebral cortex *Atm*$^{-/-}$ cells (Figure 11f). The percentages of MitoTracker-labeled cerebellar WT and *Atm*$^{-/-}$ astrocytes were 88% and 94%, respectively, and fluorescence intensities of the MitoTracker signal per cell was similar between WT and *Atm*$^{-/-}$ astrocytes derived from both cerebellum (Figure 11g) and cerebral cortex (Figure 11h). MitoTracker green passively diffuses across the plasma membrane and accumulates in the inner mitochondrial membrane (Camilleri-Broet et al., 1998). The high fluorescent intensity per cell may be due to an increase in mitochondrial permeability suggestive of apoptosis; however, since these cells are viable, we assume that increased staining reflects a higher mitochondrial mass in *Atm*$^{-/-}$ cerebellar microglia.

To measure mitochondrial membrane potential, we used TMRE. In healthy cells, the mitochondrial membrane potential is approximately −140 mV (Gerencser et al., 2012). One of the essential components in the generation of mitochondrial membrane potential is cytochrome C, which promotes the pumping of protons into the mitochondrial intermembrane space as it shuttles electrons from Complex III to Complex IV along the electron transport chain. The release of cytochrome C during certain types of cell death impairs the ability of the mitochondria to maintain their proper membrane potential (Huttemann et al., 2011). The collapse of the mitochondrial transmembrane potential coincides with the opening of the mitochondrial permeability transition pores, leading to the release of cytochrome C into the cytosol. TMRE analyses revealed similar percentages of TMRE-labeled WT and *Atm*$^{-/-}$ cerebellar microglia (90.6% and 93.5%, respectively), but significantly lower, by 65%, membrane potential in cerebellar *Atm*$^{-/-}$ microglial cells (Figure 12a–e). In contrast to cerebellar microglial cells, no differences were observed between cerebral cortical WT and *Atm*$^{-/-}$ microglial with respect to TMRE labeling or mitochondrial membrane potential (Figure 12f). The percentages of TMRE-labeled cerebellar WT and *Atm*$^{-/-}$ astrocytes were 88% and 94%, respectively, and in the cerebral cortex the percentages were 95% and 84%, respectively. Atm deficiency did not affect the mitochondrial membrane potential of cerebellar astrocytes (Figure 12g). Interestingly, the mitochondrial membrane potential in the Atm-deficient cerebral cortical astrocytes was significantly higher than in WT cells (Figure 12h). Thus, Atm deficiency selectively reduces the mitochondrial membrane potential of cerebellar but not cerebral cortical microglia. The effects are different in astrocytes as loss of Atm

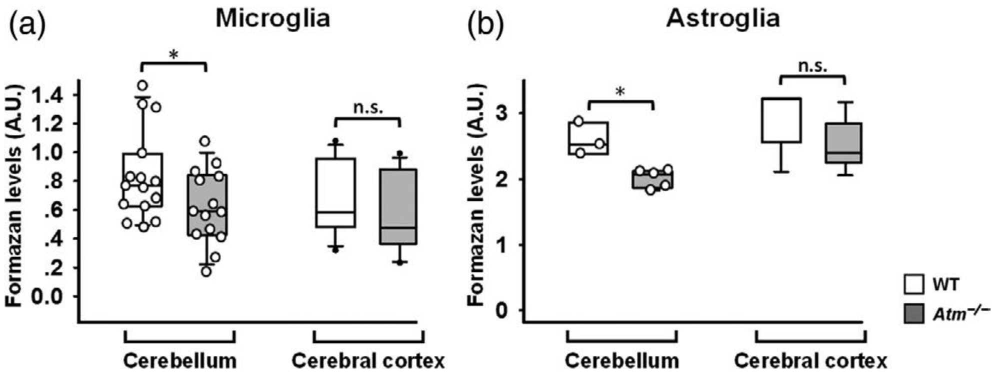

FIGURE 10 Mitochondrial activity is low in cerebellar *Atm*$^{-/-}$ microglia and astroglia. (a) Formazan levels in WT cerebellar ($n = 15$) and *Atm*$^{-/-}$ ($n = 14$) and cortical microglia ($n = 4$). (b) Formazan levels in *Atm*$^{-/-}$ and WT cerebellar and cortical astrocytes ($n = 3$–5). Statistical analyses: two-tailed Mann–Whitney test. $^{*}p < 0.05$

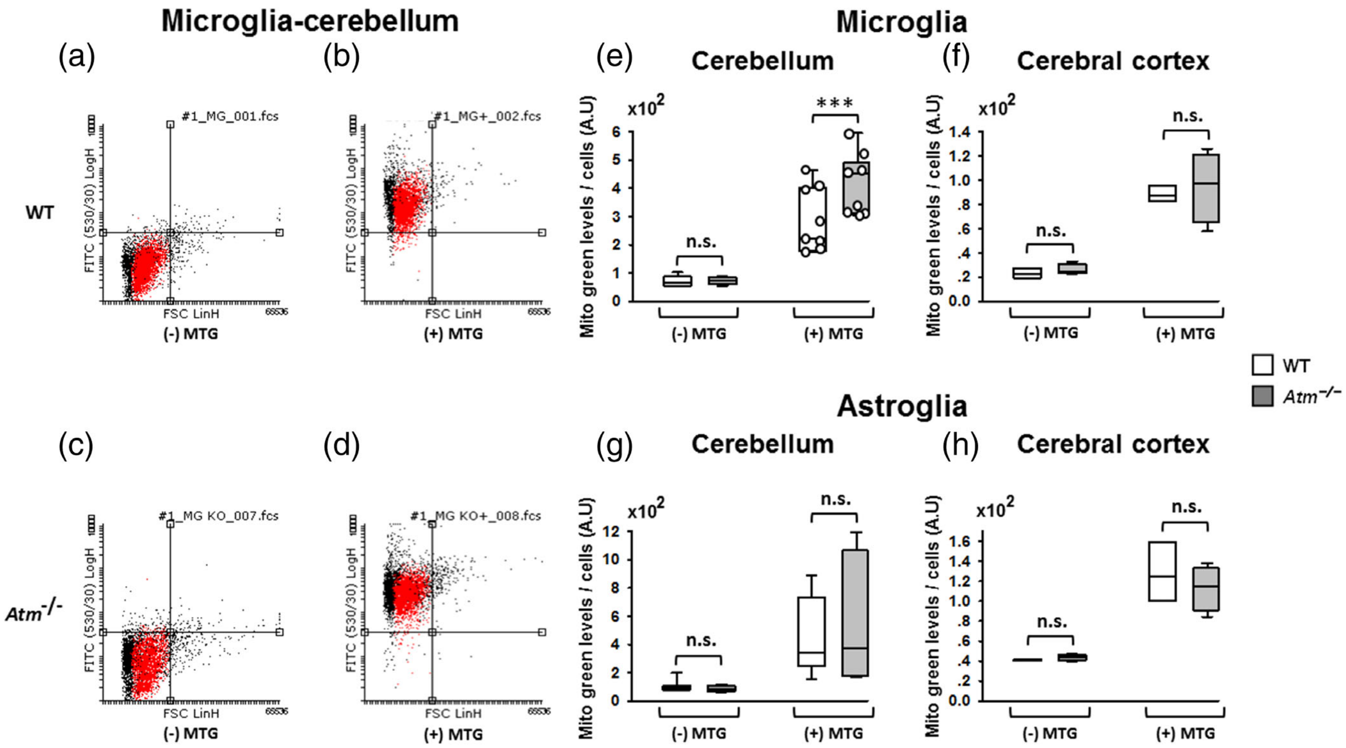

FIGURE 11 Atm deficiency increases the mitochondrial mass in cerebellar but not in cerebral cortical microglia. (a–d) Flow cytometry analysis of Mito-tracker green (MTG) uptake into microglial cells derived from WT and *Atm*$^{-/-}$ mice. Cells were (a) WT purified microglia cultured without MTG, (b) WT purified microglia exposed to fluorescently labeled MTG, (c) *Atm*$^{-/-}$ purified microglia cultured without MTG, and (d) *Atm*$^{-/-}$ purified microglia exposed to fluorescently labeled MTG. MTG labels mitochondria regardless of their membrane potential. (e) Quantification of MTG levels per microglial cell derived from WT and *Atm*$^{-/-}$ cerebella. (f) Quantification of mitochondrial masses in microglia derived from WT and *Atm*$^{-/-}$ cerebral cortex. (g) Quantification of MTG levels per astrocytes derived from WT and *Atm*$^{-/-}$ cerebella. (h) Quantification of mitochondrial masses in astrocytes derived from WT and *Atm*$^{-/-}$ cerebral cortex. Statistical analyses: two-tailed unpaired Student's *t*-test; $n = 4–8$; ***$p < 0.005$

resulted in no change in cerebellar astrocytes and increased the potential in cerebral cortical astrocytes.

4 | DISCUSSION

A-T is a pleotropic genetic disorder characterized by developmental abnormalities and by a progressive neuronal loss in the cerebellum, while the cerebral cortex remains relatively intact (Gatti et al., 2001; Shiloh, 2003). Our results show that *Atm*$^{-/-}$ cerebellar, but not cerebral cortical, microglia have significantly impaired phagocytosis, accelerated cell migration, elevated ROS levels, diminished secretion of neurotrophic factors, and hampered mitochondrial activity. Moreover, the effects of Atm deficiency on cerebellar and cerebral cortical astroglia are markedly different. These observations are compatible with the notion that microglia and astrocytes are heterogeneous populations of cells with region-specific characteristics. This hypothesis is supported by evidence showing that under physiological conditions and upon deleterious stimuli microglia exhibit distinct turnover rates, extents of self-renewal, growth factor release, metabolism, and radiosensitivities, and differences in functions such as synaptic modeling, myelination, and vascular remodeling (Menzel et al., 2018; Stratoulias et al., 2019). The mechanisms by which cerebellar and cerebral cortical microenvironments as well as Atm deficiency alter the phenotypic behavior and the functionality of microglial cells is not well understood. Differences in cerebellar and cortical microglia might stem from disease-associated signaling, differences in cell types, microenvironments, redox state, and metabolites.

Together, our results support the notion that Atm-proficient microglia can exert protective effects. In contrast, Atm deficiency in microglia can alter cerebellar homeostasis in a way that contributes to cerebellar demise. The importance of fully functional microglia for neuronal survival was suggested previously by Song et al. (X. Song et al., 2019) who showed that Atm inhibition caused severe structural damage to cultured neurons most likely by the secretion of neurotoxic substances. The finding that Purkinje neurons are dynamically surveyed by a special type of microglial cells strengthens the notion that Purkinje cell survival and functionality are heavily dependent on microglia (Stowell et al., 2017).

We did not find any evidence for microglial cell proliferation in purified cultures regardless of Atm expression or their origin (Figure S2). In contrast, astrocytes are fully proliferative in purified cultures. These results suggest that specific signals, which are lacking in the microglial cell cultures, are needed to induce proliferation. This

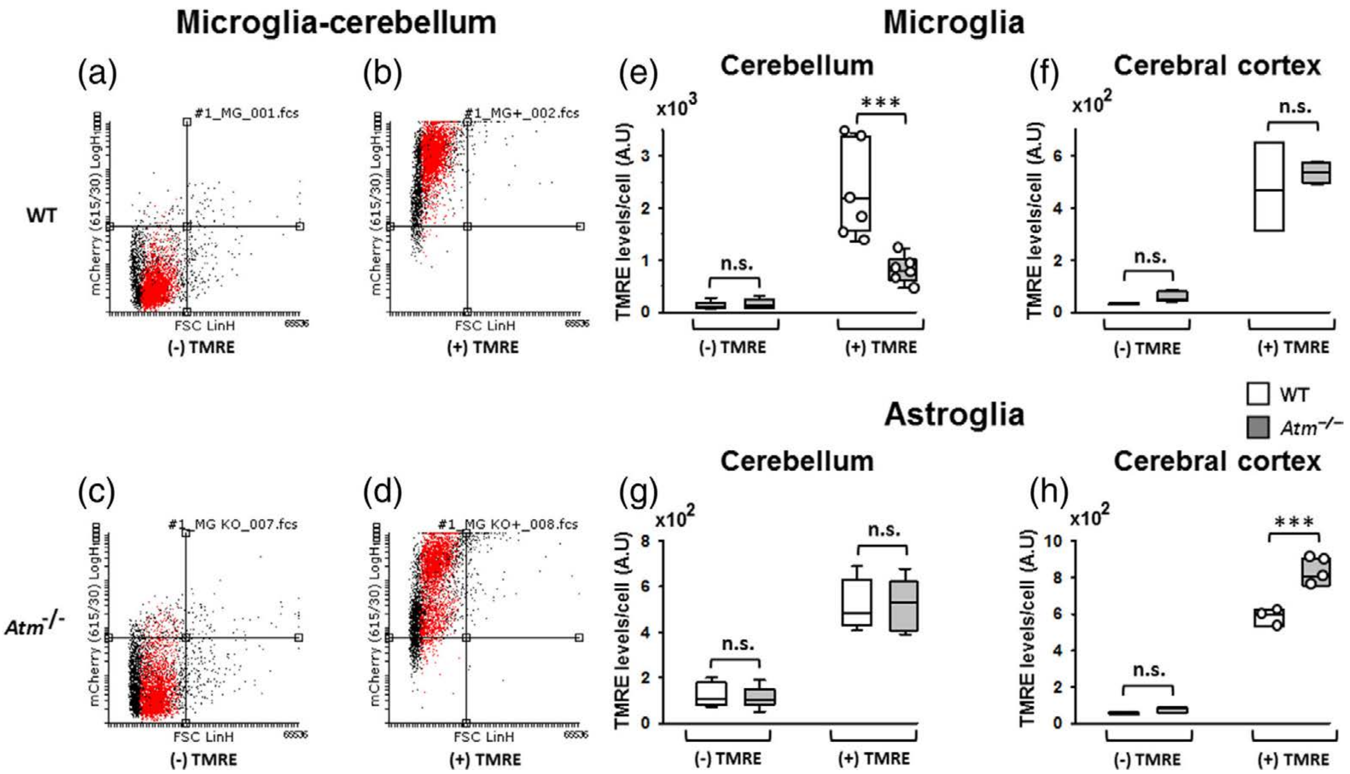

FIGURE 12 Atm deficiency decrease the mitochondrial membrane potential in cerebellar and increase in cerebral cortical microglia. (a–d) Flow cytometry analysis of tetramethylrhodamine ethyl ester (TMRE) uptake into microglial cells from WT and *Atm*$^{-/-}$ mice. Cells were (a) WT purified microglia cultured without TMRE, (b) WT purified microglia treated with fluorescently labeled TMRE, (c) *Atm*$^{-/-}$ purified microglia cultured without TMRE, (d) *Atm*$^{-/-}$ cultured purified microglia treated with fluorescently labeled TMRE. (e) Quantification of TMRE levels per microglial cell derived from WT and *Atm*$^{-/-}$ cerebella. (f) Mitochondrial membrane potential in microglial cells derived from WT and *Atm*$^{-/-}$ cerebral cortices ($n = 6$ WT and 3-4 *Atm*$^{-/-}$ mice). (g) Quantification of TMRE levels per astrocyte derived from WT and *Atm*$^{-/-}$ cerebella. (h) Mitochondrial membrane potential in astrocytes derived from WT and *Atm*$^{-/-}$ cerebral cortices ($n = 3$-4 WT and 3-4 *Atm*$^{-/-}$ mice). The left part of each graph shows the fluorescent levels per cell and the right part shows the TMRE levels in microglia or astrocytes. Statistical analyses: two-tailed unpaired Student's *t*-test; ***$p < 0.005$

notion is supported by several studies (Floden & Combs, 2007; Yu et al., 2017) that have demonstrated that the proliferation rate of cultured microglial cells is highly dependent on GM-CSF, which was absent from our culture media. The DNA precursor EdU is widely used to assess cell proliferation; however, EdU can trigger DNA damage and can impair cell-cycle transitions and apoptosis (Zhao et al., 2013). The finding that EdU can trigger massive cell death in WT and *Atm*$^{-/-}$ cerebellar microglia suggest that these cells are highly sensitive to minor DNA damage triggered by low doses of this drug that do not affect astrocytes or cerebral cortical microglia (Figure S2a,b,d). Together, these results emphasize the differences between the microglial cells that originate from different brain areas. In the brain, microglia numbers are strictly maintained by the balance between cell proliferation and cell death (Askew et al., 2017). Lack of cell proliferation in the cultured microglia and increased cell death in *Atm*$^{-/-}$ cerebellar microglia are most likely the causes for the significantly reduced yield of the mutant microglia. We further assume that the higher yield of *Atm*$^{-/-}$ cerebral cortical microglial cell compared to cerebellar microglia cells stemmed from higher resistance to cell death by the cerebral cortical cells (Figure 2).

About 42% of the cultured WT cerebellar microglial cells had resting ramified or bipolar appearance. In WT cortical cultures and in *Atm*$^{-/-}$ cortical cultures of microglia, about half the cells were activated. In contrast, about 75% of cerebellar *Atm*$^{-/-}$ microglia in our purified cultures were in either amoeboid or unipolar morphologies characteristic of activated cells (Figure 4a–d). *In vivo* morphological analysis of *Atm*$^{-/-}$ mouse cerebella revealed that around 60% the microglia had shorter and thicker processes and larger cell bodies, signs of microglia activation (X. Song et al., 2019). Similar to the primary microglial cultures, our *in vivo* analyses revealed that Atm deficiency led to microglial activation (Figure 4e,f). Thus, similar to the *in vitro* conditions, Atm deficiency can lead to significant microglial activation in whole cerebellum. The divergence in functionality between microglia from the cerebella and cerebral cortex likely begins early in development. Our analyses were performed on cultures from P4 cerebella and cerebral cortices and differences were observed within two weeks after their dissociation. Our results suggest that microglial maturation occurs more rapidly in the cerebral cortex than in the cerebellum, and we propose that Atm deficiency specifically impairs cerebellar development leading to the accumulation of immature amoeboid cells. Together, these results strengthen the notion that the primary tissue cultures of purified microglia faithfully represent the effects of Atm deficiency on microglial cells.

Microglial cells survey the microenvironment and phagocytose cell debris, impaired synapses, and plaques. Lim et al. found that Atm binds to β-adaptin, one of the components of AP-2 adaptor complex, which is involved in clathrin-mediated endocytosis (Lim et al., 1998). Cerebellar, but not cerebral cortical, *Atm*$^{-/-}$ microglial cells were significantly impaired in their ability to phagocytose latex beads (Figure 8). This finding implies that under certain circumstances Atm plays an important role in cell membrane function. These functions require that microglial cells have high plasticity and motility. The reduced functionality of the cerebellar microglia led us to hypothesize that Atm deficiency in microglial cells would severely reduce their motility, but, surprisingly, our results showed the opposite: Atm deficiency accelerated motility of cerebellar microglia (Figure 6). Two main mechanisms may result in this phenomenon: First, we speculate that increased levels of ROS and reactive nitrogen species that we observed in *Atm*$^{-/-}$ cerebellar microglia compared to WT cells (Figure 7) accelerate microglial motility. It has been shown that elevated levels of these reactive species directly increase the steady-state levels of GTP-bound Rac1 protein thereby accelerating motility (Tolbert et al., 2019). Second, microglia in their resting state are not motile but rather actively survey their environment through their highly motile processes and protrusions (Nimmerjahn et al., 2005). Compared to wild type cerebellar microglia, a significantly higher percentage of *Atm*$^{-/-}$ cerebellar microglia are activated. The migration rate of resting microglia is lower than that of activated unipolar microglia (Lively & Schlichter, 2013). Thus, the high percentage of unipolar *Atm*$^{-/-}$ cerebellar microglia partially explains the accelerated motility of these cells.

We found a significant increase in ROS levels in *Atm*$^{-/-}$ cerebellar microglia relative to WT cells but not in cerebral cortical cells (Figure 7a). We previously found that oxidative stress plays a role in cellular degeneration in A-T (Kamsler et al., 2001). Our work is compatible with the previous report that provided evidence of a dramatic increase in heme oxygenase activity in *Atm*$^{-/-}$ cerebellum of mice that was strongly suggestive of increased oxidative stress (Barlow et al., 1999). In contrast to microglial cells, we found that cerebral cortical *Atm*$^{-/-}$ astrocytes had significant lower ROS levels compared to WT astrocytes. Since ROS level measurements were of untreated astrocytes, the reduction in ROS level can be explained due to increased levels of endogenous antioxidants (Poljsak, 2011). The mutant cells might have an improved defense machinery against ROS, which can greatly contribute in coping with oxidative environment in the absence of *Atm* (Figure 7b).

We found that levels of pro-BDNF, Akt, GAPDH, and actin were significantly reduced in *Atm*$^{-/-}$ cerebellar, but not cerebral cortical, microglial cells (Figure 9). Specific proteolytic cleavage of pro-BDNF yields the 14-kDa, mature form. We assume that the reduced pro-BDNF levels in *Atm*$^{-/-}$ cerebellar microglia in the early postnatal period result in reduced expression of mature BDNF in *Atm*$^{-/-}$ cerebellar microglial cells. Mature BDNF promotes cell survival, migration, and differentiation as well as dendritic arborization, synaptogenesis, and activity-dependent forms of synaptic plasticity (Gottlob et al., 2001). In contrast, the pro-BDNF causes cell death and pruning of non-active synapses (Je et al., 2012). Interestingly, we previously showed that Atm deficiency results in an increased number of synapses in neural cultures as well as in the mutant cerebellum (Kanner et al., 2018). BDNF secreted by microglia is critical in multiple learning tasks and in learning-induced synaptic remodeling (Parkhurst et al., 2013). Moreover, genetic depletion of BDNF from microglia recapitulates many of the phenotypes generated by deletion of microglia (Parkhurst et al., 2013). We speculate that in addition to Atm deficiency-induced cerebellar atrophy, reduced BNDF expression impairs cerebellar learning further augmenting cerebellar motor deficits in diseases like A-T.

Links between Akt and Atm have been documented. For instance, radiosensitivity, which is one of the classical hallmarks of A-T, is explained by the lack of Akt activity (W. S. Chen et al., 2001). The previously reported prolonged delay seen in the G2/M checkpoint following γ-radiation in *Atm*$^{-/-}$ cells may also result from altered Akt activity (B. Xu et al., 2002) as Akt plays a key role in controlling this transition after DNA damage (Kandel et al., 2002). It is possible that the lack of Atm prevents appropriate phosphorylation of Akt (Y. Li et al., 2012).

Atm deficiency in microglia also decreases expression of the housekeeping protein GAPDH, which is often used for normalization during western blot analyses. The multifunctional GAPDH is important in the glycolytic process and in apoptosis independently of its glycolytic functions (Berry & Boulton, 2000). GAPDH also has a protective role through inhibition of mitochondrial outer membrane permeabilization and cytochrome C release through mechanisms not dependent on caspase activation (Colell et al., 2007). GAPDH also protects cells from apoptosis through the elevation of glycolysis followed by enhancement of autophagy and transient reduction in mitochondrial mass (Colell et al., 2007). Combined reduction in the levels of Akt and GAPDH along with the elevation of the mitochondrial mass and the impaired mitochondrial membrane potential observed in the Atm-deficient microglia (Figure 11), might interrupt the regulation of processes necessary for cell survival, thus triggering various independent apoptotic pathways.

The cleaved form of the cytoskeleton protein actin influences microglial cell morphology (Franco-Bocanegra et al., 2019). Impaired actin dynamics can lead to reduced mitochondrial membrane potential and sensitivity to apoptotic insult, a mechanism conserved from yeast to mammals (Gourlay & Ayscough, 2005). Thus, morphology differences seen in *Atm*$^{-/-}$ compared with the wild type cerebellar microglia and the reduced mitochondrial membrane potential in the mutant might be due to loss of actin.

Our analysis also revealed a significant increase in mitochondrial mass in cerebellar *Atm*$^{-/-}$ microglia (Figure 11a). Additionally, using TMRE we found that cerebellar *Atm*$^{-/-}$ microglial cells exhibit reduced mitochondrial membrane potential suggesting that Atm deficiency reduces mitochondrial functionality (Figure 11b). Our results are compatible with the recent findings that mitochondrial activity and ATP production are abnormally low primary human skin fibroblast cell lines created from A-T patients (Chow et al., 2019). Changes in mitochondrial mass and membrane potential are observed in early stages of apoptosis (Mancini et al., 1997; Reipert et al., 1995). Atm is activated in response to oxidative stress specifically in the mitochondria in the absence of DNA damage (Ditch & Paull, 2012; Morita et al., 2014; Paull, 2015), suggesting that factors not related to DNA damage are involved in Atm activation (Lee & Paull, 2020). Valentin-Vega et al. showed that a fraction of Atm protein is localized in the mitochondria and that there is mitochondrial dysfunction and enhanced generation of ROS in *Atm*$^{-/-}$ thymocytes (Valentin-Vega et al., 2012). Changes in the membrane potential are presumed to occur in response to the opening of the mitochondrial permeability transition pore, which allows passage of ions and small molecules leading to the uncoupling of the respiratory chain and the release of cytochrome *C* into the cytosol where it activates cell death through activation of caspases (C. Wang & Youle, 2009).

We hypothesize that Atm function couples the mitochondrial respiratory chain and the generation of ATP. Atm deficiency likely induces generation of superoxide anions thereby accelerating the formation of oxygen radicals and resulting in oxidative stress. The idea that oxidative stress plays a role in the etiology of A-T was proposed by Rotman and Shiloh (Rotman & Shiloh, 1997a, 1997b) and validated by Kamsler et al. (Kamsler et al., 2001). Barlow et al. provided evidence of oxidative stress in in the cerebellum of Atm-deficient mice (Barlow et al., 1999). High levels of oxidative stress may underlie the diverse symptoms of A-T such as progressive neurodegeneration, immunodeficiency, and premature aging.

In summary, Atm deficiency severely impaired the functionality of cerebellar microglia. In culture, *Atm*$^{-/-}$ cerebellar microglia have impaired phagocytosis, accelerated cell migration, elevated levels of ROS, increased mitochondrial mass, and decreased membrane potential compared to wild-type cerebellar microglia. Loss of Atm did not result in dysfunction of cerebral cortical microglia, however. Our data support our working hypothesis that Atm inactivation reduces the protective effects of cerebellar glial cells but not of cerebral cortical glial cells leading to the cerebellar atrophy that is observed in A-T patients. It is still unclear whether the differences between cerebellar and cerebral microglia are innate, tissue specific, or stem from differences in responses to alterations in signaling resulting from Atm deficiency. Our analyses accentuate the critical role played by regional microglial cells in the etiology of A-T. Under the conditions of Atm deficiency, the cerebellar but not the cortical microglial cells become destructive thereby contributing to cerebellar pathology.

ACKNOWLEDGMENTS

The laboratory of AB is funded by the Israel Science Foundation (Grants Nos. 41/15 and 1307/19), Israeli Ministry of Science and Technology (Grant No. 3-14260-2016) German Israeli Foundation (Grant No. I-192-418.13-2014), and Joint Italian-Israeli Laboratory on Application of Neuroscience (Grant No. 590308).

CONFLICT OF INTEREST

The authors declare no conflict of interest.

AUTHOR CONTRIBUTIONS

All authors listed have made substantial, direct, and intellectual contributions to the work and approved it for publication.

DATA AVAILABILITY STATEMENT

Data sharing is not applicable to this article as no new data were created or analyzed in this study.

ORCID

Ari Barzilai https://orcid.org/0000-0002-8133-463X

REFERENCES

Abbas, T., Keaton, M. A., & Dutta, A. (2013). Genomic instability in cancer. *Cold Spring Harbor Perspectives in Biology*, *5*(3), a012914. https://doi.org/10.1101/cshperspect.a012914

Aguilera, A., & Garcia-Muse, T. (2013). Causes of Genome Instability. *Annual Review of Genetics*, *47*, 1–32. https://doi.org/10.1146/annurev-genet-111212-133232

Aloisi, F. (2001). Immune function of microglia. *GLIA*, *36*(2), 165–179.

Alt, F. W., Zhang, Y., Meng, F. L., Guo, C., & Schwer, B. (2013). Mechanisms of programmed DNA lesions and genomic instability in the immune system. *Cell*, *152*(3), 417–429. https://doi.org/10.1016/j.cell.2013.01.007

Alterman, N., Fattal-Valevski, A., Moyal, L., Crawford, T. O., Lederman, H. M., Ziv, Y., & Shiloh, Y. (2007). Ataxia-telangiectasia: Mild neurological presentation despite null ATM mutation and severe cellular phenotype. *American Journal of Medical Genetics: Part A*, *143A*(16), 1827–1834. https://doi.org/10.1002/ajmg.a.31853

Ambrose, M., & Gatti, R. A. (2013). Pathogenesis of ataxia-telangiectasia: The next generation of ATM functions. *Blood*, *121*(20), 4036–4045. https://doi.org/10.1182/blood-2012-09-456897

Askew, K., Li, K., Olmos-Alonso, A., Garcia-Moreno, F., Liang, Y., Richardson, P., Tipton, T., Chapman, M. A., Riecken, K., Beccari, S., Sierra, A., Molnar, Z., Cragg, M. S., Garaschuk, O., Perry, V. H., & Gomez-Nicola, D. (2017). Coupled proliferation and apoptosis maintain the rapid turnover of microglia in the adult brain. *Cell Reports*, *18*(2), 391–405. https://doi.org/10.1016/j.celrep.2016.12.041

Bakkenist, C. J., & Kastan, M. B. (2003). DNA damage activates ATM through intermolecular autophosphorylation and dimer dissociation. *Nature*, *421*(6922), 499–506.

Barlow, C., Dennery, P. A., Shigenaga, M. K., Smith, M. A., Morrow, J. D., Roberts, L. J., 2nd, … Levine, R. L. (1999). Loss of the ataxia-telangiectasia gene product causes oxidative damage in target organs. *Proceedings of the National Academy of Sciences of the United States of America*, *96*(17), 9915–9919.

Barlow, C., Hirotsune, S., Paylor, R., Liyanage, M., Eckhaus, M., Collins, F., … Wynshaw-Boris, A. (1996). Atm-deficient mice: A paradigm of ataxia telangiectasia. *Cell*, *86*(1), 159–171.

Bensimon, A., Aebersold, R., & Shiloh, Y. (2011). Beyond ATM: The protein kinase landscape of the DNA damage response. *FEBS Letters*, *585*(11), 1625–1639. https://doi.org/10.1016/j.febslet.2011.05.013

Bensimon, A., Schmidt, A., Ziv, Y., Elkon, R., Wang, S. Y., Chen, D. J., … Shiloh, Y. (2010). ATM-dependent and -independent dynamics of the nuclear phosphoproteome after DNA damage. *Science Signaling*, *3*(151), rs3. https://doi.org/10.1126/scisignal.2001034

Berridge, M. V., & Tan, A. S. (1993). Characterization of the cellular reduction of 3-(4,5-dimethylthiazol-2-yl)-2,5-diphenyltetrazolium bromide (MTT): Subcellular localization, substrate dependence, and involvement of mitochondrial electron transport in MTT reduction. *Archives of Biochemistry and Biophysics*, *303*(2), 474–482. https://doi.org/10.1006/abbi.1993.1311

Berry, M. D., & Boulton, A. A. (2000). Glyceraldehyde-3-phosphate dehydrogenase and apoptosis. *The Journal of Neuroscience Research*, *60*(2), 150–154. https://doi.org/10.1002/(SICI)1097-4547(20000415)60:2<150::AID-JNR3>3.0.CO;2-4

Bhatti, S., Kozlov, S., Farooqi, A. A., Naqi, A., Lavin, M., & Khanna, K. K. (2011). ATM protein kinase: The linchpin of cellular defenses to stress.

Cellular and Molecular Life Sciences, *68*(18), 2977–3006. https://doi.org/10.1007/s00018-011-0683-9

Biton, S., Barzilai, A., & Shiloh, Y. (2008). The neurological phenotype of ataxia-telangiectasia: Solving a persistent puzzle. *DNA Repair (Amst)*, *7*(7), 1028–1038. https://doi.org/10.1016/j.dnarep.2008.03.006

Borde, V., & de Massy, B. (2013). Programmed induction of DNA double strand breaks during meiosis: Setting up communication between DNA and the chromosome structure. *Current Opinion in Genetics & Development*, *23*(2), 147–155. https://doi.org/10.1016/j.gde.2012.12.002

Brown, G. C., & Neher, J. J. (2014). Microglial phagocytosis of live neurons. *Nature Reviews. Neuroscience*, *15*(4), 209–216. https://doi.org/10.1038/nrn3710

Bushong, E. A., Martone, M. E., & Ellisman, M. H. (2004). Maturation of astrocyte morphology and the establishment of astrocyte domains during postnatal hippocampal development. *International Journal of Developmental Neuroscience*, *22*(2), 73–86. https://doi.org/10.1016/j.ijdevneu.2003.12.008

Cadet, J., & Wagner, J. R. (2013). DNA base damage by reactive oxygen species, oxidizing agents, and UV radiation. *Cold Spring Harbor Perspectives in Biology*, *29*(3-4), 222–230. https://doi.org/10.1101/cshperspect.a012559

Camilleri-Broet, S., Vanderwerff, H., Caldwell, E., & Hockenbery, D. (1998). Distinct alterations in mitochondrial mass and function characterize different models of apoptosis. *Experimental Cell Research*, *239*(2), 277–292. https://doi.org/10.1006/excr.1997.3899

Chen, B. P., Li, M., & Asaithamby, A. (2012). New insights into the roles of ATM and DNA-PKcs in the cellular response to oxidative stress. *Cancer Letters*, *327*(1-2), 103–110. https://doi.org/10.1016/j.canlet.2011.12.004

Chen, W. S., Xu, P. Z., Gottlob, K., Chen, M. L., Sokol, K., Shiyanova, T., … Hay, N. (2001). Growth retardation and increased apoptosis in mice with homozygous disruption of the Akt1 gene. *Genes & Development*, *15*(17), 2203–2208. https://doi.org/10.1101/gad.913901

Chow, H. M., Cheng, A., Song, X., Swerdel, M. R., Hart, R. P., & Herrup, K. (2019). ATM is activated by ATP depletion and modulates mitochondrial function through NRF1. *The Journal of Cell Biology*, *218*(3), 909–928. https://doi.org/10.1083/jcb.201806197

Ciccia, A., & Elledge, S. J. (2010). The DNA damage response: Making it safe to play with knives. *Molecular Cell*, *40*(2), 179–204. https://doi.org/10.1016/j.molcel.2010.09.019

Claes, K., Depuydt, J., Taylor, A. M., Last, J. I., Baert, A., Schietecatte, P., … Vral, A. (2013). Variant ataxia telangiectasia: Clinical and molecular findings and evaluation of radiosensitive phenotypes in a patient and relatives. *Neuromolecular Medicine*, *15*(3), 447–457. https://doi.org/10.1007/s12017-013-8231-4

Colell, A., Ricci, J. E., Tait, S., Milasta, S., Maurer, U., Bouchier-Hayes, L., … Green, D. R. (2007). GAPDH and autophagy preserve survival after apoptotic cytochrome c release in the absence of caspase activation. *Cell*, *129*(5), 983–997. https://doi.org/10.1016/j.cell.2007.03.045

Coull, J. A., Beggs, S., Boudreau, D., Boivin, D., Tsuda, M., Inoue, K., … De Koninck, Y. (2005). BDNF from microglia causes the shift in neuronal anion gradient underlying neuropathic pain. *Nature*, *438*(7070), 1017–1021. https://doi.org/10.1038/nature04223

Cremona, C. A., & Behrens, A. (2014). ATM signalling and cancer. *Oncogene*, *33*(26), 3351–3360. https://doi.org/10.1038/onc.2013.275

Crouch, J. D., & Brosh, R. M., Jr. (2016). Mechanistic and biological considerations of oxidatively damaged DNA for helicase-dependent pathways of nucleic acid metabolism. *Free Radical Biology & Medicine*, *107*, 245–257. https://doi.org/10.1016/j.freeradbiomed.2016.11.022

Cullheim, S., & Thams, S. (2007). The microglial networks of the brain and their role in neuronal network plasticity after lesion. *Brain Research Reviews*, *55*(1), 89–96. https://doi.org/10.1016/j.brainresrev.2007.03.012

Davis, B. M., Salinas-Navarro, M., Cordeiro, M. F., Moons, L., & De Groef, L. (2017). Characterizing microglia activation: A spatial statistics approach to maximize information extraction. *Scientific Reports*, *7*(1), 1576. https://doi.org/10.1038/s41598-017-01747-8

de Haas, A. H., Boddeke, H. W., & Biber, K. (2008). Region-specific expression of immunoregulatory proteins on microglia in the healthy CNS. *GLIA*, *56*(8), 888–894. https://doi.org/10.1002/glia.20663

de la Rosa, E. J., & de Pablo, F. (2000). Cell death in early neural development: Beyond the neurotrophic theory. *Trends in Neurosciences*, *23*(10), 454–458.

Ditch, S., & Paull, T. T. (2012). The ATM protein kinase and cellular redox signaling: Beyond the DNA damage response. *Trends in Biochemical Sciences*, *37*(1), 15–22. https://doi.org/10.1016/j.tibs.2011.10.002

Eaton, J. S., Lin, Z. P., Sartorelli, A. C., Bonawitz, N. D., & Shadel, G. S. (2007). Ataxia-telangiectasia mutated kinase regulates ribonucleotide reductase and mitochondrial homeostasis. *The Journal of Clinical Investigation*, *117*(9), 2723–2734. https://doi.org/10.1172/JCI31604

Elson, A., Wang, Y., Daugherty, C. J., Morton, C. C., Zhou, F., Campos-Torres, J., & Leder, P. (1996). Pleiotropic defects in ataxia-telangiectasia protein-deficient mice. *Proceedings of the National Academy of Sciences of the United States of America*, *93*(23), 13084–13089.

Errico, A., & Costanzo, V. (2012). Mechanisms of replication fork protection: A safeguard for genome stability. *Critical Reviews in Biochemistry and Molecular Biology*, *47*(3), 222–235. https://doi.org/10.3109/10409238.2012.655374

Escartin, C., Galea, E., Lakatos, A., O'Callaghan, J. P., Petzold, G. C., Serrano-Pozo, A., … Verkhratsky, A. (2021). Reactive astrocyte nomenclature, definitions, and future directions. *Nature Neuroscience*, *24*(3), 312–325. https://doi.org/10.1038/s41593-020-00783-4

Floden, A. M., & Combs, C. K. (2007). Microglia repetitively isolated from in vitro mixed glial cultures retain their initial phenotype. *Journal of Neuroscience Methods*, *164*(2), 218–224. https://doi.org/10.1016/j.jneumeth.2007.04.018

Franco-Bocanegra, D. K., McAuley, C., Nicoll, J. A. R., & Boche, D. (2019). Molecular mechanisms of microglial motility: Changes in ageing and Alzheimer's disease. *Cells*, *639*, 1–21. https://doi.org/10.3390/cells8060639

Fu, Z., Zou, F., Deng, H., Zhou, H., & Liu, L. (2014). Estrogen protects SGC7901 cells from endoplasmic reticulum stress-induced apoptosis by the Akt pathway. *Oncology Letters*, *7*(2), 560–564. https://doi.org/10.3892/ol.2013.1701

Gatti, R. A., Becker-Catania, S., Chun, H. H., Sun, X., Mitui, M., Lai, C. H., … Iyer, R. K. (2001). The pathogenesis of ataxia-telangiectasia. Learning from a Rosetta Stone. *Clinical Reviews in Allergy and Immunology*, *20*(1), 87–108. https://doi.org/10.1385/CRIAI:20:1:87

Gerencser, A. A., Chinopoulos, C., Birket, M. J., Jastroch, M., Vitelli, C., Nicholls, D. G., & Brand, M. D. (2012). Quantitative measurement of mitochondrial membrane potential in cultured cells: Calcium-induced de- and hyperpolarization of neuronal mitochondria. *The Journal of Physiology*, *590*(12), 2845–2871. https://doi.org/10.1113/jphysiol.2012.228387

Gilad, S., Chessa, L., Khosravi, R., Russell, P., Galanty, Y., Piane, M., … Bar-Shira, A. (1998). Genotype-phenotype relationships in ataxia-telangiectasia and variants. *American Journal of Human Genetics*, *62*(3), 551–561.

Gilad, S., Khosravi, R., Shkedy, D., Uziel, T., Ziv, Y., Savitsky, K., … Bar-Shira, A. (1996). Predominance of null mutations in ataxia-telangiectasia. *Human Molecular Genetics*, *5*(4), 433–439.

Ginhoux, F., Greter, M., Leboeuf, M., Nandi, S., See, P., Gokhan, S., … Merad, M. (2010). Fate mapping analysis reveals that adult microglia derive from primitive macrophages. *Science*, *330*(6005), 841–845. https://doi.org/10.1126/science.1194637

Giulian, D., & Baker, T. J. (1986). Characterization of ameboid microglia isolated from developing mammalian brain. *The Journal of Neuroscience*, *6*(8), 2163–2178.

Goldshmit, Y., Erlich, S., & Pinkas-Kramarski, R. (2001). Neuregulin rescues PC12-ErbB4 cells from cell death induced by H(2)O(2). Regulation of reactive oxygen species levels by phosphatidylinositol 3-kinase. *The Journal of Biological Chemistry*, *276*(49), 46379–46385. https://doi.org/10.1074/jbc.M105637200

Goodarzi, A. A., & Jeggo, P. A. (2013). The repair and signaling responses to DNA double-strand breaks. *Advances in Genetics*, *82*, 1–45. https://doi.org/10.1016/B978-0-12-407676-1.00001-9

Gottlob, K., Majewski, N., Kennedy, S., Kandel, E., Robey, R. B., & Hay, N. (2001). Inhibition of early apoptotic events by Akt/PKB is dependent on the first committed step of glycolysis and mitochondrial hexokinase. *Genes & Development*, *15*(11), 1406–1418. https://doi.org/10.1101/gad.889901

Gourlay, C. W., & Ayscough, K. R. (2005). The actin cytoskeleton in ageing and apoptosis. *FEMS Yeast Research*, *5*(12), 1193–1198. https://doi.org/10.1016/j.femsyr.2005.08.001

Grabert, K., Michoel, T., Karavolos, M. H., Clohisey, S., Baillie, J. K., Stevens, M. P., … McColl, B. W. (2016). Microglial brain region-dependent diversity and selective regional sensitivities to aging. *Nature Neuroscience*, *19*(3), 504–516. https://doi.org/10.1038/nn.4222

Guo, Z., Kozlov, S., Lavin, M. F., Person, M. D., & Paull, T. T. (2010). ATM activation by oxidative stress. *Science*, *330*(6003), 517–521. https://doi.org/10.1126/science.1192912

Halaby, M. J., Hibma, J. C., He, J., & Yang, D. Q. (2008). ATM protein kinase mediates full activation of Akt and regulates glucose transporter 4 translocation by insulin in muscle cells. *Cellular Signalling*, *20*(8), 1555–1563. https://doi.org/10.1016/j.cellsig.2008.04.011

Hande, M. P., Balajee, A. S., Tchirkov, A., Wynshaw-Boris, A., & Lansdorp, P. M. (2001). Extra-chromosomal telomeric DNA in cells from Atm(-/-) mice and patients with ataxia-telangiectasia. *Human Molecular Genetics*, *10*(5), 519–528.

Hempstead, B. L. (2015). Brain-derived neurotrophic factor: Three ligands, many actions. *Transactions of the American Clinical Climatology Association*, *126*, 9–19.

Herculano-Houzel, S. (2014). The glia/neuron ratio: How it varies uniformly across brain structures and species and what that means for brain physiology and evolution. *GLIA*, *62*(9), 1377–1391. https://doi.org/10.1002/glia.22683

Herrup, K. (2013). ATM and the epigenetics of the neuronal genome. *Mechanisms of Ageing and Development*, *134*(10), 434–439. https://doi.org/10.1016/j.mad.2013.05.005

Herrup, K., Li, J., & Chen, J. (2013). The role of ATM and DNA damage in neurons: Upstream and downstream connections. *DNA Repair (Amst)*, *12*(8), 600–604. https://doi.org/10.1016/j.dnarep.2013.04.012

Hoche, F., Seidel, K., Theis, M., Vlaho, S., Schubert, R., Zielen, S., & Kieslich, M. (2012). Neurodegeneration in ataxia telangiectasia: What is new? What is evident? *Neuropediatrics*, *43*(3), 119–129. https://doi.org/10.1055/s-0032-1313915

Hoft, S., Griemsmann, S., Seifert, G., & Steinhauser, C. (2014). Heterogeneity in expression of functional ionotropic glutamate and GABA receptors in astrocytes across brain regions: Insights from the thalamus. *Philosophy Transductions of the Royal Society London B Biological Sciences*, *369*(1654), 20130602. https://doi.org/10.1098/rstb.2013.0602

Huttemann, M., Pecina, P., Rainbolt, M., Sanderson, T. H., Kagan, V. E., Samavati, L., … Lee, I. (2011). The multiple functions of cytochrome c and their regulation in life and death decisions of the mammalian cell: From respiration to apoptosis. *Mitochondrion*, *11*(3), 369–381. https://doi.org/10.1016/j.mito.2011.01.010

Je, H. S., Yang, F., Ji, Y., Nagappan, G., Hempstead, B. L., & Lu, B. (2012). Role of pro-brain-derived neurotrophic factor (proBDNF) to mature BDNF conversion in activity-dependent competition at developing neuromuscular synapses. *Proceedings of the National Academy of Sciences of the United States of America*, *109*(39), 15924–15929. https://doi.org/10.1073/pnas.1207767109

Jena, N. R. (2012). DNA damage by reactive species: Mechanisms, mutation and repair. *Journal of Biosciences*, *37*(3), 503–517.

Jeppesen, D. K., Bohr, V. A., & Stevnsner, T. (2011). DNA repair deficiency in neurodegeneration. *Progress in Neurobiology*, *94*(2), 166–200. https://doi.org/10.1016/j.pneurobio.2011.04.013

John Lin, C. C., Yu, K., Hatcher, A., Huang, T. W., Lee, H. K., Carlson, J., … Deneen, B. (2017). Identification of diverse astrocyte populations and their malignant analogs. *Nature Neuroscience*, *20*(3), 396–405. https://doi.org/10.1038/nn.4493

Jurga, A. M., Paleczna, M., & Kuter, K. Z. (2020). Overview of General and Discriminating Markers of Differential Microglia Phenotypes. *Frontiers in Cellular Neuroscience*, *14*, 198. https://doi.org/10.3389/fncel.2020.00198

Kaidi, A., & Jackson, S. P. (2013). KAT5 tyrosine phosphorylation couples chromatin sensing to ATM signalling. *Nature*, *498*(7452), 70–74. https://doi.org/10.1038/nature12201

Kamsler, A., Daily, D., Hochman, A., Stern, N., Shiloh, Y., Rotman, G., & Barzilai, A. (2001). Increased oxidative stress in ataxia telangiectasia evidenced by alterations in redox state of brains from Atm-deficient mice. *Cancer Research*, *61*(5), 1849–1854.

Kandel, E. S., Skeen, J., Majewski, N., Di Cristofano, A., Pandolfi, P. P., Feliciano, C. S., … Hay, N. (2002). Activation of Akt/protein kinase B overcomes a G(2)/m cell cycle checkpoint induced by DNA damage. *Molecular and Cellular Biology*, *22*(22), 7831–7841.

Kanner, S., Goldin, M., Galron, R., Ben Jacob, E., Bonifazi, P., & Barzilai, A. (2018). Astrocytes restore connectivity and synchronization in dysfunctional cerebellar networks. *Proceedings of the National Academy of Sciences of the United States of America*, *115*(31), 8025–8030. https://doi.org/10.1073/pnas.1718582115

Khalil, A., Morgan, R. N., Adams, B. R., Golding, S. E., Dever, S. M., Rosenberg, E., … Valerie, K. (2011). ATM-dependent ERK signaling via AKT in response to DNA double-strand breaks. *Cell Cycle*, *10*(3), 481–491. https://doi.org/10.4161/cc.10.3.14713

Kierdorf, K., Erny, D., Goldmann, T., Sander, V., Schulz, C., Perdiguero, E. G., … Prinz, M. (2013). Microglia emerge from erythromyeloid precursors via Pu.1- and Irf8-dependent pathways. *Nature Neuroscience*, *16*(3), 273–280. https://doi.org/10.1038/nn.3318

Kim, Y. S., & Joh, T. H. (2006). Microglia, major player in the brain inflammation: Their roles in the pathogenesis of Parkinson's disease. *Experimental & Molecular Medicine*, *38*(4), 333–347. https://doi.org/10.1038/emm.2006.40

Kong, X., Shen, Y., Jiang, N., Fei, X., & Mi, J. (2011). Emerging roles of DNA-PK besides DNA repair. *Cellular Signalling*, *23*(8), 1273–1280. https://doi.org/10.1016/j.cellsig.2011.04.005

Kornberg, M. D., Sen, N., Hara, M. R., Juluri, K. R., Nguyen, J. V., Snowman, A. M., … Snyder, S. H. (2010). GAPDH mediates nitrosylation of nuclear proteins. *Nature Cell Biology*, *12*(11), 1094–1100. https://doi.org/10.1038/ncb2114

Kozlov, S. V., Graham, M. E., Peng, C., Chen, P., Robinson, P. J., & Lavin, M. F. (2006). Involvement of novel autophosphorylation sites in ATM activation. *The EMBO Journal*, *25*(15), 3504–3514.

Lange, J., Pan, J., Cole, F., Thelen, M. P., Jasin, M., & Keeney, S. (2011). ATM controls meiotic double-strand-break formation. *Nature*, *479*(7372), 237–240. https://doi.org/10.1038/nature10508

Lavin, M. F. (2008). Ataxia-telangiectasia: From a rare disorder to a paradigm for cell signalling and cancer. *Nature Reviews in Molecular Cell Biology*, *9*(10), 759–769. https://doi.org/10.1038/nrm2514

Lawson, L. J., Perry, V. H., Dri, P., & Gordon, S. (1990). Heterogeneity in the distribution and morphology of microglia in the normal adult mouse brain. *Neuroscience*, *39*(1), 151–170. https://doi.org/10.1016/0306-4522(90)90229-w

Lee, J. H., & Paull, T. T. (2020). Mitochondria at the crossroads of ATM-mediated stress signaling and regulation of reactive oxygen species. *Redox Biology*, *32*, 101511. https://doi.org/10.1016/j.redox.2020.101511

Li, Q., Cheng, Z., Zhou, L., Darmanis, S., Neff, N. F., Okamoto, J., … Barres, B. A. (2019). Developmental Heterogeneity of Microglia and Brain Myeloid Cells Revealed by Deep Single-Cell RNA Sequencing. *Neuron*, *101*(2), 207–223-e210. https://doi.org/10.1016/j.neuron.2018.12.006

Li, Y., Xiong, H., & Yang, D. Q. (2012). Functional switching of ATM: Sensor of DNA damage in proliferating cells and mediator of Akt survival signal in post-mitotic human neuron-like cells. *Chinese Journal of Cancer*, *31*(8), 364–372. https://doi.org/10.5732/cjc.012.10086

Lian, H., Litvinchuk, A., Chiang, A. C., Aithmitti, N., Jankowsky, J. L., & Zheng, H. (2016). Astrocyte-Microglia cross talk through complement activation modulates amyloid pathology in mouse models of Alzheimer's Disease. *The Journal of Neuroscience*, *36*(2), 577–589. https://doi.org/10.1523/JNEUROSCI.2117-15.2016

Liddelow, S. A., & Barres, B. A. (2017). Reactive astrocytes: Production, function, and therapeutic potential. *Immunity*, *46*(6), 957–967. https://doi.org/10.1016/j.immuni.2017.06.006

Liddelow, S. A., Guttenplan, K. A., Clarke, L. E., Bennett, F. C., Bohlen, C. J., Schirmer, L., … Barres, B. A. (2017). Neurotoxic reactive astrocytes are induced by activated microglia. *Nature*, *541*(7638), 481–487. https://doi.org/10.1038/nature21029

Lim, D. S., Kirsch, D. G., Canman, C. E., Ahn, J. H., Ziv, Y., Newman, L. S., … Kastan, M. B. (1998). ATM binds to beta-adaptin in cytoplasmic vesicles. *Proceedings of the National Academy of Sciences of the United States of America*, *95*(17), 10146–10151.

Lindahl, T. (1993). Instability and decay of the primary structure of DNA. *Nature*, *362*(6422), 709–715. https://doi.org/10.1038/362709a0

Ling, E. A., & Tan, C. K. (1974). Amoeboid microglial cells in the corpus callosum of neonatal rats. *Archivum Histologicum Japonicum*, *36*(4), 265–280. https://doi.org/10.1679/aohc1950.36.265

Lively, S., & Schlichter, L. C. (2013). The microglial activation state regulates migration and roles of matrix-dissolving enzymes for invasion. *Journal of Neuroinflammation*, *10*, 75. https://doi.org/10.1186/1742-2094-10-75

Lovejoy, C. A., & Cortez, D. (2009). Common mechanisms of PIKK regulation. *DNA Repair (Amst)*, *8*(9), 1004–1008. https://doi.org/10.1016/j.dnarep.2009.04.006

Mancini, M., Anderson, B. O., Caldwell, E., Sedghinasab, M., Paty, P. B., & Hockenbery, D. M. (1997). Mitochondrial proliferation and paradoxical membrane depolarization during terminal differentiation and apoptosis in a human colon carcinoma cell line. *The Journal of Cell Biology*, *138*(2), 449–469.

Manto, M. U., & Jissendi, P. (2012). Cerebellum: Links between development, developmental disorders and motor learning. *Frontiers in Neuroanatomy*, *6*, 1. https://doi.org/10.3389/fnana.2012.00001

Marechal, A., & Zou, L. (2013). DNA damage sensing by the ATM and ATR kinases. *Cold Spring Harbor Perspectives in Biology*, *5*(9), 1–17. https://doi.org/10.1101/cshperspect.a012716

Marin-Teva, J. L., Dusart, I., Colin, C., Gervais, A., van Rooijen, N., & Mallat, M. (2004). Microglia promote the death of developing Purkinje cells. *Neuron*, *41*(4), 535–547.

Matsuoka, S., Ballif, B. A., Smogorzewska, A., McDonald, E. R., 3rd, Hurov, K. E., Luo, J., … Elledge, S. J. (2007). ATM and ATR substrate analysis reveals extensive protein networks responsive to DNA damage. *Science*, *316*(5828), 1160–1166. https://doi.org/10.1126/science.1140321

McGeer, P. L., Rogers, J., & McGeer, E. G. (2006). Inflammation, anti-inflammatory agents and Alzheimer disease: The last 12 years. *Journal of Alzheimer's Disease*, *9*(3 Suppl), 271–276.

McKinnon, P. J. (2012). ATM and the molecular pathogenesis of ataxia telangiectasia. *Annual Review of Pathology*, *7*, 303–321. https://doi.org/10.1146/annurev-pathol-011811-132509

McKinnon, P. J. (2013). Maintaining genome stability in the nervous system. *Nature Neuroscience*, *16*(11), 1523–1529. https://doi.org/10.1038/nn.3537

Meneret, A., Ahmar-Beaugendre, Y., Rieunier, G., Mahlaoui, N., Gaymard, B., Apartis, E., … Anheim, M. (2014). The pleiotropic movement disorders phenotype of adult ataxia-telangiectasia. *Neurology*, *83*(12), 1087–1095. https://doi.org/10.1212/WNL.0000000000000794

Menzel, F., Kaiser, N., Haehnel, S., Rapp, F., Patties, I., Schoneberg, N., … Bechmann, I. (2018). Impact of X-irradiation on microglia. *GLIA*, *66*(1), 15–33. https://doi.org/10.1002/glia.23239

Mergia, E., Russwurm, M., Zoidl, G., & Koesling, D. (2003). Major occurrence of the new alpha2beta1 isoform of NO-sensitive guanylyl cyclase in brain. *Cellular Signalling*, *15*(2), 189–195.

Metcalfe, J. A., Parkhill, J., Campbell, L., Stacey, M., Biggs, P., Byrd, P. J., & Taylor, A. M. (1996). Accelerated telomere shortening in ataxia telangiectasia. *Nature Genetics*, *13*(3), 350–353. https://doi.org/10.1038/ng0796-350

Miller, S. J. (2018). Astrocyte Heterogeneity in the adult central nervous system. *Frontiers in Cellular Neuroscience*, *12*, 401. https://doi.org/10.3389/fncel.2018.00401

Morita, A., Tanimoto, K., Murakami, T., Morinaga, T., & Hosoi, Y. (2014). Mitochondria are required for ATM activation by extranuclear oxidative stress in cultured human hepatoblastoma cell line Hep G2 cells. *Biochemical and Biophysical Research Communications*, *443*(4), 1286–1290. https://doi.org/10.1016/j.bbrc.2013.12.139

Morris, G. P., Clark, I. A., Zinn, R., & Vissel, B. (2013). Microglia: A new frontier for synaptic plasticity, learning and memory, and neurodegenerative disease research. *Neurobiology of Learning and Memory*, *105*, 40–53. https://doi.org/10.1016/j.nlm.2013.07.002

Mu, J. J., Wang, Y., Luo, H., Leng, M., Zhang, J., Yang, T., … Qin, J. (2007). A proteomic analysis of ataxia telangiectasia-mutated (ATM)/ATM-Rad3-related (ATR) substrates identifies the ubiquitin-proteasome system as a regulator for DNA damage checkpoints. *The Journal of Biological Chemistry*, *282*(24), 17330–17334. https://doi.org/10.1074/jbc.C700079200

Nakajima, H., Itakura, M., Kubo, T., Kaneshige, A., Harada, N., Izawa, T., … Takeuchi, T. (2017). Glyceraldehyde-3-phosphate dehydrogenase (GAPDH) aggregation causes mitochondrial dysfunction during oxidative stress-induced cell death. *The Journal of Biological Chemistry*, *292*(11), 4727–4742. https://doi.org/10.1074/jbc.M116.759084

Nakamura, K., Fike, F., Haghayegh, S., Saunders-Pullman, R., Dawson, A. J., Dork, T., & Gatti, R. A. (2014). A-TWinnipeg: Pathogenesis of rare ATM missense mutation c.6200C>A with decreased protein expression and downstream signaling, early-onset dystonia, cancer, and life-threatening radiotoxicity. *Mol Genet*. *Molecular Genetics Genomic Medicine*, *2*(4), 332–340. https://doi.org/10.1002/mgg3.72

Napoli, I., & Neumann, H. (2009). Microglial clearance function in health and disease. *Neuroscience*, *158*(3), 1030–1038. https://doi.org/10.1016/j.neuroscience.2008.06.046

Negrini, S., Gorgoulis, V. G., & Halazonetis, T. D. (2010). Genomic instability—An evolving hallmark of cancer. *Nature Reviews. Molecular Cell Biology*, *11*(3), 220–228. https://doi.org/10.1038/nrm2858

Neumann, H., Kotter, M. R., & Franklin, R. J. (2009). Debris clearance by microglia: An essential link between degeneration and regeneration. *Brain*, *132*(Pt 2), 288–295. https://doi.org/10.1093/brain/awn109

Nimmerjahn, A., Kirchhoff, F., & Helmchen, F. (2005). Resting microglial cells are highly dynamic surveillants of brain parenchyma in vivo. *Science*, *308*(5726), 1314–1318. https://doi.org/10.1126/science.1110647

O'Driscoll, M. (2012). Diseases associated with defective responses to DNA damage. *Cold Spring Harbor Perspectives in Biology*, *4*(12), 1–25. https://doi.org/10.1101/cshperspect.a012773

Ohtaki, H., Tsumuraya, T., Song, D., Sato, A., Ohara, K., Miyamoto, K., … Shioda, S. (2013). Establishment and characterization of primary adult microglial culture in mice. *Acta Neurochirurgica. Supplement*, *118*, 49–54. https://doi.org/10.1007/978-3-7091-1434-6_8

Pandita, T. K. (2002). ATM function and telomere stability. *Oncogene*, *21*(4), 611–618. https://doi.org/10.1038/sj.onc.1205060

Panier, S., & Durocher, D. (2013). Push back to respond better: Regulatory inhibition of the DNA double-strand break response. *Nature Reviews. Cancer*, *13*(10), 661–672. https://doi.org/10.1038/nrm3659

Parkhurst, C. N., Yang, G., Ninan, I., Savas, J. N., Yates, J. R., 3rd, Lafaille, J. J., … Gan, W. B. (2013). Microglia promote learning-dependent synapse formation through brain-derived neurotrophic factor. *Cell*, *155*(7), 1596–1609. https://doi.org/10.1016/j.cell.2013.11.030

Paull, T. T. (2015). Mechanisms of ATM Activation. *Annual Review of Biochemistry*, *84*, 711–738. https://doi.org/10.1146/annurev-biochem-060614-034335

Perlman, S. L., Boder Deceased, E., Sedgewick, R. P., & Gatti, R. A. (2012). Ataxia-telangiectasia. *Handbook of Clinical Neurology*, *103*, 307–332. https://doi.org/10.1016/B978-0-444-51892-7.00019-X

Perry, V. H., Nicoll, J. A., & Holmes, C. (2010). Microglia in neurodegenerative disease. *Nature Reviews. Neurology*, *6*(4), 193–201. https://doi.org/10.1038/nrneurol.2010.17

Poljsak, B. (2011). Strategies for reducing or preventing the generation of oxidative stress. *Oxidative Medicine and Cellular Longevity*, *2011*, 194586. https://doi.org/10.1155/2011/194586

Polo, S. E., & Jackson, S. P. (2011). Dynamics of DNA damage response proteins at DNA breaks: A focus on protein modifications. *Genes & Development*, *25*(5), 409–433. https://doi.org/10.1101/gad.2021311

Quek, H., Luff, J., Cheung, K., Kozlov, S., Gatei, M., Lee, C. S., … Lavin, M. F. (2017a). A rat model of ataxia-telangiectasia: Evidence for a neurodegenerative phenotype. *Human Molecular Genetics*, *26*(1), 109–123. https://doi.org/10.1093/hmg/ddw371

Quek, H., Luff, J., Cheung, K., Kozlov, S., Gatei, M., Lee, C. S., … Lavin, M. F. (2017b). Rats with a missense mutation in Atm display neuroinflammation and neurodegeneration subsequent to accumulation of cytosolic DNA following unrepaired DNA damage. *Journal of Leukocyte Biology*, *101*(4), 927–947. https://doi.org/10.1189/jlb.4VMA0716-316R

Ransohoff, R. M., & Cardona, A. E. (2010). The myeloid cells of the central nervous system parenchyma. *Nature*, *468*(7321), 253–262. https://doi.org/10.1038/nature09615

Rao, V. L., Audet, R. M., & Butterworth, R. F. (1997). Increased neuronal nitric oxide synthase expression in brain following portacaval anastomosis. *Brain Research*, *765*(1), 169–172.

Reipert, S., Berry, J., Hughes, M. F., Hickman, J. A., & Allen, T. D. (1995). Changes of mitochondrial mass in the hemopoietic stem cell line FDCP-mix after treatment with etoposide: A correlative study by multiparameter flow cytometry and confocal and electron microscopy. *Experimental Cell Research*, *221*(2), 281–288. https://doi.org/10.1006/excr.1995.1376

Rothblum-Oviatt, C., Wright, J., Lefton-Greif, M. A., McGrath-Morrow, S. A., Crawford, T. O., & Lederman, H. M. (2016). Ataxia telangiectasia: A review. *Orphanet Journal of Rare Diseases*, *11*(1), 159. https://doi.org/10.1186/s13023-016-0543-7

Rotman, G., & Shiloh, Y. (1997a). Ataxia-telangiectasia: Is ATM a sensor of oxidative damage and stress? *Bioessays*, *19*(10), 911–917.

Rotman, G., & Shiloh, Y. (1997b). The ATM gene and protein: Possible roles in genome surveillance, checkpoint controls and cellular defence against oxidative stress. *Cancer Surveys*, *29*, 285–304.

Saunders-Pullman, R., Raymond, D., Stoessl, A. J., Hobson, D., Nakamura, K., Pullman, S., … Bressman, S. B. (2012). Variant ataxia-telangiectasia presenting as primary-appearing dystonia in Canadian Mennonites. *Neurology*, *78*(9), 649–657. https://doi.org/10.1212/WNL.0b013e3182494d51

Savitsky, K., Bar-Shira, A., Gilad, S., Rotman, G., Ziv, Y., Vanagaite, L., … Shiloh, Y. (1995). A single ataxia telangiectasia gene with a product similar to PI-3 kinase. *Science*, *268*(5218), 1749–1753.

Savitsky, K., Sfez, S., Tagle, D. A., Ziv, Y., Sartiel, A., Collins, F. S., … Rotman, G. (1995). The complete sequence of the coding region of the ATM gene reveals similarity to cell cycle regulators in different species. *Human Molecular Genetics*, *4*(11), 2025–2032.

Schafer, D. P., Lehrman, E. K., Kautzman, A. G., Koyama, R., Mardinly, A. R., Yamasaki, R., … Stevens, B. (2012). Microglia sculpt postnatal neural circuits in an activity and complement-dependent manner. *Neuron*, *74*(4), 691–705. https://doi.org/10.1016/j.neuron.2012.03.026

Schieber, M., & Chandel, N. S. (2014). ROS function in redox signaling and oxidative stress. *Current Biology*, *24*(10), R453–R462. https://doi.org/10.1016/j.cub.2014.03.034

Semlitsch, M., Shackelford, R. E., Zirkl, S., Sattler, W., & Malle, E. (2011). ATM protects against oxidative stress induced by oxidized low-density lipoprotein. *DNA Repair (Amst)*, *10*(8), 848–860. https://doi.org/10.1016/j.dnarep.2011.05.004

Sharma, N. K., Lebedeva, M., Thomas, T., Kovalenko, O. A., Stumpf, J. D., Shadel, G. S., & Santos, J. H. (2014). Intrinsic mitochondrial DNA repair defects in Ataxia Telangiectasia. *DNA Repair (Amst)*, *13*, 22–31. https://doi.org/10.1016/j.dnarep.2013.11.002

Shiloh, Y. (2003). ATM and related protein kinases: Safeguarding genome integrity. *Nature Reviews Cancer*, *3*(3), 155–168.

Shiloh, Y. (2014). ATM: Expanding roles as a chief guardian of genome stability. *Experimental Cell Research*, *329*(1), 154–161. https://doi.org/10.1016/j.yexcr.2014.09.002

Shiloh, Y., & Lederman, H. M. (2017). Ataxia-telangiectasia (A-T): An emerging dimension of premature ageing. *Ageing Research Reviews*, *33*, 76–88. https://doi.org/10.1016/j.arr.2016.05.002

Shiloh, Y., Tabor, E., & Becker, Y. (1983). Abnormal response of ataxia-telangiectasia cells to agents that break the deoxyribose moiety of DNA via a targeted free radical mechanism. *Carcinogenesis*, *4*(10), 1317–1322.

Shiloh, Y., & Ziv, Y. (2013). The ATM protein kinase: Regulating the cellular response to genotoxic stress, and more. *Nature Reviews in Molecular Cell Biology*, *14*(4), 197–210. https://doi.org/10.1038/nrm3546

Silvestri, G., Masciullo, M., Piane, M., Savio, C., Modoni, A., Santoro, M., & Chessa, L. (2010). Homozygosity for c 6325T>G transition in the ATM gene causes an atypical, late-onset variant form of ataxia-telangiectasia. *Journal of Neurology*, *257*(10), 1738–1740. https://doi.org/10.1007/s00415-010-5583-7

Sirbu, B. M., & Cortez, D. (2013). DNA damage response: Three levels of DNA repair regulation. *Cold Spring Harbor Perspectives in Biology*, *5*(8), a012724. https://doi.org/10.1101/cshperspect.a012724

Sirover, M. A. (1999). New insights into an old protein: The functional diversity of mammalian glyceraldehyde-3-phosphate dehydrogenase. *Biochimica et Biophysica Acta*, *1432*(2), 159–184.

Song, M., Martinowich, K., & Lee, F. S. (2017). BDNF at the synapse: Why location matters. *Molecular Psychiatry*, *22*(10), 1370–1375. https://doi.org/10.1038/mp.2017.144

Song, X., Ma, F., & Herrup, K. (2019). Accumulation of cytoplasmic DNA due to ATM deficiency activates the microglial viral response system with neurotoxic consequences. *The Journal of Neuroscience*, *39*(32), 6378–6394. https://doi.org/10.1523/JNEUROSCI.0774-19.2019

Soresina, A., Meini, A., Lougaris, V., Cattaneo, G., Pellegrino, S., Piane, M., … Plebani, A. (2008). Different clinical and immunological presentation of ataxia-telangiectasia within the same family. *Neuropediatrics*, *39*(1), 43–45. https://doi.org/10.1055/s-2008-1076736

Stensaas, L. J., & Reichert, W. H. (1971). Round and amoeboid microglial cells in the neonatal rabbit brain. *Zeitschrift für Zellforschung und Mikroskopische Anatomie*, *119*(2), 147–163. https://doi.org/10.1007/BF00324517

Stern, N., Hochman, A., Zemach, N., Weizman, N., Hammel, I., Shiloh, Y., … Barzilai, A. (2002). Accumulation of DNA damage and reduced levels of nicotine adenine dinucleotide in the brains of Atm-deficient mice. *The Journal of Biological Chemistry*, *277*(1), 602–608.

Stowell, R. D., Wong, E. L., Batchelor, H. N., Mendes, M. S., Lamantia, C. E., Whitelaw, B. S., & Majewska, A. K. (2017). Cerebellar microglia are dynamically unique and survey Purkinje neurons in vivo. *Developmental Neurobiology*, *78*(6), 627–644. https://doi.org/10.1002/dneu.22572

Stracker, T. H., Roig, I., Knobel, P. A., & Marjanovic, M. (2013). The ATM signaling network in development and disease. *Frontiers in Genetics*, *4*, 37. https://doi.org/10.3389/fgene.2013.00037

Stratoulias, V., Venero, J. L., Tremblay, M. E., & Joseph, B. (2019). Microglial subtypes: Diversity within the microglial community. *The EMBO Journal*, *38*(17), e101997. https://doi.org/10.15252/embj.2019101997

Sun, Y., Xu, Y., Roy, K., & Price, B. D. (2007). DNA damage-induced acetylation of lysine 3016 of ATM activates ATM kinase activity. *Molecular and Cellular Biology*, *27*(24), 8502–8509. https://doi.org/10.1128/MCB.01382-07

Tamashiro, T. T., Dalgard, C. L., & Byrnes, K. R. (2012). Primary microglia isolation from mixed glial cell cultures of neonatal rat brain tissue. *Journal of Visualized Experiments*, *66*, 1–5. https://doi.org/10.3791/3814

Taylor, A. M., Harnden, D. G., Arlett, C. F., Harcourt, S. A., Lehmann, A. R., Stevens, S., & Bridges, B. A. (1975). Ataxia telangiectasia: A human mutation with abnormal radiation sensitivity. *Nature*, *258*(5534), 427–429.

Taylor, A. M., Lam, Z., Last, J. I., & Byrd, P. J. (2014). Ataxia telangiectasia: More variation at clinical and cellular levels. *Clinical Genetics*, *87*(3), 199–208. https://doi.org/10.1111/cge.12453

Thompson, L. H. (2012). Recognition, signaling, and repair of DNA double-strand breaks produced by ionizing radiation in mammalian cells: The molecular choreography. *Mutation Research*, *751*(2), 158–246. https://doi.org/10.1016/j.mrrev.2012.06.002

Tolbert, C. E., Beck, M. V., Kilmer, C. E., & Srougi, M. C. (2019). Loss of ATM positively regulates Rac1 activity and cellular migration through oxidative stress. *Biochemical and Biophysical Research Communications*, *508*(4), 1155–1161. https://doi.org/10.1016/j.bbrc.2018.12.033

Trapp, B. D., Wujek, J. R., Criste, G. A., Jalabi, W., Yin, X., Kidd, G. J., … Ransohoff, R. (2007). Evidence for synaptic stripping by cortical microglia. *GLIA*, *55*(4), 360–368. https://doi.org/10.1002/glia.20462

Ulmann, L., Hatcher, J. P., Hughes, J. P., Chaumont, S., Green, P. J., Conquet, F., … Rassendren, F. (2008). Up-regulation of P2X(4) receptors in spinal microglia after peripheral nerve injury mediates BDNF release and neuropathic pain. *Journal of Neuroscience*, *28*(44), 11263–11268. https://doi.org/10.1523/Jneurosci.2308-08.2008

Vail, G., Cheng, A., Han, Y. R., Zhao, T., Du, S., Loy, M. M., … Plummer, M. R. (2016). ATM protein is located on presynaptic vesicles and its deficit leads to failures in synaptic plasticity. *Journal of Neurophysiology*, *116*(1), 201–209. https://doi.org/10.1152/jn.00006.2016

Valentin-Vega, Y. A., & Kastan, M. B. (2012). A new role for ATM: Regulating mitochondrial function and mitophagy. *Autophagy*, *8*(5), 840–841. https://doi.org/10.4161/auto.19693

Valentin-Vega, Y. A., Maclean, K. H., Tait-Mulder, J., Milasta, S., Steeves, M., Dorsey, F. C., … Kastan, M. B. (2012). Mitochondrial dysfunction in ataxia-telangiectasia. *Blood*, *119*(6), 1490–1500. https://doi.org/10.1182/blood-2011-08-373639

Verhagen, M. M., Abdo, W. F., Willemsen, M. A., Hogervorst, F. B., Smeets, D. F., Hiel, J. A., … van Deuren, M. (2009). Clinical spectrum of ataxia-telangiectasia in adulthood. *Neurology*, *73*(6), 430–437. https://doi.org/10.1212/WNL.0b013e3181af33bd

Verhagen, M. M., Last, J. I., Hogervorst, F. B., Smeets, D. F., Roeleveld, N., Verheijen, F., … Willemsen, M. A. (2012). Presence of ATM protein and residual kinase activity correlates with the phenotype in ataxia-telangiectasia: A genotype-phenotype study. *Human Mutation*, *33*(3), 561–571. https://doi.org/10.1002/humu.22016

Vijg, J., & Suh, Y. (2013). Genome instability and aging. *Annual Review of Physiology*, *75*, 645–668. https://doi.org/10.1146/annurev-physiol-030212-183715

Wada, R., Tifft, C. J., & Proia, R. L. (2000). Microglial activation precedes acute neurodegeneration in Sandhoff disease and is suppressed by bone marrow transplantation. *Proceedings of the National Academy of Sciences of the United States of America*, *97*(20), 10954–10959.

Wake, H., Moorhouse, A. J., Miyamoto, A., & Nabekura, J. (2013). Microglia: Actively surveying and shaping neuronal circuit structure and function. *Trends in Neurosciences*, *36*(4), 209–217. https://doi.org/10.1016/j.tins.2012.11.007

Wang, C., & Youle, R. J. (2009). The role of mitochondria in apoptosis*. *Annual Review of Genetics*, *43*, 95–118. https://doi.org/10.1146/annurev-genet-102108-134850

Wang, N., Zhang, Q., Luo, L., Ning, B., & Fang, Y. (2017). Beta-asarone inhibited cell growth and promoted autophagy via P53/Bcl-2/Bclin-1 and P53/AMPK/mTOR pathways in human glioma U251 cells. *Journal of Cellular Physiology*, *233*(3), 2434–2443. https://doi.org/10.1002/jcp.26118

Worth, P. F., Srinivasan, V., Smith, A., Last, J. I., Wootton, L. L., Biggs, P. M., … Taylor, A. M. (2013). Very mild presentation in adult with classical cellular phenotype of ataxia telangiectasia. *Movement Disorders*, *28*(4), 524–528. https://doi.org/10.1002/mds.25236

Wu, Y., Dissing-Olesen, L., MacVicar, B. A., & Stevens, B. (2015). Microglia: Dynamic mediators of synapse development and plasticity. *Trends in Immunology*, *36*(10), 605–613. https://doi.org/10.1016/j.it.2015.08.008

Xu, B., Kim, S. T., Lim, D. S., & Kastan, M. B. (2002). Two molecularly distinct G(2)/M checkpoints are induced by ionizing irradiation. *Molecular and Cellular Biology*, *22*(4), 1049–1059.

Xu, Y., Ashley, T., Brainerd, E. E., Bronson, R. T., Meyn, M. S., & Baltimore, D. (1996). Targeted disruption of ATM leads to growth retardation, chromosomal fragmentation during meiosis, immune defects, and thymic lymphoma. *Genes & Development*, *10*(19), 2411–2422.

Yang, D. Q., Halaby, M. J., Li, Y., Hibma, J. C., & Burn, P. (2011). Cytoplasmic ATM protein kinase: An emerging therapeutic target for diabetes, cancer and neuronal degeneration. *Drug Discovery Today*, *16*(7-8), 332–338. https://doi.org/10.1016/j.drudis.2011.02.001

Yang, Y., Hui, C. W., Li, J., & Herrup, K. (2014). The interaction of the atm genotype with inflammation and oxidative stress. *PLoS One*, *9*(1), e85863. https://doi.org/10.1371/journal.pone.0085863

Yu, A. C., Neil, S. E., & Quandt, J. A. (2017). High yield primary microglial cultures using granulocyte macrophage-colony stimulating factor from embryonic murine cerebral cortical tissue. *Journal of Neuroimmunology*, *307*, 53–62. https://doi.org/10.1016/j.jneuroim.2017.03.018

Zecca, L., Zucca, F. A., Albertini, A., Rizzio, E., & Fariello, R. G. (2006). A proposed dual role of neuromelanin in the pathogenesis of Parkinson's disease. *Neurology*, *67*(7 Suppl 2), S8–S11.

Zhao, H., Halicka, H. D., Li, J., Biela, E., Berniak, K., Dobrucki, J., & Darzynkiewicz, Z. (2013). DNA damage signaling, impairment of cell cycle progression, and apoptosis triggered by 5-ethynyl-2'-deoxyuridine incorporated into DNA. *Cytometry. Part A*, *83*(11), 979–988. https://doi.org/10.1002/cyto.a.22396

Ziv, Y., Bar-Shira, A., Pecker, I., Russell, P., Jorgensen, T. J., Tsarfati, I., & Shiloh, Y. (1997). Recombinant ATM protein complements the cellular A-T phenotype. *Oncogene*, *15*(2), 159–167.

Ziv, Y., Jaspers, N. G., Etkin, S., Danieli, T., Trakhtenbrot, L., Amiel, A., … Shiloh, Y. (1989). Cellular and molecular characteristics of an immortalized ataxia-telangiectasia (group AB) cell line. *Cancer Research*, *49*(9), 2495–2501.

SUPPORTING INFORMATION

Additional supporting information may be found in the online version of the article at the publisher's website.

White Paper

January 15, 2021

Keywords or phrases:
Astrocyte, Astroglia, Live-Cell Analysis, Cell Migration and Invasion, Neuronal Cell Health, Neuronal Activity, Cell Cycle

Characterizing Astroglia Models With Live-Cell Analysis

S. L. Alcantara, J. Trigg, T. Campbell, J. Rauch, L. Oupicka, T. Jackson, N. Holtz, E. Endsley, C. Schramm, D. Appledorn and T. Dale

The Diverse Astrocyte—A Confirmed Key Player in the Nervous System

Astrocytes are a type of specialized glial cell ubiquitously distributed throughout the brain and spinal cord. It is estimated that they occupy 50% of the total volume of the central nervous system (CNS) and that they outnumber neurons by over fivefold.[1] Interestingly, the number, complexity, and diversity of astroglia cells have increased considerably with evolution[2], and research from several groups indicate the existence of gender differences.[3] Historically, astrocytes have been regarded as mere supporters of neuronal function, but mounting evidence indicates that they not only support neuronal activity, but directly contribute to it.

Astrocytes are a heterogenous population of cells with distinctive morphological and functional characteristics, that have specialized to their different brain regions and locations.[4] Remarkably, regional populations of astrocytes appear to also exhibit local heterogeneity.[5] Protoplasmic astrocytes, present in the grey matter, consist of fine and complex branching processes that envelop synapses and enable bidirectional communication.[6] In contrast, fibrous astrocytes, present in the white matter, contact the myelin-sheath gaps, Nodes of Ranvier[7], and are generally more coarse and less extensively branched. Morphological variation is best characterized by *in vivo* imaging, however further development is needed for *in vitro* replication.

During development, astrocytes guide axonal migration and assist the formation and function of developing synapses.[8] By interaction with pericytes, epithelial cells and blood vessels, they orchestrate CNS flow and modulate the blood brain barrier (BBB).[9] Interestingly, they form regional islands of non-overlapping astrocytes[10], composed of thousands of synapses, enabling synaptic and blood flow control over large regions.[11] They also function as key regulators of energy metabolism.[12] Maintaining brain homeostasis function is imperative. Under pathological conditions, such as injury, neurodegeneration, or infection, reactive astrocytes together with microglia participate in the inflammatory response, playing a key role in the progression of neurodegenerative diseases.[13]

Find out more: www.essenbioscience.com/en/communications/assays-neuroscience-research/

Here we describe how a combination of live-cell analysis techniques provide the flexibility required to enable the characterization of these highly dynamic astrocytic models, by quantifying their growth, morphology, motility, and functional analysis.

Live-Cell Analysis Applied to Astroglia Characterization

Real-time, live-cell analysis is redefining the possibilities and workflows of cell biology. This technique is based on non-invasive time-lapse image acquisition and automatic software segmentation. This enables researchers to monitor and measure cell behaviors and phenotypes in a non-perturbing manner, over long periods of time, and in real-time, allowing for informed and data-driven decisions to be incorporated within the routine experimental work-flow. The Incucyte® Live-Cell Analysis System provides flexible kinetic quantification of biological phenotypes to monitor growth, morphology, motility, and cellular function.[14]

To exemplify the use of live-cell analysis to monitor and compare the diversity of cultured astroglia phenotypes, rat primary astrocytes isolated from different brain regions (cortex, hippocampus, and cerebellum), were grown *in vitro*. Time-lapse images were automatically acquired, segmented, and quantified in real-time (Figure 1). Segmentation of these images at each time-point allows for the generation of time-courses, enabling kinetic assessment of morphological change. In addition, metric variability can be derived from this data, leading to assay optimization and an increased experimental robustness. In this *in vitro* paradigm, cortical astrocytes presented a faster rate of growth (confluence) and a lower ramification (analyzed with Incucyte® Neurotrack Analysis Software Module), when compared to astrocytes isolated from the hippocampus or cerebellum.

From this data, one can extrapolate the potential that live-cell analysis brings to the research of these very dynamic and heterogeneous type of cells.

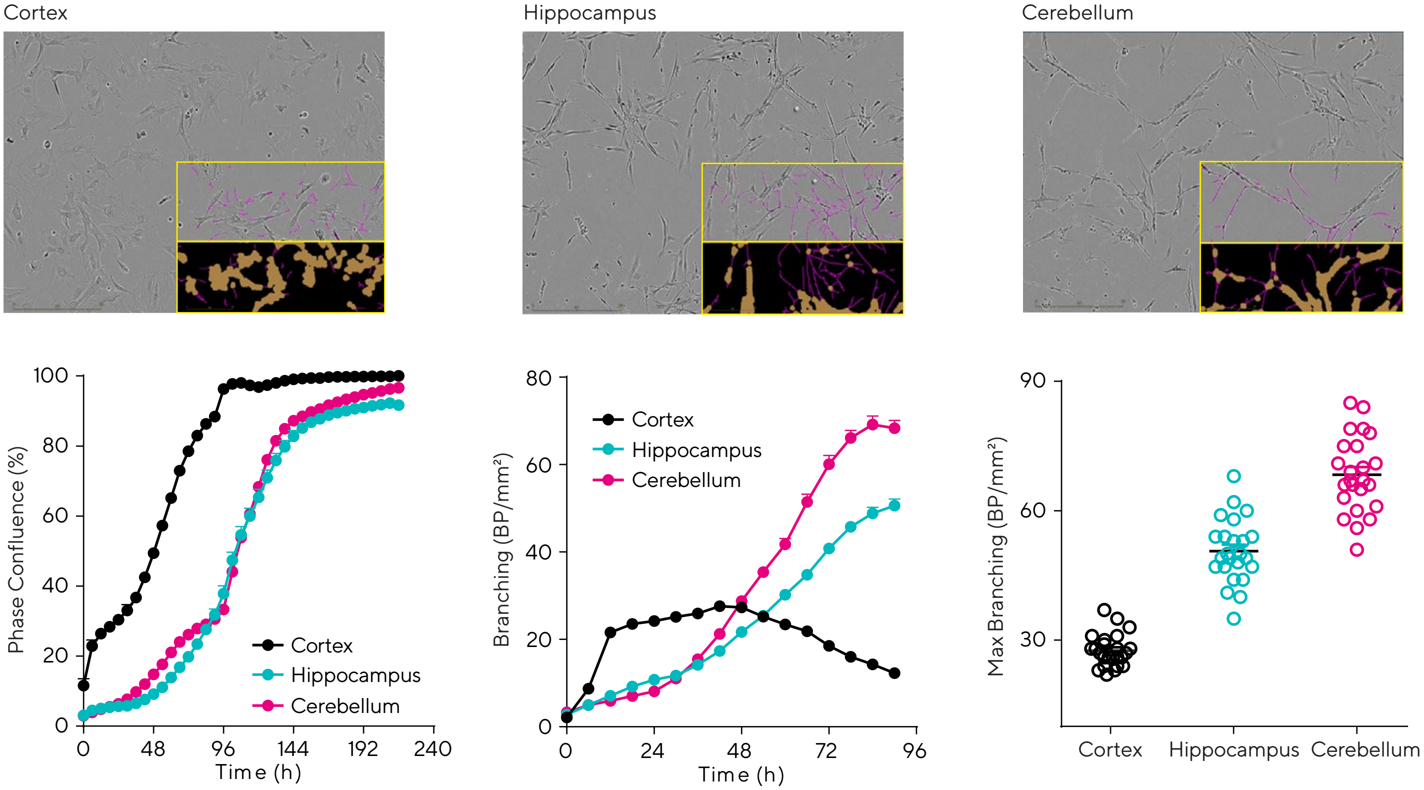

Figure 1: Temporal monitoring of brain region astroglia revealed differences in cell growth and morphology. Cortex, Hippocampus, and Cerebellum astroglia were seeded in 96-well plates at 2,000 cells/well. Proliferation and morphology were monitored over 10 days. Images show cultures at 30–40% confluence (2 days, cortical, or 4 days, hippocampal and cerebellar). Time-course profile compares growth across brain regions and reveals cortical astrocytes have the fastest rate of growth. Glia ramification (pink and brown masks) is compared over time with cerebellum astrocytes yielding the highest ramification by 96 h (68.3 ± 1.8 branch points (BP)/mm²) followed by hippocampal (50.6 ± 1.5 BP/mm²) and cortical (12.3 ± 0.7 BP/mm²). Maximum ramification for each well is also shown (variability plot). Data presented as mean ± SEM (24 replicates) and images were captured at 10X magnification.

Cell Monitoring and Workflow Optimization

As advanced cell assays become technically more complex, the need to holistically capture dynamic and sometimes subtle cellular events becomes ever more important. Introducing live-cell monitoring during cell culture QC provides an opportunity for better-informed decision-making, such as the best time to manipulate the culture, or perform the assay. This ensures that the models are optimal from the outset, which in turn validates and improves the assay readout, resulting in an enhanced data interpretation, increased reliability, and improved experimental success.[15]

Appropriately adjusting seeding density improves cellular health while minimizing the time for assay readiness. Figure 2 shows the kinetic correlation of confluence with seeding density for the human glioblastoma T98G cell line.

The software capability to discriminate cells from background is seen in the segmented image. The automatic segmentation calculates a confluence value in real-time. The confluence values are concatenated to provide a growth profile for each well of the plate, which can be used to assess the optimal seeding density and appropriate assaying time for each specific cell type.

The importance of the culture environment for a primary astrocytic line was studied by seeding rat cortical astrocytes on several extracellular matrices (ECM), such as Poly-D-Lysine (PDL), Poly-L-Lysine (PLL) or Poly-L-Ornithine (PLO), and kinetically following their confluence. The data demonstrates the effect of coating a tissue culture vessel on cell growth and an indication of assay variability.

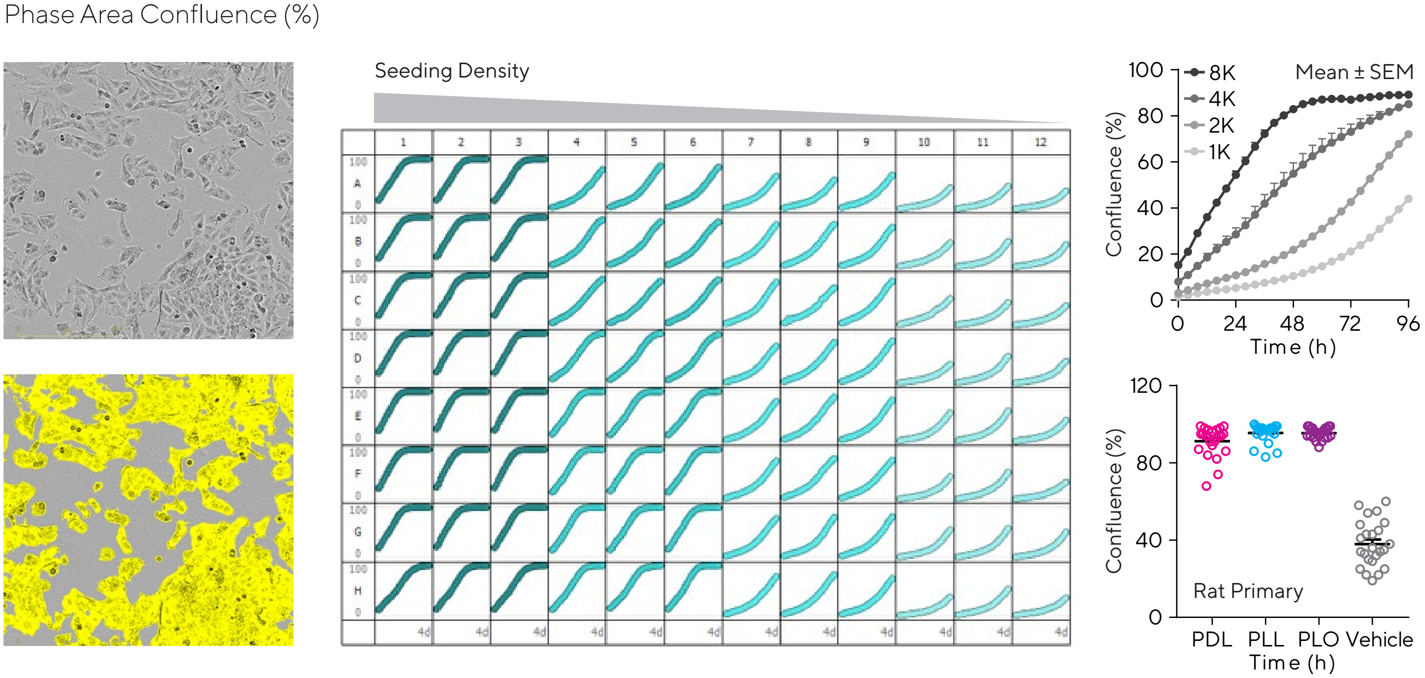

Figure 2: Cell monitoring and workflow optimization. Human glioblastoma T98G cells were seeded in 96-well plates at several densities (1,000–8,000 cells/well). Cellular proliferation was monitored over 4 days. Representative phase images show the segmented cells at 4,000 cells/well and 4 days post-seeding. Plate view represents cell growth in each well of a microtiter plate. Time-course profiles compare astrocyte growth at the different densities tested. The importance of an extracellular matrix is presented in the variability plot, where rat primary cortical astrocytes were seeded at 4,000 cells/well in PLL, PDL, or PLO (0.02–1 mg/mL) pre-coated 96-well plates and each individual confluence value at 4 days was obtained. Data presented as mean ± SEM, 12–24 replicates.

Ensuring assay quality with live-cell analysis offers scientists benefits at every stage of their cell assay workflow. Continually monitoring cell culture during the study improves the understanding of cellular events, while the ability to retrospectively assess images enables scientists to make better informed decisions. Live-cell monitoring ensures efficient use of resources, which is further enhanced by its non-invasive and cell-sparing nature. Additionally, live-cell analysis allows pre-treatment normalization of cells, which further increases assay robustness and enables accurate characterization of small changes.

Modulating Astroglia Health, Morphology and Growth

It is generally accepted that primary astrocyte proliferation occurs mainly during brain development, and adult astrocytes, under healthy conditions, do not proliferate. However, neural stem cells, which have characteristics of astrocytes, retain the ability of self-renewal. Furthermore, astrocytes can regain their proliferative properties under pathological conditions, such as stress, neurodegeneration, or injury.[16]

Reactive astrogliosis is deemed a pathological hallmark of altered CNS tissue, with reactive astrocytes found in areas surrounding severe focal lesions, and characterized by proliferation and morphological change, leading to the generation of the glial scar.[17] Reactive protoplasmic astrocytes in the cortex have shown to re-enter the cell cycle and start proliferating within 3 to 5 days post-injury.[18]

In order to generate a cell-based model to study and modulate pathological conditions, injury was induced in primary cerebella astrocytes by increasing their intracellular calcium levels using the Calcium chelator ionomycin.[19] The effect of this drug on growth, viability, and morphology was assessed using live-cell imaging (Figure 3). Confluence measurements showed ionomycin-induced inhibition on cell growth. Apoptosis was measured via visualization and quantification of the kinetic externalization of phosphatidyl serine (PS) using Incucyte® Annexin V NIR Dye. As expected, proliferation and apoptosis are inversely proportional, as shown by the concentration response curves (CRCs). Interestingly, at early timepoints (< 24 h) ionomycin induced concentration-dependent increases in ramification.

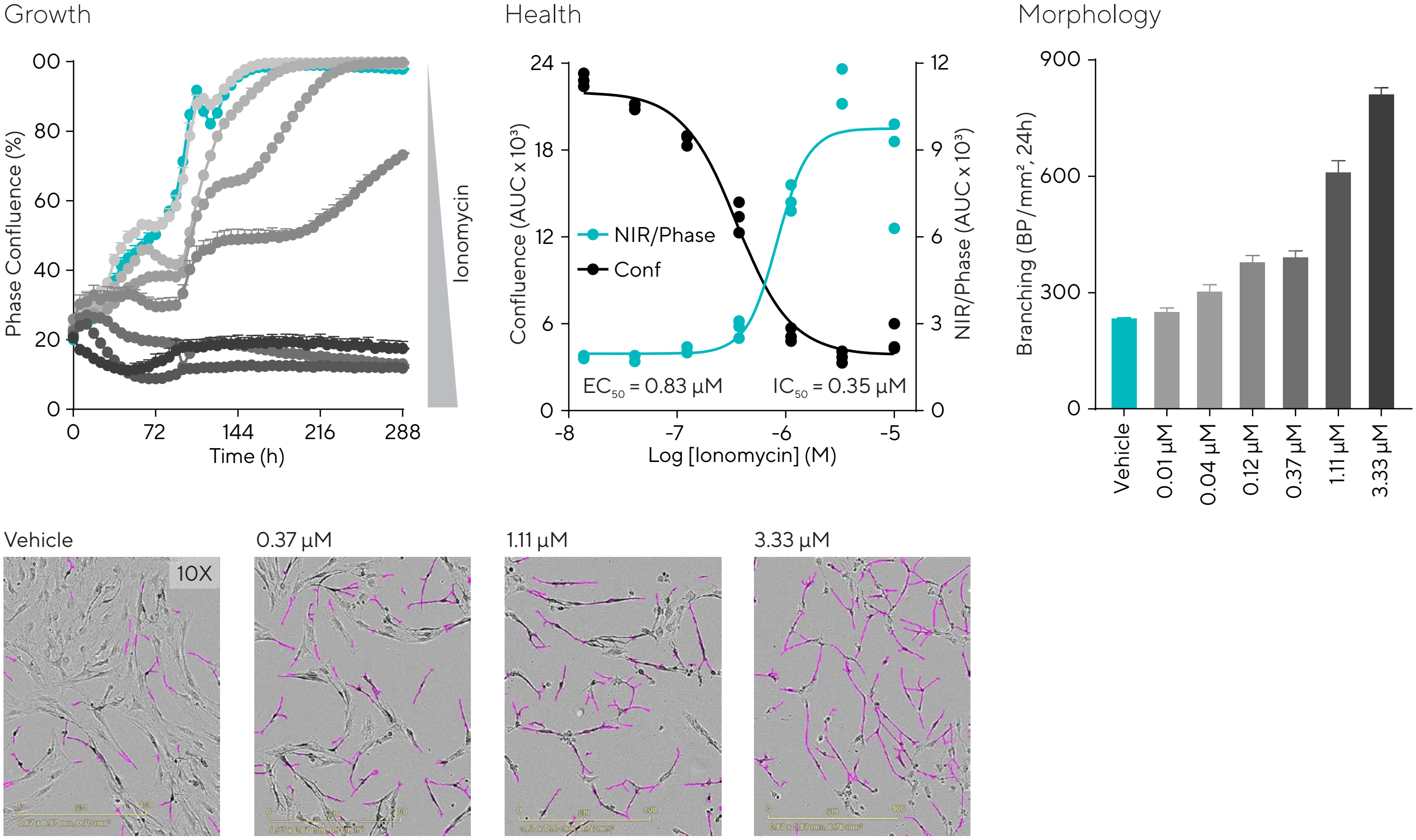

Figure 3: Effects of calcium increase in cerebellar astrocytes cellular growth, morphology, and health. Cerebellum astrocytes were seeded in 96-well plates at 10,000 cells/well and treated with Ionomycin (0.01–10 µM) in media supplemented with Incucyte® Annexin V NIR Dye. Proliferation, cell health, and morphology were monitored over 10 days. Time-course shows the effect of Ionomycin on cell growth. Concentration response curves compare the effect of Ionomycin on cell growth and apoptosis. The bar graph quantifying morphology and representative images demonstrate that the drug increased ramification at concentrations above 10 nM. Data presented as mean ± SEM, 3 replicates, and images captured at 10X magnification.

The role of astrocytes in neurodegeneration is becoming increasingly evident, and the potential of novel stem cell-based platforms in modelling these diseases is gaining momentum. The importance of astrocytes in Alzheimer's disease (AD) is currently strongly emerging.[20] In order to gain a deeper insight into cell cycle dynamics, human T98G glioblastoma cells were stably infected with the Incucyte® Cell Cycle Green | Orange Lentivirus, which enables quantification of cells in the G1 (orange), S | G2 | M (green), or transitioning (G1 to S in yellow; M to G1 non-fluorescent) cell cycle phases without altering cell function and in real-time (Figure 4). Images show T98G cells as they grow and divide. Quantification and classification of the different populations was performed by the Incucyte® Cell-by-Cell Analysis Software Module[21], allowing individual cells to be segmented and classified according to the orange and green fluorescent intensity. This provides an insight into the phenotypic biology of subsets of cells within a culture. Kinetic quantification of the percentage of cells at each phase exhibits the culture growth dynamic. Pharmacological modulation allows the study of drug-induced treatment effects on proliferation. The effect of the PP2A inhibitor Okadaic acid (OKA) was studied in an astrocytic cell model of AD. The data indicates that inhibiting phosphorylation via OKA arrested T98G astrocytes in S | G2 | M phase in a concentration dependent manner.

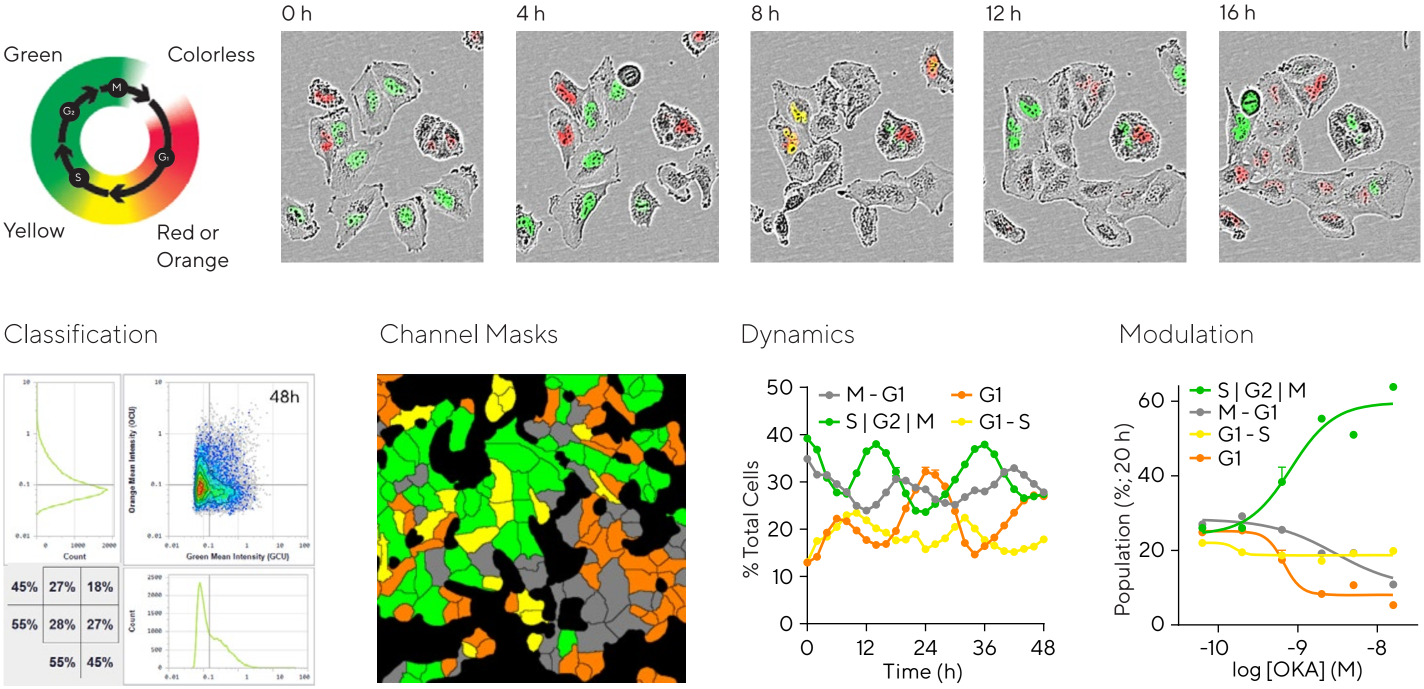

Figure 4: Effect of inhibiting phosphorylation in an astrocytic model of Alzheimer's Disease. T98G glioblastoma cells stably expressing Incucyte® Cell Cycle were seeded in 96-well plates at 4,000 cells/well. Schematic displays the color expression of the reagent. Representative images show a cycling cell cluster over time. For Cell Cycle quantification, images were acquired in Incucyte ® Cell-by-Cell Analysis Software Module to allow individual cells to be segmented and classified according to orange and green fluorescence intensity. Classification masks shows cells identified as orange, green, yellow, or non-fluorescent at a time-point. Time-course reveals the dynamics of each of the populations of T98G cells. To examine cell cycle modulation, T98G cells were treated with the protein phosphatase inhibitor Okadaic Acid (OKA; 0.14–50 nM). The concentration-response curves break down the percentage of cells at each phase for a given concentration at 20 h post-treatment. This data indicates that inhibiting phosphorylation via OKA arrested T98G astrocytes in S | G2 | M phase in a concentration dependent manner. Data presented as mean ± SEM, 6 replicates.

Insights into Astroglia Motility

It is during development, disease, and post-injury that astrocytes have been found to divide and migrate. In a pro-inflammatory environment, astrocytes undergo astrogliosis and change from naïve to reactive in a reversible manner, changing their morphology and protein expression. In order to minimize propagation of the lesion, this glia then proliferate and migrate to the lesion site and form the irreversible glial scar.[22] A very recent and exciting study using single nucleus RNA-sequencing discovered a novel and intermediate astrocytic state present in Alzheimer's and in lesser extent, in aging mouse and human brains. These Disease Associated Astrocytes (DAAs) switch from homeostatic astrocytes by upregulating metabolic, immune, stress, and aging pathways.[23] Characterizing these reversible glia states via elucidating the molecular mechanisms regulating astrocyte motility provides a window of opportunity for therapeutic intervention for neurodegenerative diseases, stroke, and injury.[24]

Here we present a cell model to study astrocytic migration post-injury, using live-cell analysis and the Incucyte® Scratch Wound Assay.[25] Time-lapse images from a scratch wound assay can be analyzed, and the rate of cell migration and wound closure quantified using the relative wound density (RWD) metric. Primary astrocytes from different brain regions (cortex, hippocampus, and cerebellum), and iPSC derived cortical iCell Astrocytes (Fujifilm) were seeded at 80–90% confluence in PLL pre-coated plates. 96 independent scratches were simultaneously performed using the Incucyte® 96-well Woundmaker Tool. The baseline rate of wound closure was obtained for the different cell types (Figure 5). When treated with Ionomycin, iCell Astrocytes presented a decreased motility in a concentration-dependent manner.

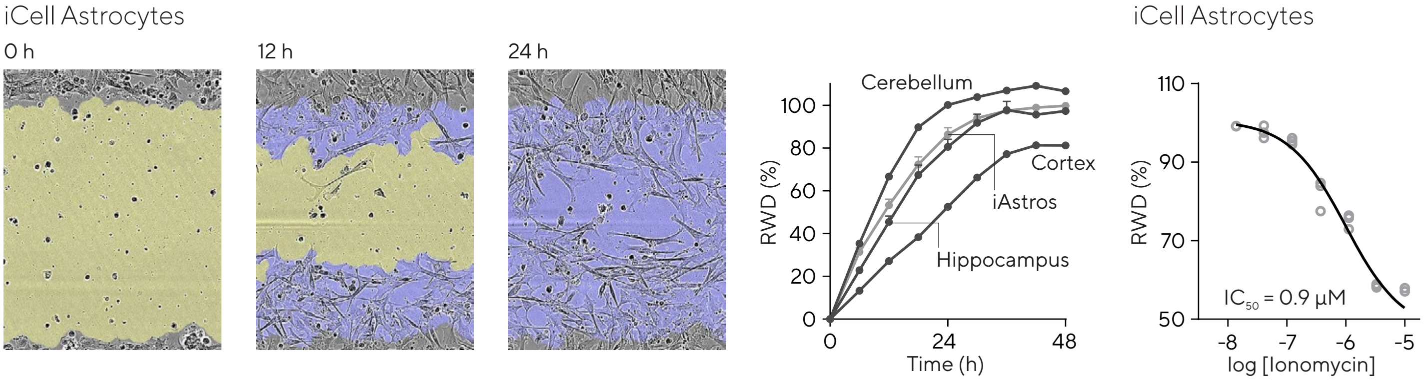

Figure 5: Brain region dependent astrocytic migration post-injury and pharmacological modulation. Primary (Cortex, Hippocampus, Cerebellum) or iPSC (iCell, Fujifilm) astrocytes were seeded in Incucyte® Imagelock 96-well Plates at 30,000 cells/well and precise, reproducible wounds were created with the Incucyte® Woundmaker. Images were acquired using the Incucyte® Live-Cell Analysis System. Images show migration of iPSC derived iCell Astrocytes at 0, 12, and 24 h post-injury, allowing qualitative morphological assessment. Segmentation indicates initial wound mask (blue) and time-dependent mask (yellow). Time-course profiles compare rate of wound closure for different brain regions with cerebellar astroglia migrating the fastest. For pharmacological studies, iPSC astroglia were incubated with ionomycin (0.01–10 µM) at time of wounding. A concentration-dependent inhibition of migration was observed (IC_{50} = 0.9 µM). Data presented as mean ± SEM, 3 replicates.

To gain further biological insight into glia motility towards site of injury, a live-cell model of chemotactic migration was developed. Human T98G astrocytic line was plated in the Incucyte® Clearview 96-well Plates.[26] Each well provides an optically clear surface for label-free imaging and a membrane consisting of 96 laser etched pores. Cells were seeded in the upper chamber in low serum media and Fetal Bovine Serum (FBS, 0–10%) as the chemoattractant added to the lower reservoir plate. Directional migration between top and bottom side of the membrane was monitored and quantified using the Incucyte® Chemotaxis Analysis Software Module[27] (Figure 6). A concentration-dependent migration of T98G cells through the pores was observed, demonstrating the potential of this model to study chemotactic astroglia migration.

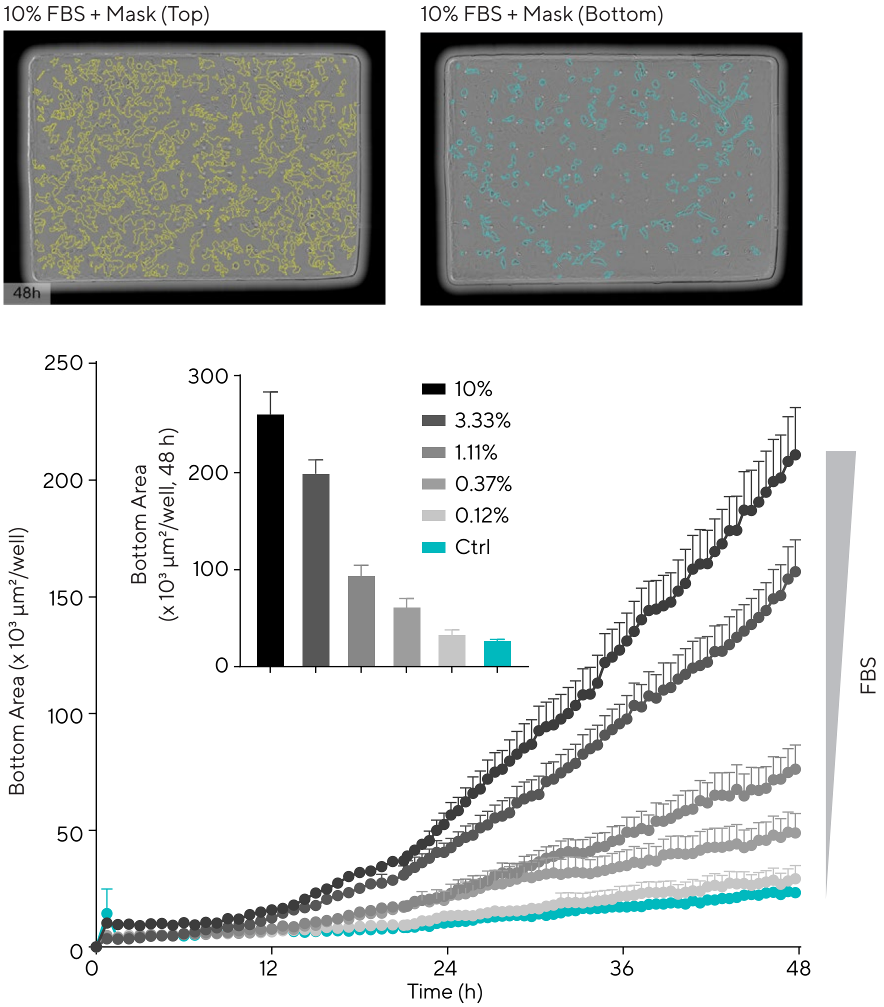

Figure 6: T98G astrocyte chemotactic migration towards FBS. T98G cells were plated in the top chamber of the Incucyte® Clearview 96-Well Plate coated with PDL (0.1 mg/mL) at a density of 1,000 cells/well. Once the cells had adhered, Fetal Bovine Serum (FBS; 0.12–10%) was added to the bottom chamber as a chemoattractant. Images, and respective masks, are representative of the top and bottom side of the membrane at 48 h post-addition. Time-course and bar-graph data indicate a concentration-dependent increase in migration through the pore with increasing levels of FBS. Data presented as mean ± SEM, 6 replicates.

Astrocytic Modulation of Neuronal Signaling in Co-Cultures

As opposed to the traditional view that brain function results exclusively from neuronal activity, it is now widely accepted as a more coordinated perspective involving both neurons and glia. Astrocytes are regarded as active partners in brain activity via bidirectional communication, orchestrated at the tripartite synapse, composed of the neuronal pre- and post-synapses and their close interaction with the surrounded astroglia.[28]

In order to understand the effect of astrocytes in the signaling response of neurons via measurements of calcium oscillations, a humanized live-cell model of neuronal activity was developed in collaboration with Talisman Therapeutics. Recent advances in human induced pluripotent stem cell (hiPSC) offer a powerful *in vitro* model strategy for the study of both healthy and disease stages of the human nervous system. Non-perturbing neurite outgrowth measurements can be performed in mono- or co-culture (post-infection with Incucyte® Neurolight Orange Lentivirus[29]) via automatic segmentation of time-lapse imaging using the Incucyte® Neurotrack Analysis Software Module.[30] Cell bodies and neurites are discriminated and kinetically quantified. For Neuronal Activity measurements, neurons can be infected with the synaptic driven Incucyte® Neuroburst Orange Lentivirus.[31] High-frequency images (3 frames/second) are obtained, and fluorescent calcium bursts are quantified over-time using the Incucyte® Neuronal Activity Analysis Software Module.[32] When co-cultured with astrocytes, neurons developed greater and more branched neurites compared to monocultures (Figure 7). The functional profile of co-cultures also differed of that of monocultures, the former showing greater active objects (1/image), burst duration (sec), and lower burst rate (1/min), at a similar correlation, indicating greater network stability in the presence of glial cells.

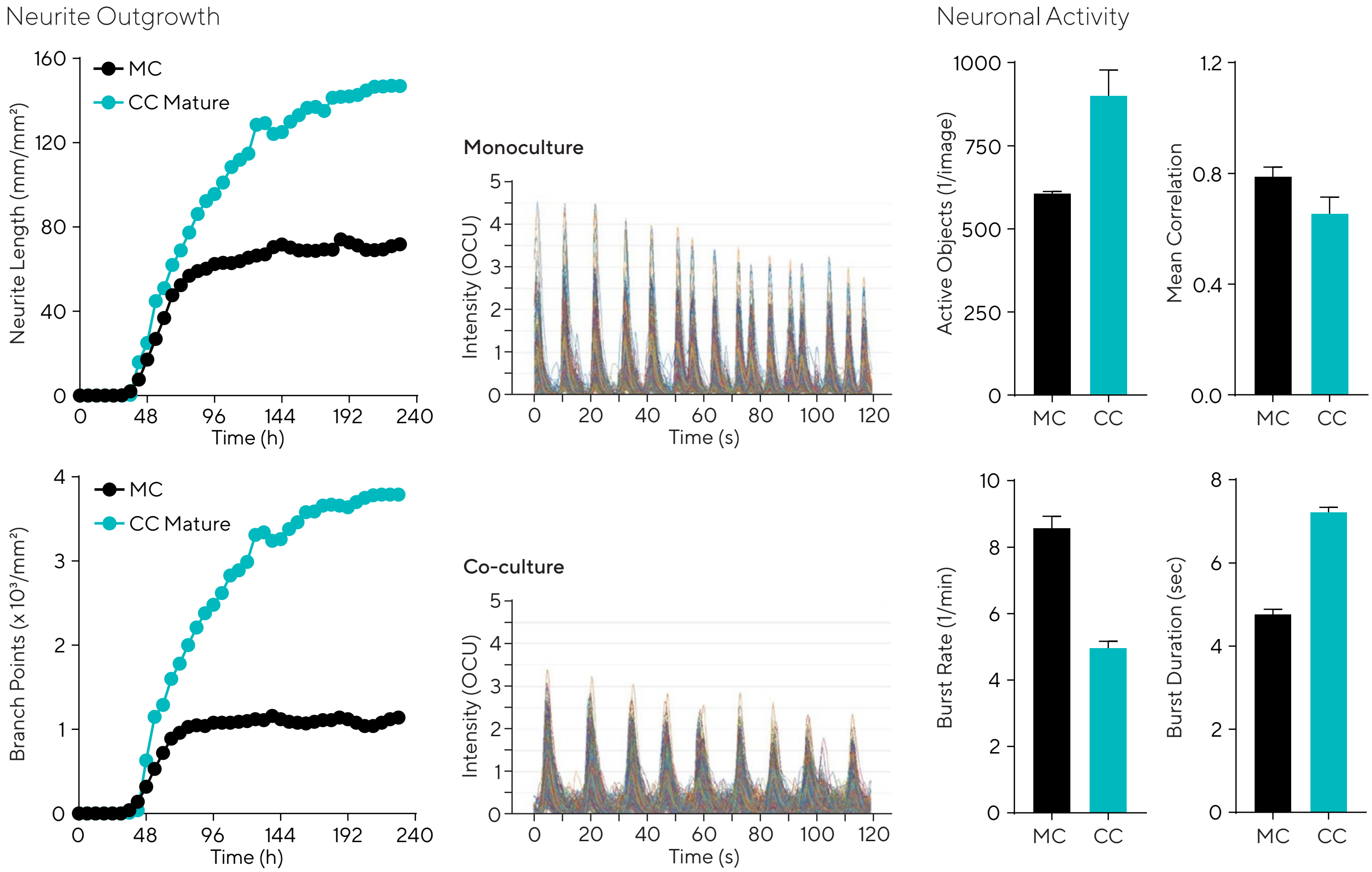

Figure 7: iPSC neurons co-cultured with mature astrocytes yield greater outgrowth and branching and neuronal network activity is modified. Network activity in neuron-astrocyte co-culture differs from monocultures, displaying a reduced frequency of longer-lasting burst rates (characteristic of a more mature neuronal network through the development of a network's ability to fire trains of APs). N = 12. Traces and bar charts are 23 days post-infection.

Conclusion

In this white paper, we described several live-cell phenotypic analyses suitable for the characterization of astroglia cells. When used in combination, the growth, health, morphology, motility, and functional effects, as well as their modulation, can be studied in a flexible and dynamic manner, ideally suited for this type of heterogenous and plastic cells.

New technological tools, adapted to the glia dynamism, can provide the stepping stone to further our understanding of this once undervalued brain cell type. When used in combination to traditional downstream techniques, one can achieve a wider view on the influence that glia has in neuronal health and disease, opening the door to more translatable cell models suitable for improved therapeutics.

References

1. Sofroniew MV and Vinters HV. **Astrocytes: biology and pathology.** *Acta Neuropathologica,* 1(119);7-35 (2010)
2. Nedergaard M, Ransom B, and Goldman SA. **New roles for astrocytes: Redefining the functional architecture of the brain.** *Trends in Neurosciences,* 26(10);523-530 (2003)
3. Santos-Galindo M, Acaz-Fonseca E, Bellini MJ, and Garcia-Segura LM. **Sex differences in the inflammatory response of primary astrocytes to lipopolysaccharide.** *Biology of Sex Differences,* 2(1);7 (2011)
4. Verkhratsky A and Nedergaard M. **Physiology of Astroglia.** *Physiological Reviews,* 98(1);239-289 (2018)
5. Hewett JA. **Determinants of regional and local diversity within the astroglial lineage of the normal central nervous system.** *Journal of Neurochemestry,* 110(6);1717-1736 (2009)
6. Arizono M, Inavalli VVGK, Panatier A, *et al.* **Structural basis of astrocytic Ca2+ signals at tripartite synapses.** *Nature Communications,* 11;1906 (2020)

7. Guo F, Ma J, and Pleasure DE. **Astrocytes.** *Encyclopedia of the Neurological Sciences (2nd Edition),* 287-289 (2014)
8. Reemst K, Noctor SC, Lucassen PJ, and Hol EM. **The Indispensable Roles of Microglia and Astrocytes during Brain Development.** *Frontiers in Human Neuroscience,* 10;566 (2016)
9. Cabezas R, Avila M, Gonzalez J, *et al.* **Astrocytic modulation of blood brain barrier: perspectives on Parkinson's disease.** *Frontiers in Cellular Neuroscience,* 8;211 (2014)
10. Halassa MM, Fellin T, Takano H, *et al.* **Synaptic Islands Defined by the Territory of a Single Astrocyte.** *Journal of Neuroscience,* 27(24);6473-6477 (2007)
11. Bushong EA, Martone ME, Jones YZ, and Ellisman MH. **Protoplasmic astrocytes in CA1 stratum radiatum occupy separate anatomical domains**. *Journal of Neuroscience,* 22(1);183-192 (2002)
12. Camandola S. **Astrocytes, emerging stars of energy homeostasis.** *Cell Stress,* 2(10);246-252 (2018)
13. Li K, Li J, Zheng J, and Qin S. **Reactive Astrocytes in Neurodegenerative Diseases.** *Aging & Disease,* 10(3);664-675 (2019)
14. **Incucyte® Live-Cell Analysis.** https://www.essenbioscience.com/de/products/incucyte/ (Jan 6, 2021)
15. **Live-Cell Monitoring: Optimizing Workflows for Advanced Cell Models.** https://www.essenbioscience.com/en/forms/white-paper-live-cell-monitoring-advanced/ (Jan 6, 2021)
16. Guizzetti M, Kavanagh TJ, Costa LG. **Measurements of astrocyte proliferation.** *Methods of Molecular Biology,* 758;349-359 (2011)
17. Swanson RA, Ying W, and Kauppinen TM. **Astrocyte Influences on Ischemic Neuronal Death.** *Current Molecular Medicine,* 4(2);193-205 (2004)
18. Susarla BTS, Villapol S, Yi JH, *et al.* **Temporal Patterns of Cortical Proliferation of Glial Cell Populations after Traumatic Brain Injury in Mice.** *SAGE journals,* 6(3);159 (2014)
19. Peaudecerf MS, Obel LF, Waagepetersen HS, and Schousboe A. **Complex actions of ionomycin in cultured cerebellar astrocytes affecting both calcium-induced calcium release and store-operated calcium entry.** *Neurochemical Research,* 38(6);1260-1265 (2013)
20. Oksanen M, Lehtonen S, Jaronen M, *et al.* **Astrocyte alterations in neurodegenerative pathologies and their modeling in human induced pluripotent stem cell platforms.** *Cellular and Molecular Life Sciences,* 76(14);2739-2760 (2019)
21. **Incucyte® Cell-By-Cell Software Analysis.** https://www.essenbioscience.com/en/applications/cell-monitoring-workflows/cell-by-cell-analysis/ (Jan 6, 2021)
22. Bylicky MA, Mueller GP, and Day RM. **Mechanisms of Endogenous Neuroprotective Effects of Astrocytes in Brain Injury.** *Oxidative Medicine and Cellular Longevity,* Apr 1 (2018)
23. Habib N, McCabe C, Medina S, *et al.* **Disease-associated astrocytes in Alzheimer's disease and aging.** *Nature Neuroscience,* 23;701-706 (2020)
24. Lagos-Cabré R, Burgos-Bravo F, Avalos AM, and Leyton L. **Connexins in Astrocyte Migration.** *Frontiers in Pharmacology,* 10;1546 (2019)
25. **Incucyte® Scratch Wound Migration and Invasion Assays for Live-Cell Analysis.** https://www.essenbioscience.com/en/applications/live-cell-assays/scratch-wound-cell-migration-invasion/ (Jan 6, 2021)
26. **Incucyte® Clearview 96-Well Chemotaxis Plate.** https://gbp-shop.essenbioscience.com/products/clearview-96-well-chemotaxis-plates (Jan 6, 2021)
27. **Chemotatic Migration and Invasion Assays for Live-Cell Analysis.** https://www.essenbioscience.com/en/applications/live-cell-assays/cell-migration-chemotaxis/ (Jan 6, 2021)
28. Arizono M, Inavalli VVGK, Panatier A, Pfeiffer T, *et al.* **Structural basis of astrocytic Ca2+ signals at tripartite synapses.** *Nature Communication,* Apr;11(1) (2020)
29. **Incucyte® Neurolight Orange Lentivirus.** https://gbp-shop.essenbioscience.com/products/incucyte-neurolight-orange-lentivirus-synapsin-promoter (Jan 6, 2021)
30. **Neuronal Cell Health & Morphology.** https://www.essenbioscience.com/en/communications/assays-neuroscience-research/neuronal-cell-health-morphology (Jan 6, 2021)
31. **Incucyte® Neuroburst Orange Lentivirus Reagent—Synapsin Promoter for Neuronal Activity.** https://gbp-shop.essenbioscience.com/products/incucyte-neuroburst-orange-lentivirus-synapsin-promoter-for-spontaneous-neuronal-activity (Jan 6, 2021)
32. **Incucyte® Neuronal Activity Assay.** https://www.essenbioscience.com/en/applications/live-cell-assays/neuronal-activity/ (Jan 6, 2021)

North America
Essen BioScience Inc.
300 West Morgan Road
Ann Arbor, Michigan, 48108
USA
Phone: +1 734 769 1600
Email: orders.US07@sartorius.com

Europe
Essen BioScience Ltd.
Units 2 & 3 The Quadrant
Newark Close
Royston Hertfordshire
SG8 5HL
United Kingdom
Phone: +44 1763 227400
Email: euorders.UK03@sartorius.com

Asia Pacific
Sartorius Japan K.K.
4th Floor Daiwa Shinagawa North Bldg.
1-8-11 Kita-Shinagawa
Shinagawa-ku, Tokyo
140-0001
Japan
Phone: +81 3 6478 5202
Email: orders.US07@sartorius.com

For further information,
visit www.sartorius.com

Publication No.: 8000-0761-A00 Version: 01|2021

Have a Question?
Email AskAScientist@sartorius.com